Master's thesis

NTNU
Norwegian University of Science and Technology
Faculty of Natural Sciences
Department of Materials Science and Engineering

Olav Johansen Vad

Creep deformation of an additively manufactured nickel-based superalloy

Master's thesis in Materials Science and Engineering
Supervisor: Paraskevas Kontis
Co-supervisor: Constantinos Hatzoglou
June 2022

NTNU
Norwegian University of Science and Technology

Olav Johansen Vad

Creep deformation of an additively manufactured nickel-based superalloy

Master's thesis in Materials Science and Engineering
Supervisor: Paraskevas Kontis
Co-supervisor: Constantinos Hatzoglou
June 2022

Norwegian University of Science and Technology
Faculty of Natural Sciences
Department of Materials Science and Engineering

NTNU
Norwegian University of
Science and Technology

Preface and acknowledgments

This master thesis marks my final delivery for my studies at the Norwegian University of Science and Technology (NTNU) at the study program Materials Science and Engineering. I would like to thank my supervisors Paraskevas Kontis and Constantinos Hatzoglou for their involvement in this thesis. They have helped me enter the complex world of atom probe tomography with their knowledge, simple explanations and patience. I would specially want to thank Paraskevas for his enormous passion and support which have helped me tremendously. He has provided me with knowledge that I am sure will be of great value for my future career. I also want to thank Yingda Yu for his help at the EM-lab and Kasper Hunnestad for his help and guidance for the challenging sample preparation. Thanks to Guilhem Martin from the Grenoble Alpes university for providing me samples for this thesis. Finally, I want to thank my father, Erik, for his interest and support for my studies.

The Research Council of Norway is acknowledged for the support to the Norwegian Micro- and Nano-Fabrication Facility, NorFab. The Research Council of Norway (RCN) is also acknowledged for funding the NTNU atom probe facility through the Norwegian Laboratory for Mineral and Materials Characterization (MiMaC) project number 269842.

Sammendrag

To versjoner av en nikkelbasert superlegering ble produsert med additiv tilvirkning og karakterisert etter sigetesting med SEM og atomprobetomografi. De to legeringene ble kalt CB og C da hovedforskjellen i mellom dem var at CB legeringen inneholdt bor og karbon, mens C legeringen inneholdt bare karbon. Disse legeringene ble studert for å se effekten av bor på korngrensesegregering og oppsprekking under siging. C legeringen ble undersøkt med et elektronmikroskop med sekundære elektroner, tilbakespredte elektroner og diffraksjon av tilbakespredte elektroner (EBSD). Denne legeringen hadde få sprekker som hadde propagert intergranulært. Dette kommer mest sannsynlig av at det manglet styrking av korngrensene. Det ble også funnet en del oksider inne i sprekkene som indikerer at sprekkene ble forsprøet under siging. Volumfraksjonen av γ' ble beregnet for begge legeringene og det ble funnet at volumfraksjonen var omtrent de samme for legeringene. Dette tilsier at den store forskjellen i sigemotstand kommer av tilførselen av bor i den ene legeringen og ikke volumfraksjonen av γ'. Atomprobeprøver fra CB og C legeringen ble preparert med en fokusert ionestråleetser med mål om å inkludere en korngrense i prøvene. Bare en av prøvene fra CB legeringen virket å inneholde en mulig korngrense i rekonstruksjonen. Denne korngrensen var omringet av en opphoping av dislokasjoner hvor både korngrense og dislokasjoner virker å ha segregering av bor. Det var også et karbid tilstede i rekonstruksjonen. Denne korngrensen var delt opp i to deler, en del som gikk langs karbidoverflaten og en del over karbidet. Konsentrasjonen av bor var lav på delen av korngrensen over karbidet. Dette var diskutert å kunne være på grunn av dislokasjonene da disse muligens kunne ha redusert den totale korngrensesegregeringen. Det kan også ha vært et resultat av bor som ble konsumert under formeringen av karbidet. Den siste muligheten er at denne delen består av dislokasjoner og ikke er en del av korngrensen. Det ble også funnet områder med høye konsenrasjoner av bor i flere rekonstruksjoner som var antatt å være bor som var segregert på dislokasjoner. Konsentrasjonen av bor var lav på korngrensen, noe som var diskutert å kunne være på grunn av dislokasjonene eller partikkelen i nærheten av korngrensen. Det er også diskutert at desegregering av korngrenser kan ha hendt under siging som kan ha gjort at korngrensene har mistet segregeringen av bor og derfor ikke er synlige i rekonstruksjonene. Dette kan også forklare hvorfor CB legeringen sprakk opp intergranulært da mindre segregering av bor gjorde at korngrensene ble svakere. Det er derfor anbefalt å bruke korrelativ TEM/APT i fremtidige studier for å skille korngrenser og andre fenomener med mindre usikkerheter.

Abstract

Two versions of a nickel-based superalloy produced by additive manufacturing were characterized after creep testing with SEM and atom probe tomography. The two alloys were named CB and C as the main difference was that the CB alloy had significant amounts of carbon and boron while the C alloy only had carbon. These alloys were studied to see the effects of boron on the grain boundary segregation and cracking during creep. The C alloy was investigated in the SEM with secondary electrons, backscattered electrons and EBSD. It contained a few cracks which had propagated intergranularly most likely as a result of the lack of grain boundary strengthening. It was also found a significant amount of oxides inside the cracks indicating that the grain boundaries had been embrittled during creep. The volume fraction of γ' was calculated for both alloys resulting in around the same value, thus indicating that the wast differences in creep resistance are a result of boron and not the volume fraction of γ'. Atom probe samples from C and CB were prepared with a focused ion beam with the goal of including grain boundaries in the samples. Only one of the samples from the CB alloy seemed to contain a grain boundary in the reconstruction. This grain boundary was surrounded by dislocations in a dislocation pile-up, where both dislocations and grain boundary seem to be segregated with boron. There was also a carbide present in the reconstruction. There were two parts of the grain boundary. One part that went along the carbide surface and one above the surface. The boron concentration of the grain boundary part above the carbide surface was low. This was discussed to possibly be a result of for example the surrounding dislocations as the overall segregation on grain boundaries were lowered. It could also be a result of the carbide consuming boron during formation or coarsening. The last possibility is that this part is made up of dislocations from the pile-up and is not part of the grain boundary. It was also found boron enrichments in multiple reconstructions which were assumed to be boron segregated at dislocations. It is discussed that desegregation of grain boundaries might have occurred during creep which could have resulted in grain boundaries losing the boron segregation and therefore not be visible in the reconstructions. This could also explain why the CB alloy cracked intergranulary as less boron segregation caused weakening of the grain boundaries. The desegregated boron could then for example segregated at dislocations. It is therefore recommended to use correlative TEM/APT in further studies to distinguish grain boundaries and other phenomenons with less uncertainties.

Abbreviations

AM	Additive manufacturing
SLM	Selective laser melting
HAZ	Heat Affected Zone
APT	Atom probe tomography
DDC	Ductility-dip cracking
SAGBO	Stress-assisted grain boundary oxidation
FCC	Face-centered cubic
HCP	Hexagonal-centered cubic
HV	High voltage
FIB	Focused-ion beam
BD	Building direction
SEM	Scanning electron microscope
TEM	Transmission electron microscope
WD	Working distance
SE	Secondary electrons
BSE	Backscattered electrons
EBSD	Electron backscatter diffraction
IPF	Inverse pole figure
ROI	Region of interest

Contents

1. Introduction

Additive manufacturing (AM) is a production method that has recently grown in popularity as it is able to produce geometrically complex parts in a short time. These parts would otherwise have been a lot more challenging to manufacture with traditional methods and would also produce more waste material. Some geometries might even be impossible to produce with other methods [1, 2]. Additive manufacturing includes a hand full of different methods depending on the material and the desired properties of the manufactured part [2]. Additive manufacturing of nickel-based superalloys has been of interest in multiple industries including the aerospace, automotive, power production and medical industries. There are however some concerns in the industry regarding the negative properties of parts produced with additive manufacturing including defects and anisotropy. These aspects could be detrimental to components for critical applications, such as in aero-engines [2, 3, 4]. There are still a lot unknown aspects regarding additive manufacturing of superalloys as there is a complex relation between process parameters and resulting microstructure [2, 4]. Some additive manufacturing methods as for example selective laser melting (SLM) is also able to be used for repairs as well as production. This method could be used to for example repair a turbine blade which has experienced material loss during use. AM methods used for repair are of great interest as replacing parts of nickel-based superalloys is very expensive. The goal of repairing with AM is to restore the microstructure and geometry of the damaged component instead of replacing it [5, 6, 7]. It is also proposed that AM might provide the chance for remote repairs. This could be utilized in areas where repairs are demanding, as for example in the sea or in space [4].

The majority of superalloys produced by AM are polycrystalline. The grain boundaries of an alloy influence multiple properties of the alloy. By adding solutes that segregate at grain boundaries such as boron and carbon, cohesion, mobility energy, structure and more may be changed as a result of the solutes. This can be used to design alloys with desired properties for a given application [8]. Atom probe tomography (APT) is able to clearly resolve segregation around material defects and grain boundaries which can prove useful in studies of the given material for both the solute distribution and the defect itself. Atom probe tomography is able to present data in three-dimensional maps with a resolution on the atomic scale. This gives information about the chemical composition and the atomic structure which can be of a high value. APT has therefore become a recognized characterization technique with growing usage worldwide. Especially in the field of materials science and engineering where APT has provided information of the properties of materials [9].

This thesis studies the grain boundaries and microstructure of an additively manufactured superalloy with atom probe tomography after creep. This technique enables the possibility of studying the alloy with a high resolution to see how different solutes and defects interact with each other and is affected by the environment. This defines the properties of this alloy in demanding environments as for example inside a jet engine. The important factor for grain boundary strengthening is the addition of boron, which is why two alloys with and without boron are studied to compare the effects of boron and its interaction on the grain boundaries. Both alloys are studied in a SEM and with APT to see how the creep resistance of this alloys is affected by segregation of boron on grain boundaries and other crystal defects. This thesis aims to contribute with findings to learn how additive manufacturing and creep affect and change the properties of the alloys. Knowledge of this will be important for implementing additive manufacturing for production and maintenance of components made by nickel-based superalloys, which hopefully will contribute to a more environmentally friendly use of these materials.

2. Theory and Literature

2.1 Nickel-based superalloys

Nickel-based superalloys are materials designed for applications at high temperatures and high loads. Superalloys are heavily used in gas turbines as the operating temperatures can exceed 800 °C. Superalloys outclass ceramics in these applications as they have higher ductility and toughness combined with a high creep and oxidation resistance. Superalloys are classed as high-temperature materials meaning they can maintain their mechanical properties at high temperatures. Superalloys are also able to operate under extreme conditions with challenging environments because of their high oxidation and corrosion resistance. This is important in for example a turbine driven by coal where the hot gasses generated from the coal can be highly corrosive due to the sulfur content inside the coal [10].

Superalloys are alloyed with multiple alloying elements where the main elements include Fe, Co, Cr, W, Mo, Ta, Nb, Ti and Al [11]. B and C are often added in polycrystalline alloys for grain boundary strengthening [12, 13]. Each element alters the properties of the superalloys. Cr is for example added to increase the corrosion resistance of the alloy, Ta increases creep and oxidation resistance and reduce the amount of casting defects, Co has a positive effect on the stacking fault energy, W strengthens the γ matrix and Al and Ti are added to precipitate the γ' phase [14]. Elements that have a similar atomic radius compared to nickel often reside in the γ matrix. These elements include Co, Fe, Cr, Ru, Mo, Re and W. Elements such as Al, Ti, Nb and Ta rather form γ' phase as these elements have a greater radius than nickel. Smaller elements such as B, C and Zr usually reside on grain boundaries inside the γ matrix [10]. The most important alloying elements for nickel-based superalloys, the phases they reside in and the placement of each element in the periodic table is given in Figure 2.1.

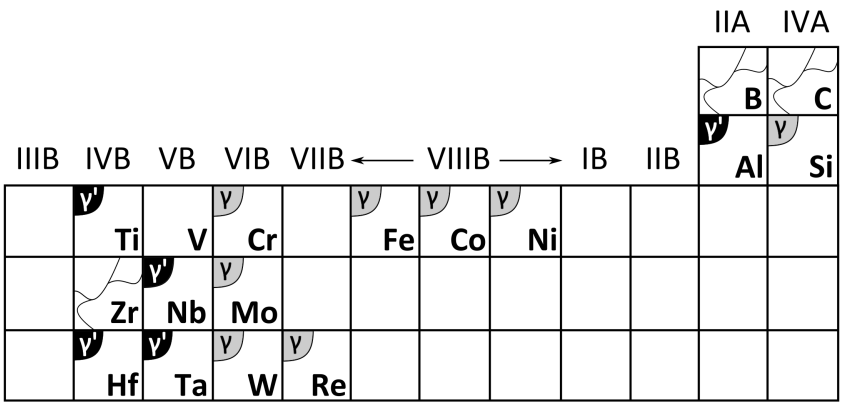

Figure 2.1: The main alloying elements in nickel-based superalloys and the phases or areas the elements reside inside the alloy [15].

Nickel-based superalloys derive their great mechanical properties at high temperatures by the phase called γ', which consists of Ni_3Al. The atomic structure of γ' and γ is given in Figure 2.2. The strengthening effect of these precipitates depends on the size and shape of the γ' phase [16, 17, 18]. An example of a typical polycrystalline microstructure for a γ'-strengthened superalloy is presented in Figure 2.3 imaged with secondary electrons. a) and b) shows the microstructure of two different samples with some variation in composition.

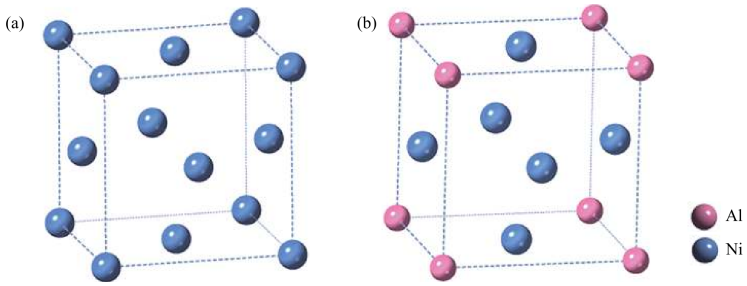

Figure 2.2: Illustration of the atomic structure of a) γ and b) γ' [19].

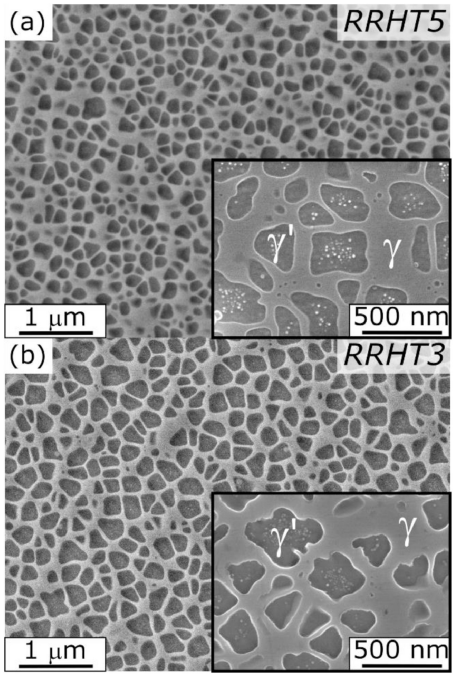

Figure 2.3: Microstructure of a nickel-based superalloy with γ and γ' phases imaged with a SEM [20].

The creep resistance of a γ'-strengthened nickel-based superalloy is said to increase with increasing volume fraction of fine γ' precipitates [21]. Increasing the amount of γ'-formers as Al and Ti therefore increases the γ' volume fraction in the superalloy [22]. The γ' coarsens during service at high temperatures, where the γ/γ' microstructure eventually ends up with the γ' phase as the matrix resulting in drastically lower mechanical properties [16, 17, 18].

Blades in gas turbines were originally polycrystalline nickel-based superalloys with an equiaxed grain structure. These alloys had a low creep resistance as the grain boundaries experienced cracking at high temperatures. These alloys were therefore replaced by directionally solidified alloys that had columnar grains. This meant that all the grain boundaries in the alloy could be aligned parallel with the stress direction to reduce grain boundary cracking. An even better solution was later to use single-crystal superalloys to remove all grain boundaries and thereby eliminate the possibility of grain boundary cracking. When the alloys no longer had any grain boundaries they were no longer alloyed with grain boundary strengtheners as B, C, Hf and Zr or alloyed with much lower amounts than the polycrystalline alloys, as these had little effect. In Figure 2.4 equiaxed, columnar and single-crystal turbine blades are showcased in the as-cast state [22].

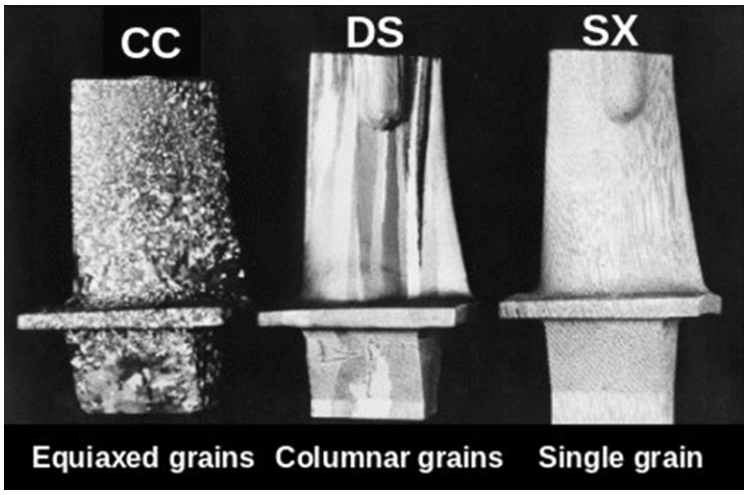

Figure 2.4: Equiaxed, columnar and single crystal as-cast high-pressure turbine blades showing visible grain boundaries inside the blades [22].

Some disadvantages with single crystal superalloys are that they are expensive compared to directionally solidified superalloys [23]. Blades with equiaxed or columnar grains are used in gas turbines in areas with low or intermediate pressures. These areas also often have moderate to low temperatures. Single crystal blades are used in areas with high pressures and temperatures up to 1150 °C [22].

2.1.1 Additive manufacturing of nickel-based superalloys

Additive manufacturing (AM) of nickel-based superalloys gives the opportunity for producing components of high complexity in small batch sizes. AM therefore has the possibility to neglecting challenges from traditional production methods with producing complex components as well as the high production costs [24]. AM of superalloys have shown promising results, where the alloy produced with AM in some cases shows properties equal or even enhanced compared to traditional production methods [25, 26]. It does however seem difficult to produce some nickel-based superalloys with AM without production defects. Especially on alloys with high amounts of Al and Ti which are classified as non-weldable alloys [27, 28, 29]. These defects include microstructural anisotropy, porosity, residual stresses and cracking [29].

Cracking is one of the main problems of additive manufacturing of γ'-strengthened nickel-based superalloys. These cracks occur during the additive manufacturing and the post processing [29, 30]. An example of a crack occurring during deposition is presented in Figure 2.5. Cracks during AM can occur as solidification cracks, postweld heat treatment cracks/strain-age cracks, ductility-dip cracks and liquation cracks [29]. These cracks are a result of the thermal cycles induced on the material during manufacturing. Ductility-dip cracking (DDC) can occur when carbides are formed at the grain boundaries of the alloy which reduces the ductility of the material. This type of cracking occurs at intermediate temperatures defined as temperatures between 40 and 70% of the melting temperature of the material.

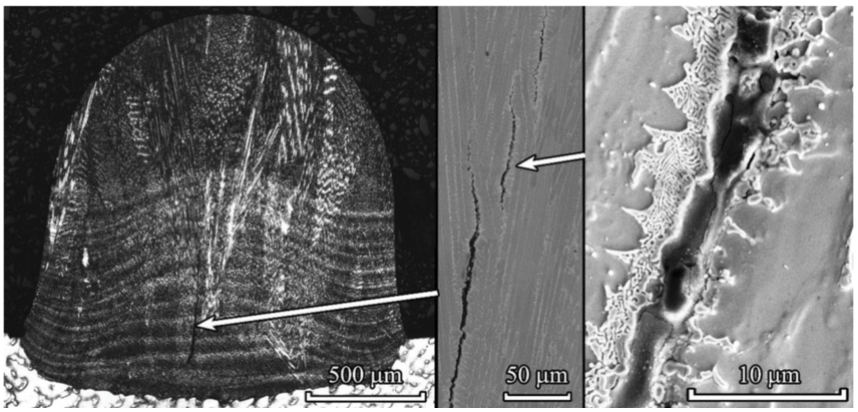

Figure 2.5: Crack formed during additive manufacturing [31].

Liquation cracking is a result of phases around grain boundaries that melts at lower temperatures than the bulk material. Liquation cracking then occurs as the liquid of these phases penetrates the grain boundary and weakens it [29]. In nickel-based superalloys these phases could for example be some types of carbides. These cracks occur at high angle grain boundaries and with laser methods this type of cracking occurs during reheating of the material from the laser during manufacturing [30]. It is however stated that liquation cracking does not occur in components produced with selective laser melting (SLM). This is because this method supposedly does not produce phases with low melting temperatures along grain boundaries which could have resulted in liquation cracking [26, 30, 32]. Solidification cracks also appear at high angled grain boundaries. These cracks do however appear at the last stage of solidification [30]. A high γ'-fraction in the superalloy also increases the chance for strain-age cracking during post-weld treatment [29]. This cracking is a result of a reduced local ductility which gives cracking at grain boundaries during the post-weld treatment [30]. Solidification cracks are a result of liquid regions being trapped between solid regions during rapid cooling of the material when it solidifies. These mixed regions of liquid and solid material then result in cracking in combination with stress. Larger components are often more susceptible to solidification cracking as larger volumes result in greater thermal gradients [29]. Different parameters during additive manufacturing often has a significant effect on the defects in the final product. An example is given in Figure 2.6 where liquation cracking in the heat-affected zone (HAZ) was studied on Inconel 718 produced with laser additive manufacturing. It was found that the total crack length during manufacturing increased with either increased heat input or scanning rate [33].

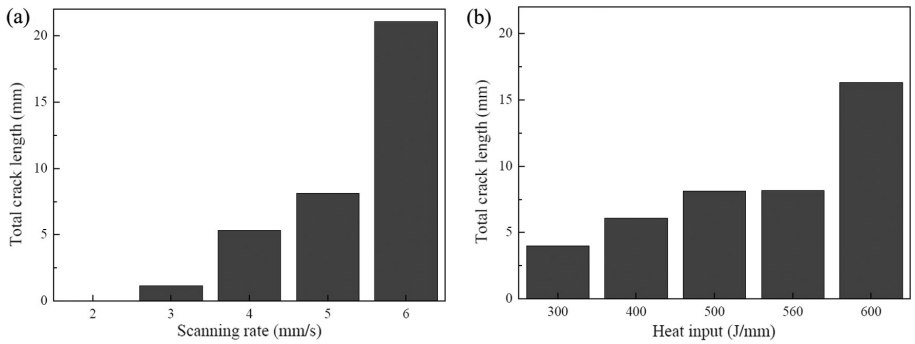

Figure 2.6: The effect of a) scanning rate and b) heat input on total crack length of liquation cracks of laser additive manufactured nickel-based superalloy [33].

Porosity can also occur in additively manufactured superalloys and seems to be a result of the production process with little variation between different alloy compositions. The porosity of the powder feedstock used during AM can however affect the porosity of the manufactured component. Imperfect melting of the powder may result in internal porosity. This could come from for example an uneven spread of the powder or because the energy applied was too low. A high energy density during AM will therefore decrease the porosity in the material. A very high energy density might however result in keyholed-induced porosity. This kind of porosity occurs when the high energy causes evaporation of the material which then is trapped inside the material. The formation of a keyhole pore is shown in Figure 2.7 in a titanium alloy. Nickel-based superalloys contain numerous alloying elements which can increase the melting range of the material. That is why keyhole porosity is usual in nickel-based superalloys. If the inert gas shielding is lacking during AM this might cause the superalloy to oxidize during manufacturing. This oxidation can then increase the surface tension resulting in ”balling” [29].

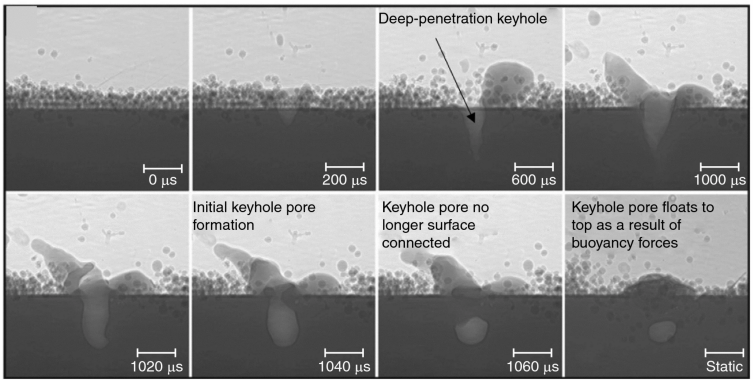

Figure 2.7: Formation of a keyhole pore in a titanium alloy shown with dynamic x-rays images. This formation happens during manufacturing with laser powder-bed fusion [34].

The concept of additive manufacturing is to build components layer by layer upon a substrate. This often results in anisotropy in the microstructure of the alloy as the method gives a columnar grain structure. With powder bed and directed energy deposition methods the microstructure gives epitaxial growth as a result of rapid solidification combined with heat loss in the specific direction of the substrate. The challenges this anisotropy gives depends however on the area of usage for the component produced with additive manufacturing [29].

There is often a need for post-processing and heat treatment of components of nickel-based superalloys produced with additive manufacturing. One reason for this is that the as-built microstructure can contain undesirable phases from the rapid solidification. Heat treatment is often also necessary for the correct high-temperature properties as the treatment controls the size and fraction of γ' precipitates. The as-built components often show lacking properties in mechanical properties compared to components manufactured with traditional routes. Post-processing and heat treatments has however shown to strengthen the additively manufactured superalloys to be able to reach equal or even increased mechanical properties compared to traditional methods. Heat treatment is however not able to affect the anisotropic mechanical properties from the additive manufacturing. These required processing steps do however add additional costs to the production of components with AM [29]. Defects as residual stress, pores and cracks may be removed or mitigated by the help of heat treatment. Heat treatments used with traditional manufacturing methods may not always be applicable for components produced with AM. Heat treatments that are specified for AM is therefore required and may need more research [2].

Repairs with additive manufacturing

Repairing with additive manufacturing of damaged components has been of great interest in multiple industries. If the repair is able to restore the microstructure and geometry of the original component it could save a lot of expenses [5, 6, 7]. One alloy which is often used to repair damaged gas turbine blades and vanes of nickel-based superalloys are the 625 alloy. This is a solid-solution strengthened nickel-based superalloy and is frequently used as this alloy has a high weldability combined with good mechanical and chemical properties [35, 36, 37, 38]. One of the methods used for repairs is laser wire deposition which is said to be able to repair complex parts with little distortion and dilution [39]. This method is growing popular for repairing components for gas turbines [38]. There are however complications with using AM for repairs as the base material of γ'-hardened superalloys might experience cracking. This could for example be solidification cracking [40, 41] and strain-age cracks [38, 41] which is explained earlier in this section. Boron has shown to have positive effect on repairs with 625 and being able to prevent solidification cracking. It is also said that boron can increase the amount of heterogeneous nucleation sites during the AM process which can result in equiaxed grain growth instead of columnar growth. It is found that this is the case for some areas, while the overall grain growth is mostly columnar [38]. Figure 2.8 shows how a die core is repaired with a hybrid AM solution combing AM and machining to get the desired properties. These solutions have shown to give desirable properties to the repaired components [31].

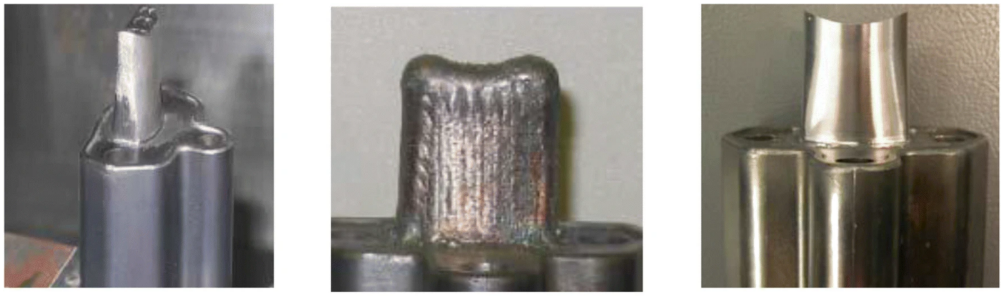

(a) (b) (c)

Figure 2.8: Hybrid repair technique of a damaged die (a) by combining additive manufacturing (b) and machining (c) [31].

2.2 Grain boundary strengthening of nickel-based superalloys

Solid-solution strengthening of alloys is when solvent atoms are added to a lattice which strengthens the material. If these solute atoms are much smaller than the metal atoms in the lattice they can occupy interstitial positions. Some of the more common interstitial alloying elements are carbon, boron, nitrogen and hydrogen [42].

2.2.1 Carbon

Carbon is added in nickel-based superalloys to improve grain-boundary strengthening of the alloy. This strengthening effect is said to be a result of mainly carbides precipitating at grain boundaries. These carbides give a higher resistance to grain boundary sliding which strengthens the alloy [13, 43]. The strengthening effect from carbides may depend on the distribution and the size of the particles. Fine and uniformly distributed carbides might give increased creep resistance while coarser carbides can act as crack initiation sites [44, 45, 46]. It is also found that some carbides may give an increased creep resistance by greatly reducing common crack initiation sites as for example casting pores [13].

Carbon can also reside at grain boundaries in solid solution in polycrystalline superalloys [47]. It is agreed that carbon and other minor alloying elements that segregate at the grain boundaries increases the creep resistance of the alloy [12, 48] It is observed that carbon segregates at grain boundaries even at small concentrations as 0.006 wt% [47]. Another effect is that carbon gives higher strength to the superalloy at high temperatures and increase the hardenability of the alloy. Alloying with carbon might however also reduce the corrosion resistance. Since carbon is a grain boundary strengthener it is usually a lower amount or not present at all in single-crystal alloys [11]. There are however cases of carbon being used in single-crystal superalloys to reduce the amount of solidification defects and oxide scales after casting [49, 50].

2.2.2 Boron

Boron is a minor alloying element in nickel-based superalloys which supposedly increases the strength of the grain boundaries. Boron is also able to form secondary phases inside the γ matrix [13]. It is suggested that boron may increase creep strength by decreasing the chance for damage initiation at grain boundaries as for example micro-cracks and cavities [51, 52]. Boron tends to reside on grain boundaries in nickel-based superalloys either in solid solution or as borides [53, 54, 55, 56]. In a study from [55] it was found enrichment of boron at carbide interfaces while it was not found any enrichment at γ/γ' interfaces. It was stated that this was similar to findings in other atom probe experiments on nickel-based superalloys alloyed with boron [56, 57]. In the article from Sijbrandij it was theorized that segregation of boron at γ/γ' interfaces could increase creep strength as the boron would increase the resistance of γ' growth. This was however not the case here as they did not find any boron at the precipitate interfaces [57]. There are however other atom probe studies that show segregation of boron at γ/γ' interfaces as [12, 58]. Boron in solid solution occupies interstitial positions and is one of the smaller elements that provide the highest strengthening effect [59]. One of the most supported theories for this is that boron increases cohesion between grain boundaries [60]. In alloys with higher amounts of boron the alloy may crack transgranulary instead of intergranulary at high temperatures as a result of boron increasing cohesion and stabilization of the grain boundaries.

A material might experience stress and strain concentrations around grain boundaries either as a result of the misorientation between the grains or because the material has few slip systems. This may then lead to either intergranular or transgranular cracking depending on the grain boundary cohesion compared with the bulk material. The strengthening effect from boron may then result in an alloy cracking transgranulary instead of intergranulary [52, 61].

The increased cohesion of grain boundaries might be the result of multiple mechanisms. One of these mechanisms include boron interacting with the dislocations to lower the movement of dislocations [52]. It is however also discussed that boron might increase the dislocation motion in grain boundaries which then decreases the chance for crack nucleation as the stresses from dislocation pile-ups decreases [62]. Some elements may weaken bonding between metal atoms by drawing charge from them. This embrittles the material. Boron however forms covalent bonds at grain boundaries which then strengthens the grain boundaries [63, 64, 65]. Another mechanism is that boron fills vacancies around grain boundaries [62, 66, 67]. Other mechanisms include boron decreasing the grain boundary diffusivity resulting in a lower void formation rate [60, 68], the fact that boron is soluble in (Ni_3Al) [69, 70, 71] and that boron prevents elements as S and H from diffusing to grain boundaries and weakening them [72, 73]. All these mechanisms depend on boron being present at grain boundaries to strengthen the alloy. Boron is attracted to grain boundaries as it has low solubility in the bulk material. The lower bulk solubility an alloying element has, the higher the grain boundary segregation is [8, 67]. It is also speculated that boron has an effect on carbides along the grain boundary which can result in initiation of cracks. The theory is that boron decreases the clustering of $M_{23}C_6$ at the grain boundaries and therefore prevent crack initiation [55, 74]. Studies with APT have shown that boron tends to segregate along grain boundaries. In these experiments carbon has also been present. Carbon have however shown to segregate in smaller concentrations than boron. It is speculated that these elements compete where boron has a higher driving force [75]. Boron has a higher mobility than carbon inside the γ matrix. This may result in carbides having a high amount of boron [55]. While boron improves creep strength of a superalloy it may also decrease the weldability of the alloy. However if carbon is present in the same alloy the weldability may be higher combined with increased mechanical properties. With APT it was observed that carbon reduced the segregation of boron around grain boundaries drastically which may be why the weldability of the alloy increased. It was proposed that this was a result of carbon changing the diffusion behavior of boron inside the bulk material. The presence of carbon may also decrease clustering of boron and other interstitial elements inside the bulk of the alloy. This was proposed after studying areas with APT which were not grain boundaries [47]. During some studies of nickel-based superalloys produced with additive manufacturing it is found boron segregated to grain boundaries in the as-built state before heat treatment [12, 76].

2.3 Grain-boundary cracking in nickel-based superalloys

The strength of the grain boundaries is one of the most important factors in a polycrystalline superalloy [14]. Grain boundaries are especially important during high-temperature deformation as intergranular cavitation, void nucleation and grain boundary sliding can occur at the grain boundaries during creep, resulting in fracture [77].

2.3.1 Grain-boundary embrittlement

Nickel-based superalloys have seen a lot of use in the aircraft and power industry because of the alloys mechanical strength, corrosion and oxidation resistance [10]. The oxidation resistance at high temperatures comes from the formation of oxide layers on the surface of the alloy. This oxide layer can consist of aluminium, chromium and silicon oxides which prevents further oxidation of the alloy [78]. The environmental effect on alloys increases with increasing temperatures which may result in the alloy failing. An example of this is shown in Figure 2.9 with fracture surfaces of samples tested at increasing temperature. It is evident that the amount of oxides at the surface increase with increasing temperature. These areas cracked intergranulary [79]. Crack nucleation and especially propagation can be affected by the environment. This may result in decreased life of components. By changing the microstructure of an alloy one can affect the environmental affect on crack growth drastically [80].

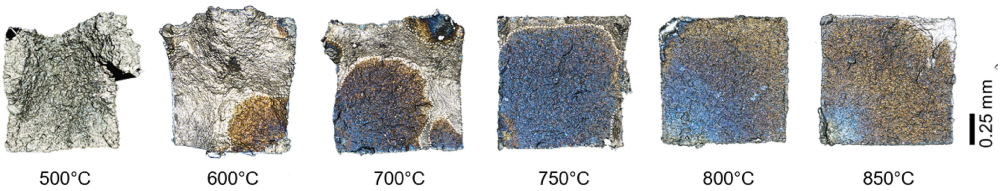

Figure 2.9: Optical microscopy images presenting fracture surfaces tested at different temperatures. An increasing amount of oxides is detected at the samples tested at higher temperatures [79].

The grain boundaries of polycrystalline superalloys are also affected by the environment and can reduce the strength of the material when reacting with oxygen at elevated temperatures. Cracking as a result of the material reacting with the environment is one of the largest challenges for superalloys used in jet engines and power production. Higher operating temperatures are required for an increased fuel efficiency. This also increases the chance for environmentally induced damage [79]. Turbine discs in modern jet engines are exposed to high temperatures combined with stress and an oxidizing environment which could result in time-dependent intergranular cracking [81]. There are multiple explanations for what causes environmentally-assisted cracking in polycrystalline superalloys. Some argue that the reason might be oxygen or other oxidizing elements that diffuse ahead of the crack tip resulting in dynamic embrittlement [82, 83, 84]. The oxygen is said to decrease the cohesion between grains resulting in intergranular cracking when subjected to stress [85]. Others believe the cracking is a result of stress-assisted grain boundary oxidation (SAGBO) [81, 85, 86].

A study from Nemeth et al. [79] states that the crack tip of an intergranular crack was studied with various methods. These were methods of high spatial resolution including transmission electron microscopy and atom probe tomography. It is stated that these methods gave results indicating a formation of layered oxides along the grain boundaries of the γ-phase in front of the crack tip. They therefore state that this seems similar to the SAGBO mechanisms [79]. The SAGBO mechanism is described as the grain boundary ahead of a crack being oxidized before fracture. This means that the crack propagates through brittle oxides at the grain boundary [85]. The oxides ahead of the crack grow from increased diffusion of oxygen through the oxides as a result of the applied stress. The stress may also change the boundary conditions of diffusion at the end of the oxide or the crack tip [86]. During oxidation of the surface of a nickel-based superalloy, NiO is the first oxide to form at the surface as this is a fast-growing oxide. This reaction can then lower the oxygen partial pressure close to the surface which promotes the formation of oxides from alloying elements as for example Cr, Ti and Al. These elements form their own layer of oxide at the surface. It is discussed that the same layered structure occurs ahead of the crack tip during environmentally-assisted cracking. This is however not confirmed to be the case as these oxides also could form after cracking [81]. Figure 2.10 shows an APT reconstruction of oxides present ahead of a crack tip.

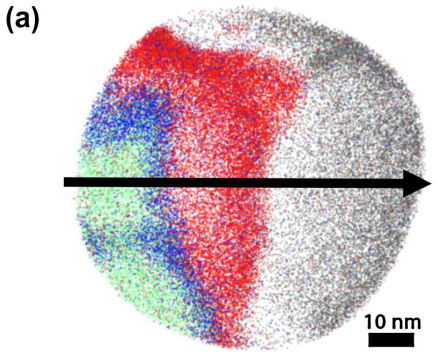

Figure 2.10: APT reconstruction of oxides found close to a crack tip. Each colour represents different oxides. The green layer is closest to the crack and represents a nickel-rich oxide, the blue is a nickel and iron-rich oxide, the red is a chromium-rich oxide and the grey is chromium inside the alloy [85].

Dynamic embrittlement was a term first used by Liu and White to describe the cracking they observed in their experiment [40]. The strength of the material and the type of elements causing embrittlement affects the susceptibility to dynamic embrittlement, where an increased strength increases the sensitivity. Grain boundaries with low diffusivity are more resistant to dynamic embrittlement which means that the effects of dynamic embrittlement may be lowered by processing or alloying. Alloying with elements that segregate at the grain boundaries decreases diffusion by decreasing the amount of free volume around the grain boundaries. Stress is the driving force for diffusion of atoms absorbed at the surface of the material during dynamic embrittlement. These atoms are then often diffused along grain boundaries. This is different from the role stress has in SAGBO where it is connected with the volume expansion by formation of oxides [82]. An example of an intergranular fracture from dynamic embrittlement is shown in Figure 2.11. Dynamic embrittlement of nickel-based superalloys occurs at temperatures above 500°C [87]. Dynamic embrittlemnt starts with oxygen diffusing along the grain boundaries ahead of the crack tip. This diffusion is driven by the high temperature and stresses. Then grain boundary decohesion occurs as a result of oxygen embrittling the grain boundary. These embrittled grain boundaries are then cracked by stress [84]. Often when the same tests are performed in vacuum and a given environment the samples fracture transgranulary in vacuum and intergranular in the given environment [87]. It is proposed that alloying with carbon and boron in nickel-based superalloys might result in a lower oxidation resistance. This does however require more studies [88].

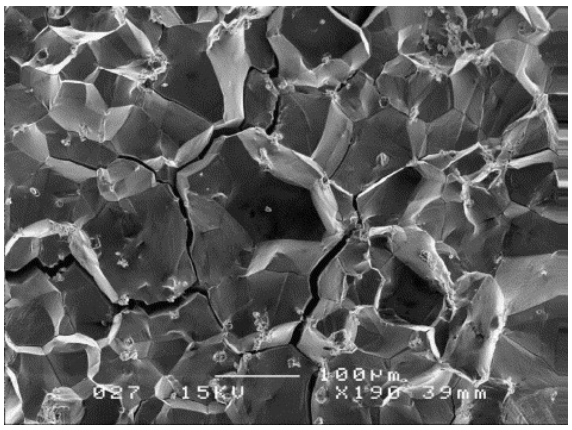

Figure 2.11: Intergranular fracture in a superalloys as a result of dynamic embrittlement [82].

2.3.2 Segregation of solute atoms at crystal defects in nickel-based superalloys

When nickel-based superalloys experience plastic deformation during elevated temperatures solutes might be redistributed inside the crystal lattice during deformation. The segregations then tend to segregate around crystal defects inside the lattice. The segregation depends on the type of crystal defect and also the composition of the alloy and the magnitude of the temperature and stresses. These crystal defects could for example be different kinds of stacking faults or dislocations. The interactions between the defects and solute atoms result in a change in the microstructure of the alloy and may also give altered properties [89] as for example increased creep properties [20]. It is observed segregation of multiple elements in nickel-based superalloys including Co, Cr, W, Mo, Nb, Ti and Ta. The elements that segregated around the defects varied between different alloys and different types of defects [89, 90, 91]. Interactions between crystal defects and solute atoms has also been found in Co-based superalloys and titanium alloys [89]. There are observed multiple atoms that can segregate to dislocations inside nickel-based superalloys. One example is from [92] where they observed segregation of Co,Cr, Mo and Re around dislocations inside the γ' phase. This was for a single crystal superalloy after creep deformation. These elements are known as γ stabilizers [92]. It is stated that interstitial atoms as boron, carbon and nitrogen can diffuse into dislocation cores in BCC or FCC alloys as steels, aluminium alloys and nickel-based superalloys. The interstitial atoms then slow down dislocation movement [93, 94, 95, 96]. In an article from [97] it was discussed that carbon can form Cottrell atmospheres around moving dislocations in nickel alloys. The carbon would however diffuse to γ' precipitates. This diffusion then decreased the strengthening from the atmosphere as it had less restrictions on dislocation movement [97]. In an article from [98] they studied a solid-solution strengthened titanium alloy with APT. This alloy was strengthened with carbon. In their results they found that carbon was mostly homogeneously distributed apart from some areas with high carbon concentrations. The reasons for these concentrations were discussed to be carbon surrounding dislocations in a Cottrell atmosphere [98]. It is suggested that the driving force for solute atoms to segregate at dislocations are the stress fields created by the dislocations. These solutes then segregate along the dislocation line and create an enriched area of solute atoms called Cottrell atmospheres. At higher temperatures new atmospheres may appear during deformation which can slow down newly created dislocations. This is called dynamic strain aging [94].

2.3.3 The Suzuki effect

The Suzuki effect is when solute atoms interact with stacking faults in the crystal structure of a FCC alloy. These solute atoms segregate around the stacking fault [99, 100]. Stacking faults occurs in most metals that have experienced plastic deformation. Slip in a specific plane in a FCC structure will result in deformation stacking fault where a section will have a HCP structure instead of FCC. This HCP region will then have a higher free energy than the FCC structure. The stacking fault has two partial dislocations at each end. These partial dislocations repel each other while the surface tension pulls them against each other. If a stacking fault has a low stacking fault energy it will result in a wide stacking fault with a large separation between the partial dislocations. A high stacking fault gives a narrow fault with a low distance between the dislocations. The interstitial atoms also need to be soluble in the HCP structure of the stacking fault for the Suzuki effect to happen. The energy of the stacking fault decreases with increased concentrations of solutes which again increases the separation of the partial dislocations of the stacking fault. This strengthens the alloy as this reduces the mobility of the dislocation and as it requires more work to draw in the partial dislocations [42]. Suzuki segregation affects the deformation mechanisms of an alloy as twinning and cross-slip of dislocations are affected by the segregations. When compared with segregations at grain boundaries and Cottrell atmospheres around dislocations, the suzuki segregation should theoretically be weaker. This is a result of the atomic structure around the stacking faults being almost the same as in the bulk material [101]. Metals with a low stacking-fault energy are often used for high-temperature applications. This is because the low stacking-fault energy results in increased resistance for cross-slipping of the partial dislocations which increases the creep resistance of the alloy. The stacking fault energy decreases with increasing solute valence. Solid-solution can increase the strength of the alloy by multiple mechanisms including the Suzuki effect, interactions with vacancies and jogs, elastic interactions with dislocations and segregation at grain boundaries by influencing grain-boundary sliding and migration [42].

2.4 Quantification of grain boundary segregation of light elements

Characterization techniques such as electron beam microscopy are not able to perform precise composition measurements of light elements such as B, C and N. One reason for this is that the contrast is very dependent on the atomic number, which means light elements are challenging to image as these have little electron scatter compared to other elements. This is however not the case for atom probe tomography (APT) as the 3D data on the atomic level is well suited to for example study interactions between solutes. APT is generally better for studying light elements and small features [102]. This is the reasoning for using APT in this thesis as boron and carbon are the main interests. Only APT is able to quantify the amount of these solutes in the microstructure in 3D.

In atom probe tomography (APT) atom by atom is removed from the specimen needle tip by field evaporation, which then is detected by a detector and used to reconstruct the analyzed volume in 3D. Field evaporation is a combination between desorption and ionization, which evaporates atom by atom and atomic layer by atomic layer. This ionization is a result of an electric field and applied pulses from either a laser or high voltage at the surface atoms. The atoms are removed by the lattice with an intense electric field during field evaporation that polarises the surface atoms and decreases the energy barrier for an atom to escape the surface. With a strong enough field the atoms can be removed from the surface while leaving an electron in the surface of the material. The required field is often around 10-50 V/nm depending on the element. Nickel for example requires around 35 V/nm for evaporation [9]. Field evaporation only occurs at the surface of the specimen as a result of the electric field only penetrating small depths, even smaller than an atom for metallic materials. The evaporated atoms are then accelerated by an electric field into a detector. The strength of the electric field needs to be increased through the experiment to field evaporate the atoms because the radius of the specimens increases throughout the atom probe experiment [9]. The electric field at the specimen surface is related to the radius of curvature at the specimen needle tip given by Equation 2.1.

$$F = V/k_f R \tag{2.1}$$

Here F is the electric field, R is the radius of curvature, V is the voltage and k_f is the field factor. This factor is to account for the specimen being shaped like a needle and often has a value between three and eight. The specimen is shaped like a needle to achieve a high electric field at the specimen surface, high enough to evaporate atoms with field evaporation [9].

2.4.1 Experimental structure of the atom probe

The specimen in an atom probe experiment is mounted on a stage that can move in all three dimensions. The specimen is placed in front of a counter electrode where the specimen is connected to a High-voltage (HV) power supply to generate the electric field. The specimen is cooled inside the ultra-high vacuum chamber to around 20-100 K, depending on the material. The pressure inside the vacuum chamber is below the base pressure of 10^{-8} Pa. A high-voltage pulser is connected to the counter electrode which sends out high-voltage pulses onto the sample lasting only a few nanoseconds. This method of evaporation is only possible for electrically conductive materials. If a laser is instead used a pulsating laser is focused on the specimen tip. When using a laser source in the atom probe, field evaporation occurs by thermal activation where light from the laser is absorbed by the specimen and increases the surface temperature. The laser-pulsing techniques still result in a high spatial resolution and make the atom probe applicable for non-metallic materials which are not conducting [9]. An illustration of the experimental setup for atom probe tomography is presented in Figure 2.12.

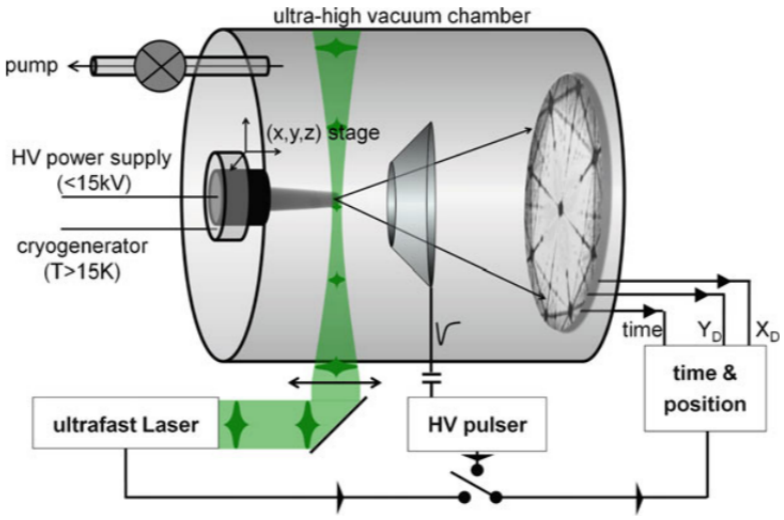

Figure 2.12: Illustration of the experimental setup of atom probe tomography. Each component of the setup is marked in the figure [9].

The introduction of position-sensitive detectors resulted in atom probe tomography with the possibility of reconstructing the analyzed volume in a three-dimensional space. This combined with the detection of the time-of-flight results in the characterization and placement in a three-dimensional space of each atom. The impact of an ion is transferred to an electrical signal that is then translated to the coordinates of the atom. The detectors do however struggle to detect multiple impacts close to each other as the detector might believe it is one single ion [9].

2.4.2 Experimental procedure for atom probe experiments

An atom probe experiment starts with specimen alignment where the position of the specimen needle tip is compared to the counter electrode. The specimen is first centered relative to the counter electrode before the specimen is moved closer to the counter electrode for a better field of view during the experiment. When the experiment has started the analysis of each ion starts with recording the time-of-flight which is later translated to the mass-to-charge ratio to determine the element of each ion. The data of every ion is then used to construct a model in three-dimensional space. There is a so called "detection window" from when a pulse is applied to a signal is detected. This is how time-of-flight is measured. When a signal is detected, it is assumed that this is an ion that is generated from the pulse at the start of the detection window. There is a chance that a pulse does not end up generating an ion or that it generates multiple ions at once. The average number of atoms that are detected per pulse is referred to as the detection rate. The voltage is often adjusted during an experiment to try to achieve a constant detection rate. Heavy and complex ions can be problematic as these could have a long time-of-flight. It is even possible that this time exceeds that of the detection window [9].

The time-of-flight of each ion is translated into the mass-to-charge state which is combined for all ions to create a mass spectrum. This mass spectrum explains the elemental composition of the specimen [9]. The natural isotopic occurrences of each ion are also included to characterize each peak in the mass spectrum [103]. The temperature of the specimen in an atom probe experiment decides the electric field required for field evaporation. This is an important parameter because one does not want atoms to evaporate in between voltage or laser pulses. This can happen if the sample contains different elements with different critical field strengths for field evaporation. This would again result in the collision of ions into the detector outside of the detection window. It is therefore required to apply a low field to avoid field evaporation between pulses. This field is generally lower during laser pulsing compared to high voltage pulsing [9].

2.4.3 Fracture of APT specimens

In some cases the APT specimen might fracture during an atom probe experiment. To achieve field evaporation a strong electrostatic field is applied which can result in fracture of the specimen. This is most likely because of the pressure from the applied field [9]. When using a laser the specimen is only exposed to a constant mechanical stress from the electric field. This is a contrast from using high voltage pulses where cyclic stresses also are applied on the specimen. The overall voltage is also reduced during laser pulsing [104]. Small fractures called micro-fractures might occur. During these events the shape of the needle tip might recover and end up in its equilibrium form and give feasible results. This is however not possible if the fracture is too severe. During these fractures the atom probe does not detect any ions and increases the voltage trying to correct this. This ends up in results that clearly show a fracture, as for example the mass spectrum contains mostly noise. Using laser-pulses instead of high-voltage pulses might be a good solution for brittle materials because of the electrostatic stress during high-voltage pulsing. Laser often results in more successive experiments compared to high voltage [9].

2.4.4 Sample preparation

The samples used in the atom probe are shaped like a needle where the area of interest should be located at the tip. The sample preparation for the atom probe is essential and demanding. Electrochemical polishing is a popular method for sample preparation for APT. This method does however have the drawback that it is impossible to prepare a needle containing a specific area at the apex of the specimen. So when specific microstructural features need to be analyzed, a focused ion beam microscope (FIB) is used for sample preparation [9].

There are multiple requirements for samples used in the atom probe. The specimen needs to be needle shaped to attain the required field strength for field evaporation and to achieve a sufficiently uniform field. The tip of the needle is required to have a radius lower than 50 nm. A too large radius will result in a requirement of a too high voltage of what the microscope can handle. The farther away the area of interest is from the needle tip the larger the recorded dataset needs to be. It is therefore recommended to have the area of interest within 100 nm of the needle tip. Another sample requirement is also that the sample is smooth and free from grooves and cracks as this could affect the reconstructed data and could act as stress concentrations which could break the sample under the applied field [9]. The requirement of a circular and smooth cross-section of the specimen is to make it easier to reconstruct the specimen accurately. The quality and robustness of the specimen used in the atom probe have a high affection on the results of the experiment [103].

FIB-based methods for preparing needle samples are often selected if the material cannot be electropolished or if the specimen needs to be prepared from a specific location. One category of FIB-methods used for sample preparation is called lift-out methods. These methods consist of cutting a small portion of the sample free from the surface with the FIB. This section is then lifted out with micromanipulators before it is shaped into a needle [9].

3. Experimental procedures

3.1 Samples

The studied alloy was the γ'-hardened AD730 which was additively manufactured and creep tested. Two versions of this alloy were studied. These were named CB and C as the main difference between these alloys were the addition of boron in the CB alloy. The C alloy contained negligible amounts of boron and only had significant levels of carbon, while the CB alloy had significant values of carbon and boron. These versions were compared to find the effects boron have on this alloy during additive manufacturing and creep. This was performed by studying the grain boundaries of the alloy. The composition of each alloy is presented in Table 3.1. The CB alloy was also studied in [105]. Both samples were produced with laser powder bed fusion with an EOS M290 machine at the university of Grenoble.

Table 3.1: Composition of the alloys named CB and C in weight percent. ”-” means that the content is below 0.001 % of the alloying element [12].

Sample	Ni	Al	Ti	Cr	Fe	Co	Nb	Mo	W	B	C
CB	bal.	2.3	3.1	16.5	4.1	8.5	0.5	3.1	3.1	0.004	0.038
C	bal.	2.2	3.6	16.2	3.6	8.1	1	3.0	3.1	-	0.010

The alloys were heat-treated at 1080 °C for 4 hours and aged at 760 °C for 16 hours after manufacturing. This heat treatment is a standard for this alloy. Creep samples were produced from each sample with a diameter of 4.5 mm and 22.5 mm in length. The creep tests were conducted with a loading direction perpendicular to the building direction with a load of 690 MPa at 650 °C. The creep resistance of each sample after heat treatment is given in Figure 3.1. The blue dots indicate the results for the C alloy and the green dot indicates the CB alloy. The alloy giving the red dots were not included in this experiment. The creep resistance is plotted using their Larson-Miller parameter. It is shown that the creep resistance of the CB alloy is at the level as that of the same alloy if it was cast and wrought. The C alloy does however have lacking creep resistance compared to the CB alloy and the cast and wrought alloy. For the creep tests the CB alloy survived for over 2000 hours while the C alloy only lasted around an hour or less. For more information about the manufacturing, heat treatment and creep test of these alloys see [12].

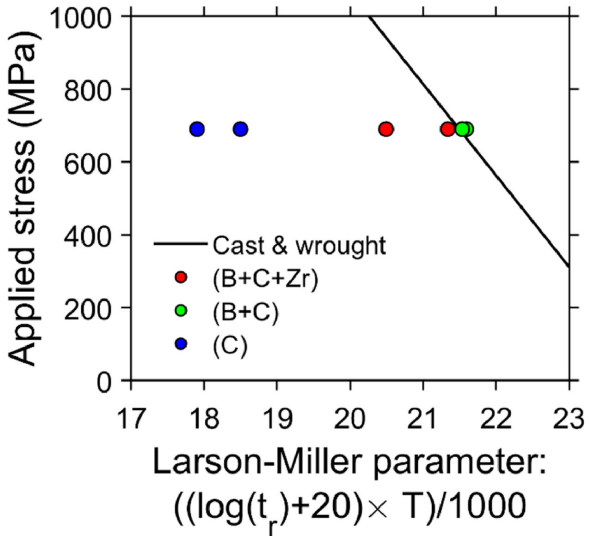

Figure 3.1: Creep resistance for the samples produced with AM compared with the same alloy cast and wrought. The creep resistance is plotted with the Larson-Miller parameter [12].

3.2 Scanning electron microscopy

Both samples were cut, grinded and polished with a colloidal finish of 1 μm with OPS-Nondry. The samples were cut perpendicular to the fracture surface as seen in Figure 3.2. The samples were then analyzed in a Zeiss Ultra 55 scanning electron microscope (SEM) with secondary electrons (SE), backscattered electrons (BSE) and electron backscatter diffraction (EBSD). These imaging techniques were used to study cracks at the polished sample surfaces to observe how the samples fractured during the creep test. The sample was mounted and tilted 70 degrees for the EBSD analysis. The program used for the analysis is called Nordif 3.2. TSL OM Data Collection 7 and TSL OM analysis were used for the data analysis. Table 3.2 shows the values of the parameters used for the EBSD analysis.

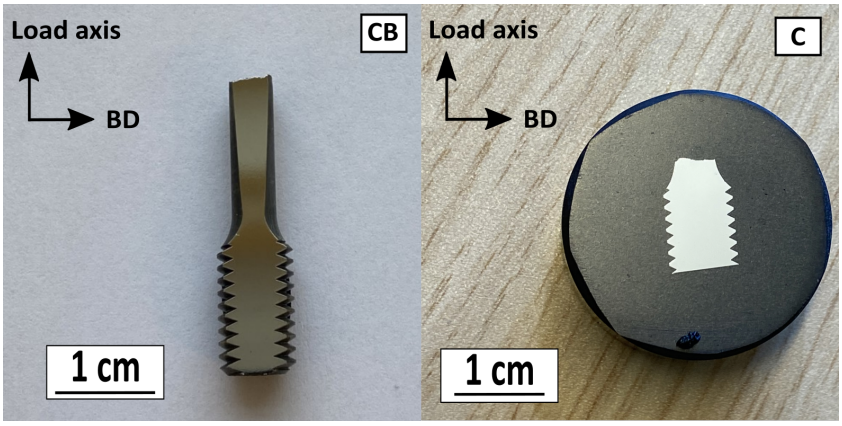

Figure 3.2: Images of the samples from the CB (left) and C (right) alloys after polishing.

Table 3.2: Parameters used at the SEM with each imaging technique.

Parameter	Value
Acceleration voltage (SE/BSE)	10 kV
Acceleration voltage (EBSD)	20 kV
Working distance (WD) (SE/BSE)	8 mm
Working distance (WD) (EBSD)	25 mm
Aperture (SE/BSE)	60 μm
Aperture (EBSD)	120 μm

3.3 APT sample preparation

Grain boundaries in the alloys were the main interest to see the effects of boron, as it was expected to find segregation of boron at the grain boundaries in the CB alloy. All cracks found with the SEM was found to go along grain boundaries which highlights the importance of the grain boundary chemistry during creep. It was therefore necessary to use a sample preparation method able to prepare APT samples containing grain boundaries. All samples used in the atom probe experiments were therefore prepared with a FEI Helios Nanolab Dual Beam FIB (focused ion beam) located at the NTNU Nanolab. Samples were prepared from grain boundaries observed at the polished sample surface. These grain boundaries were ahead of or close to a crack from the creep test. The sample preparation consisted of multiple steps that were followed, where the first step was to tilt the stage with the sample to 52° and find the Eucentric point. Different beam currents for the ion beam was used for different steps during the preparation. These are listed for each step in Table 3.3 combined with the stage tilt. Images from the sample preparation with the FIB is given in Figure 3.3 for multiple stages in the preparation.

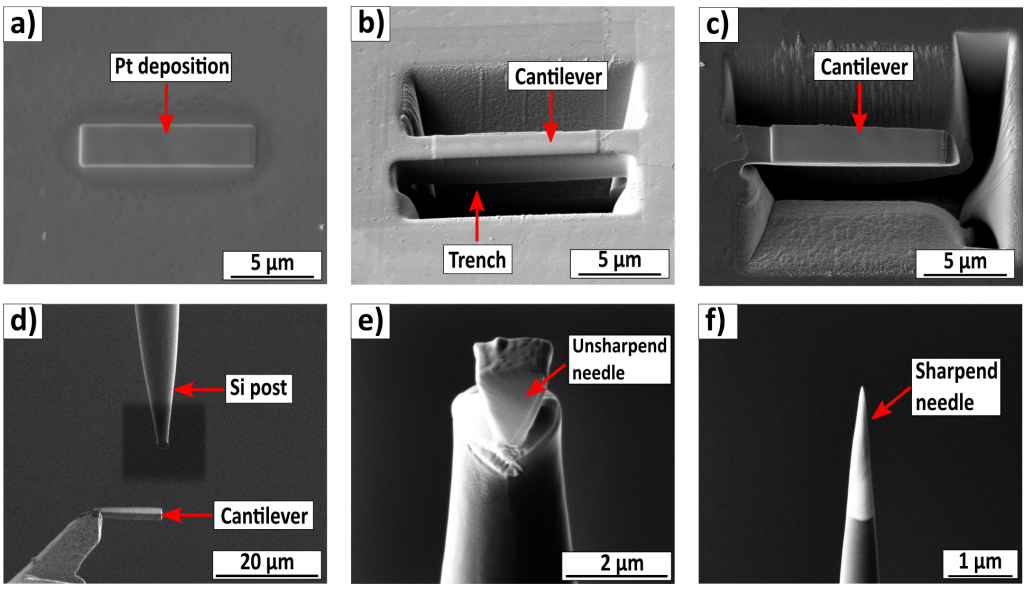

Figure 3.3: Collage of images from the sample preparation with the FIB imaged with secondary electrons or ions. a) Deposited Pt layer on top of the region of interest. b) Cantilever beam after milling of trenches and clean-cuts. c) Cantilever beam after cantilever cut, right before lift-out. d) Lift-out of cantilever and placement on micro post. e) Sample welded on top of a post before sharpening. f) Finished needle after sharpening and low-kV cleaning.

First a Pt layer was deposited at the area of interest as seen in Figure 3.3 a). This Pt layer was deposited to protect the area of interest. This protective layer was deposited as a rectangle with the rectangle pattern in the software. When grain boundaries were studied the Pt layer was deposited so the grain boundary laid in the middle of the rectangle. This rectangle varied in size depending on the grain boundary. Typical dimensions were 10μm x2.50μmx0.3μm. Then two trenches were milled at each side of the Pt layer at 30° with respect to the surface normal. Each trench was milled above the Pt layer while the stage was tilted 22°. The stage was rotated 180° before the next trench was milled. This resulted in the trenches meeting and giving a cantilever beam with a triangle cross-section. The trenches were also milled as rectangles with a width of 4-5μm wider than the Pt layer. The trenches were always milled at a depth of 3-5μm. The trenches were milled around one micrometer from the Pt layer to save space for the clean cuts. These cuts were performed on both sides of the Pt rectangle between the rectangle and the trenches. Cleaning cross-section were used for this at the edge of the protective layer with the cut ending close to the protective layer. Figure 3.3 b) shows the cantilever beam after clean-cuts and trenches.

After the cleaning-cuts the beam was cut out as seen in Figure 3.3 c). First the right side of the beam was cut from the sample with a rectangle cut. A lift-out needle was then placed at the same end as the cut and welded together with the beam. Pt was used for this weld with a rectangle pattern wide enough to cover both the cantilever and lift-out needle. Lastly, the beam was cut free at the other end of the lift-out needle. The beam was then transported to a Si coupon and welded onto microtip posts inside the vacuum chamber of the FIB. The end opposite of the lift-out needle was placed carefully at the post before it was welded to the post and cut free. This is shown in Figure 3.3 d) and e). This was done for the whole length of the beam until the whole beam length was placed at posts. Lastly, the sample stage was rotated 180° to weld at the opposite side of the microtip posts. All samples were placed at the same side of the coupon. This was because the laser-pulsing mode was used during the atom probe experiments.

The last step of the sample preparation was the milling to shape the cut beam into needles. This step consisted of multiple millings and a final low-voltage clean-up. Before the milling the sample on each needle was rotated to check for grain boundaries at the surface. The milling was performed to try to center the grain boundaries inside the needle tip. A small circle was deposited on top of the sample to mark the grain boundary from above. The first milling step was used to remove the bulk of the material and to push down the needle at least 10 μm from the apex of the specimen to prevent secondary spikes at the sample. These spikes could give inaccurate results from the atom probe experiment. The sample was milled until the whole sample had a diameter equal to the inner diameter of the milling. All millings were performed with a circular pattern with defined inner and outer diameters to shape the needles. The inner diameter was decreased for each milling. The next milling steps were used to shape the sample into a needle by shaping the tip. This was done until the tip was small enough without reducing the shank angle too much. The last milling step was then done with the smallest inner diameters to give the final tip shape of the needle. The radius of the needle tip was reduced until it was lower than ca. 100 nm. This gave the final needle shape used in the atom probe experiments. It was also done a clean-up of the sample surface performed at a low voltage. This stage cleans up damage from the Ga source of the FIB after the millings. The clean-up was done with a voltage of 5 kV. Figure 3.3 f) shows a finished needle after sharpening and low-kV cleaning.

Table 3.3: Parameters used at the FIB during each step of the sample preparation.

Preparation step	Stage tilt	Beam current	Pattern
Deposition of protective layer	52°	0.28 nA	Rectangle
Milling of trenches	22°	6.5 nA	Rectangle
Clean cut	52°	0.28 nA	Cleaning cross-section
Cantilever cut	52°	6.5 nA	Rectangle
Welding prope to cantilever	0°	28 pA	Rectangle
Cutting free the cantilever	0°	0.28 nA	Rectangle
Welding cantilever onto microtip post	0°	28 pA	Rectangle
Removal of cantilever from micropost	0°	0.28 nA	Rectangle
First milling	52°	0.46 nA	Circle
Second milling	52°	0.28 nA	Circle
Third milling	52°	0.28 nA	Circle
Fourth milling	52°	93 pA	Circle
Fifth milling	52°	93 pA	Circle
Sixth milling	52°	48 pA	Circle
Low kV clean-up	52°	47 pA	Circle

Figure 3.4 shows a sample welded on top of a post after lift-out and before sharpening. In this image a grain boundary is visible in the sample. The sharpening for each sample was then conducted to try to get this grain boundary inside the needle tip which required a radius of around 50 nm. This was challenging as it was easy to mill the grain boundary away. It was often also difficult to see the grain boundary on the sample, especially after some milling steps during the sharpening. It is also clear in the image that the grain boundary is not completely straight, making it even more difficult to place the grain boundary inside the needle tip.

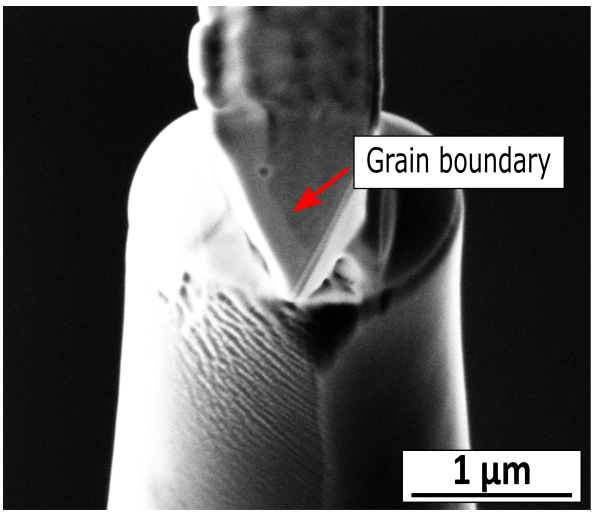

Figure 3.4: Sample after lift-out before sharpening to a needle taken with secondary electrons in the FIB. A grain boundary is present in the sample marked with a red arrow.

3.4 Atom probe tomography

The coupon with samples was placed inside the vacuum sample the day before or earlier the APT experiment was conducted. All experiments were conducted using pulsating-laser mode as the samples were brittle due to stresses after creep deformation. Using voltage mode would apply high stresses to the sample which might fracture it. All experiments started with moving the laser to the correct post on the coupon and specimen alignment. This specimen alignment was conducted to find the apex of the sample to make sure the laser was applied correctly at the sample. This calibration was done with 200 kHz pulses and 40% detection rate. The voltage was increased manually during the calibrations. These parameters were then changed before the experiment started. During the APT experiments the pulse rate was set to 125 kHz, the detection rate to 1%, the temperature to 45 K and a pulse energy at 35-50 pJ. This usually resulted in APT datasets containing at least 80 million impacts, which was providing statistically enough information. Since the presence of boron in the microstructure was one of the main objectives, mainly the CB alloy was investigated by collecting seven APT datasets, while one was collected for the C alloy. Of the eight data sets only five are included in this thesis, while the rest were showing the same result. The samples that were studied with APT were eight out of a total of around 20 samples. The samples chosen were those without defects from the sample preparation and which were believed to most likely contain a grain boundary.

3.4.1 3D reconstruction and data treatment

The IVAS 3.8.10 software from Cameca was used for data analysis and 3D reconstructions. The APT experiment resulted in a HIT file with an APT data set which was uploaded to the program. A SEM image of the sample tip was used to specify the tip radius of the specimen needle used for the experiment. The ion sequence range and detector ROI (region of interest) was also specified in the program. Then the peaks in the mass spectra were identified with the known alloying elements and possible impurities. Elements as hydrogen, hydroxides and water was not included as these are decontaminations from the sample surface and vacuum. Gallium was included and is from the sample preparation with the focused ion beam. Some elements had overlapping values which complicated the process. These peaks were classified as one of the elements if it seemed like the occurrence of that element dominated in that peak. These peaks were later decomposed for composition analyses.

When the sample was reconstructed in 3D the sample was analyzed. Using different alloying elements with different colours to highlight for example different phases, grain boundary segregations and enrichments. Chromium was frequently used to highlight the γ phase while titanium and aluminium were used to highlight the γ' phase. Boron and carbon were the elements of interest in this study and was therefore highlighted and studied in each sample. Iso-surfaces were also used often to highlight surfaces and to easier see for example the presence of boron and carbon. Concentration profiles and proxigrams was also constructed at specific areas to showcase variations in composition around for example different phases and grain boundaries. It was also conducted calculations for the volume fraction γ' with the lever rule method.

4. Results

The main part of the experiments was conducted on the CB alloy to see the effect of boron on the microstructure. This includes investigations of a grain boundary, boron enrichments and a particle found in various APT reconstructions. The C alloy was mainly used to compare results with the CB alloy. Results from the C alloy include cracks on the polished sample surface to compare with the results found for the CB alloy given in the specialization project [105], and to compare the γ/γ' microstructure and the volume fraction of γ' between the alloys.

4.1 Intergranular cracking during creep

The C alloy was investigated using secondary electrons, backscattered electrons and electron backscatter diffraction to study the crack propagation. Here, cracks were the main interest to see how these had propagated during creep. It was only found cracks close to the fracture surface, compared to the CB alloy where it was found cracks close to the fracture surface and around 1-3 mm away. The results from the CB alloy is presented in [105] and some results can also be found in Appendix A in this thesis. The CB alloy had interesting phenomenons that not were observed at the C alloy including cracks transitioning from intergranular to transgranular propagation and cracks consisting of cavities along grain boundaries. Two cracks close to the fracture surface were studied at the C alloy. The misorientation of grain boundaries close to the cracks were measured. These areas are marked in its respective figure. Figure 4.1 shows a crack from the sample taken with secondary electrons. The red dashed box indicates the area in Figure 4.3 where EBSD was performed. The blue dashed box indicates the area in Figure 4.2. The loading direction is also marked in the figure. The alloy and parameters for the creep test are given in the top left corners of each SEM image. This crack seem to have propagated 45° compared to the fracture surface.

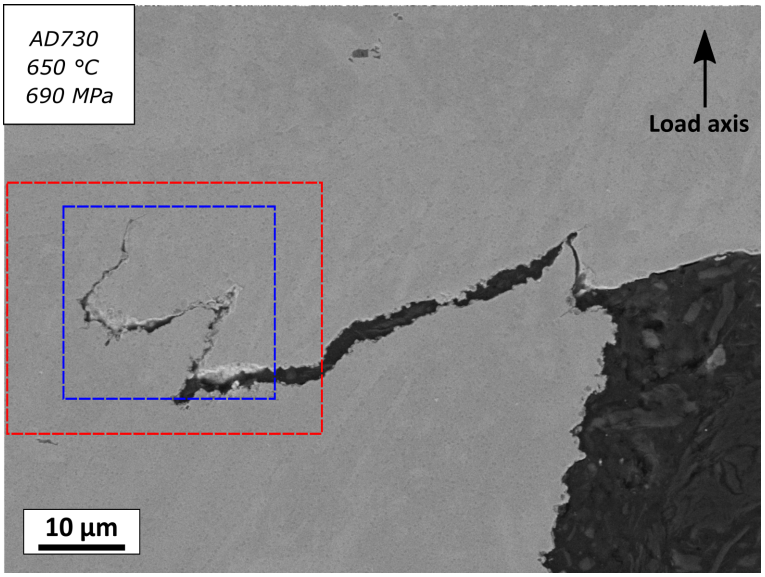

Figure 4.1: Crack found close to the fracture surface of the C alloy imaged with secondary electrons. The red dashed box indicates the area of the IPF-map in Figure 4.3 and the blue box indicates the area of Figure 4.2.

Figure 4.2 shows the same crack as Figure 4.1 taken with backscattered electrons. In this figure oxides seem to be present inside the crack as the oxides have a color contrast from the nickel.

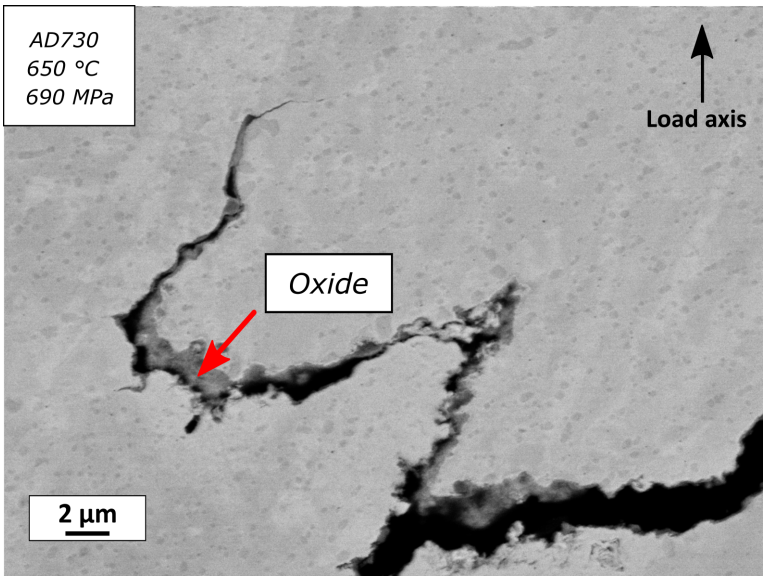

Figure 4.2: The same crack as in Figure 4.1 imaged with backscattered electrons.

Figure 4.3 shows an IPF-X map of the same crack as Figure 4.1 and 4.2, where one can see that the crack seems to have propagated intergranulary. The misorientation between grains was measured at three areas marked with a red line and a letter for each area. Grain boundaries with an angle of 15° or more are defined as high angle grain boundaries and marked with black in the IPF map. The values for misorientation is presented in Table 4.1. The crack is marked with red arrows. The black unidentified areas seem to be the crack and oxides inside and around the crack. It could possibly also be areas with high deformation.

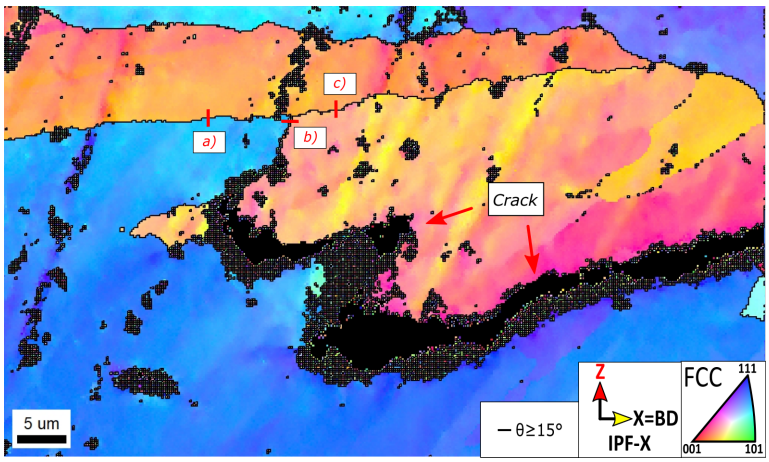

Figure 4.3: IPF-X map of the crack presented in Figure 4.1 and 4.2. The crack is marked with red arrows. The red lines a)-c) indicates where the misorientation was measured.

Figure 4.4 shows another crack found close to the fracture surface of the C alloy. This image is captured with secondary electrons. This crack also seem to have propagated at around 45° with respect to the fracture surface.

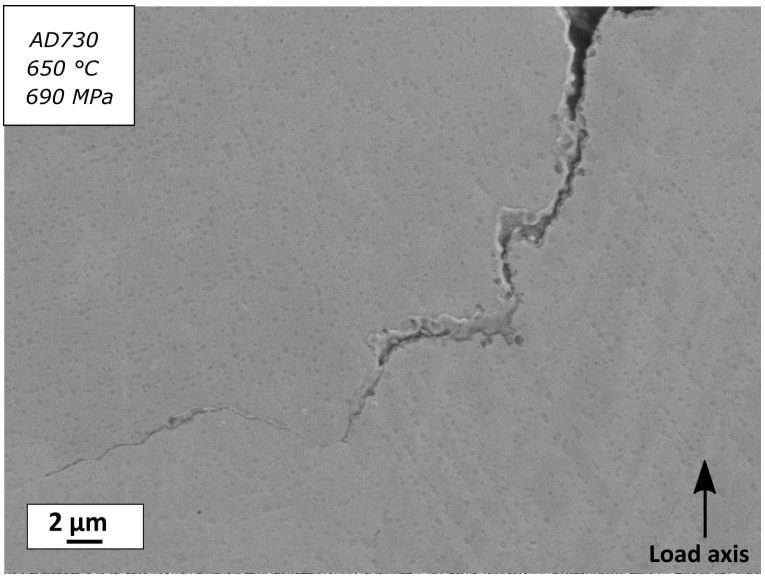

Figure 4.4: Another crack found close to the fracture surface of the C alloy. This image is taken with the secondary electron mode.

Figure 4.5 shows the same crack as in Figure 4.4 with backscattered electrons. Oxides also seem to be present inside this crack.

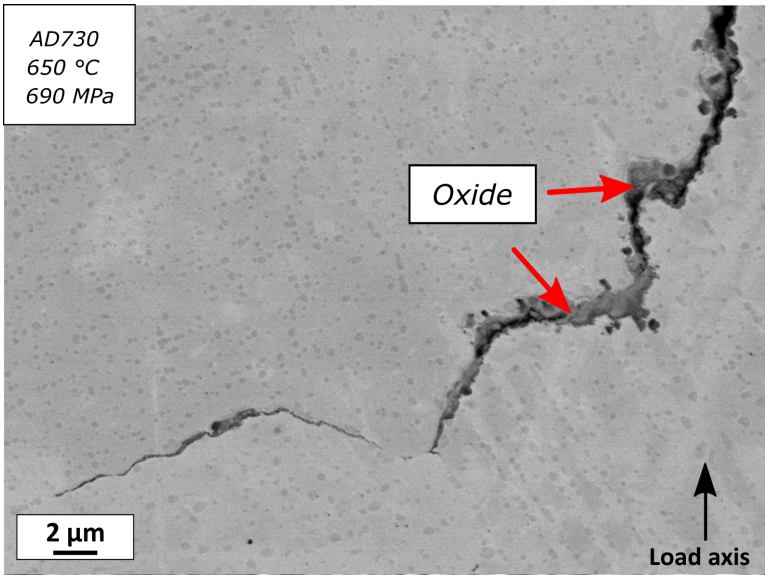

Figure 4.5: The same crack as in Figure 4.4 taken with backscattered electrons.

An IPF-X map of the crack in Figure 4.4 and 4.5 is given in Figure 4.6. This crack also seem to have propagated along a high angle grain boundary. The misorientation of three grain boundaries were measured in this IPF-map and is presented in Table 4.1.

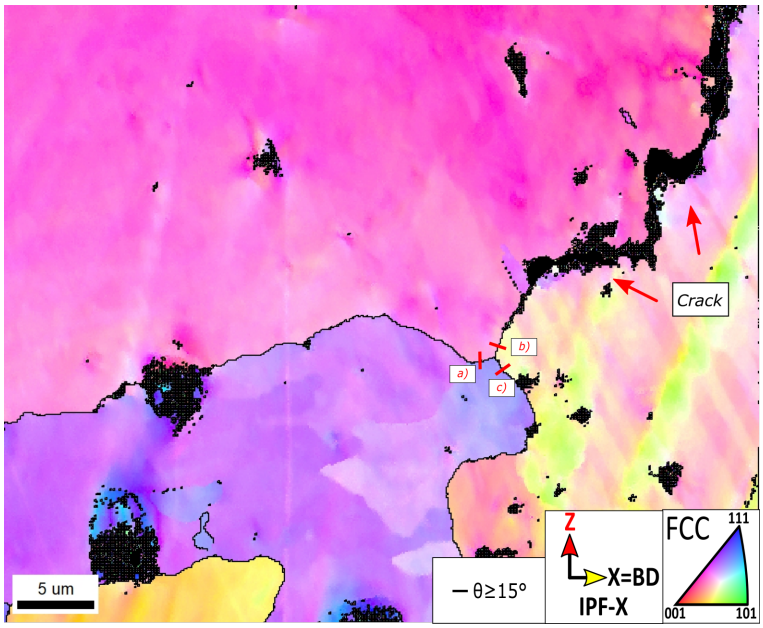

Figure 4.6: IPF-X map of the crack given in Figure 4.4 and 4.5. The crack is marked with red arrows and the red lines a)-c) indicated where the angle of misorientation was measured.

Table 4.1 presents measured angle of misorientation from each IPF-map of both cracks.

Table 4.1: Angle of misorientation from measured areas in Figure 4.3 and 4.6.

Figure	Letter	Angle of misorientation
4.3	a	58.5°
4.3	b	36.6°
4.3	c	27.7°
4.6	a	46.9°
4.6	b	34.7°
4.6	c	57.3°

4.2 γ/γ' microstructure and volume fraction of γ'

Multiple lift-outs were prepared for both alloys and several APT samples were sharpened and analyzed. The sections below show the collected volumes by APT, alongside composition profiles and proxigrams of particular features that are necessary. The first reconstruction in Figure 4.7 shows an atom probe reconstruction of the CB alloy showcasing the γ and γ' phases. The γ' phase is marked with blue aluminium atoms while the γ is marked with chromium atoms in pink. The interfaces between the phases are marked with a pink iso-surface of chromium with an iso-value of 17.05at.%. An iso-surface is a visualization tool that highlights areas with a high concentration or density of the chosen elements by coloring the space in between each atom. Iso-surfaces can be used to highlight different phases, grain boundaries and precipitates. The red γ' symbol indicates an iso-surface where the proxigram in Figure 4.8 and 4.9 is measured. This reconstruction was used as a comparison to the C alloy to compare the γ/γ' microstructure.

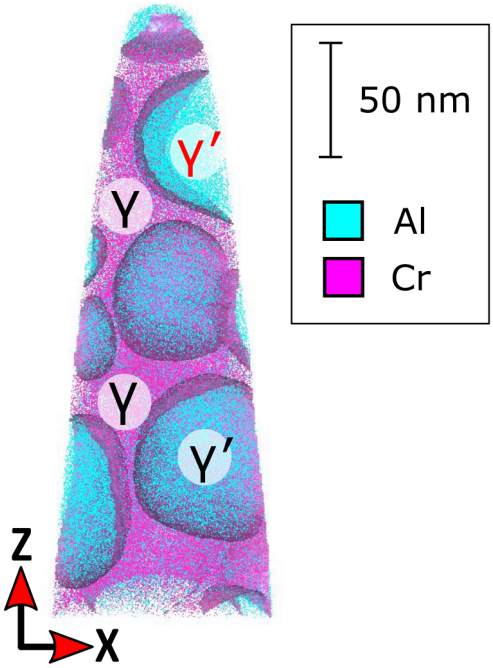

Figure 4.7: Atom probe reconstruction from CB. Each phase is marked with its corresponding symbol and the interfaces are marked with a pink iso-surface of chromium. The chromium atoms are in pink and aluminium atoms are in blue.

Figure 4.8 is a proxigram at the marked iso-surface in Figure 4.7 showcasing the difference in composition between the γ and γ' phases. A proxigram or proximity histogram, is an elemental composition profile measured as a function of distance from the chosen interface. The composition of γ' is given on the left and the composition of γ is given on the right. Each element and its corresponding curve are also given in the figure. The used bin size was 0.5 nm with a maximum distance of 10 nm. It is clear that Cr, Co and Fe mostly reside in γ, while Al and Ti reside in γ'. It seems as it is a higher nickel content in the γ' phase with 70 atomic% compared to γ with around 50 atomic%.

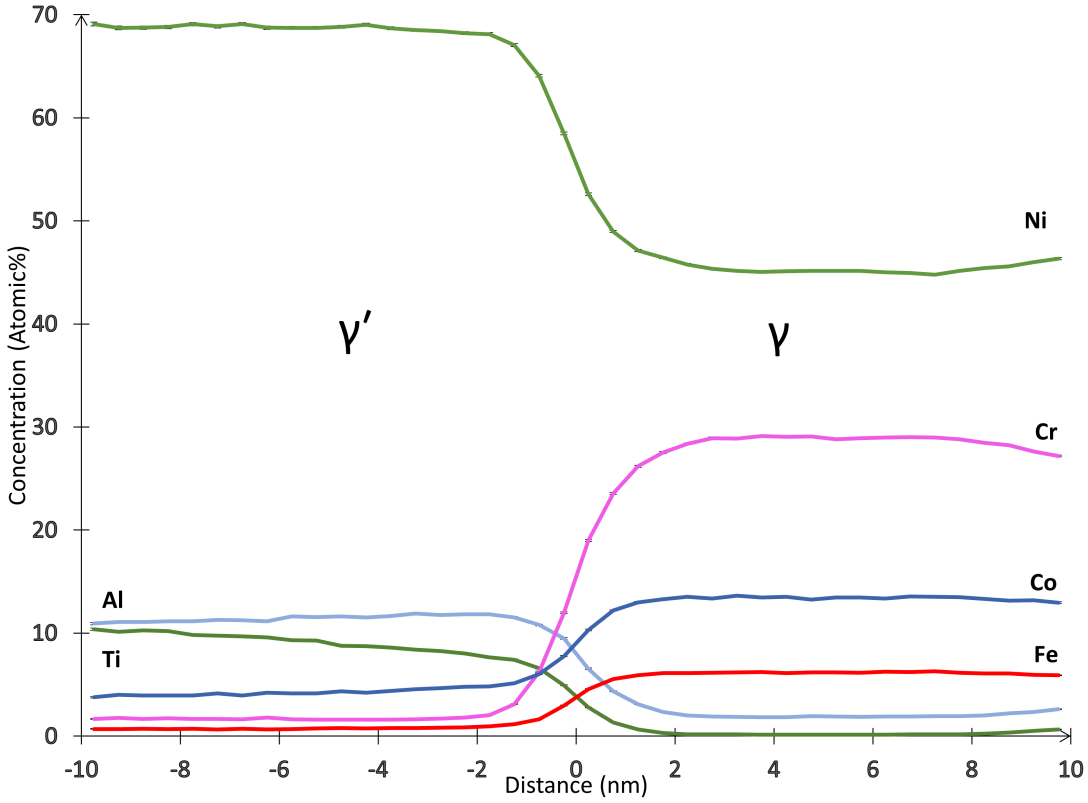

Figure 4.8: Proxigram from an iso-surface in the CB alloy. This figure shows the partition of solutes in γ and γ'. Error bars correspond to the 2σ counting error.

Figure 4.9 shows how the C and B composition varies in γ and γ'. Boron seems to mostly reside in γ compared to γ'. There is however an increased concentration on what might be the γ/γ' surface which reaches a value in the same range as the highest concentration in γ. Carbon does not seem to vary much between γ and γ'.

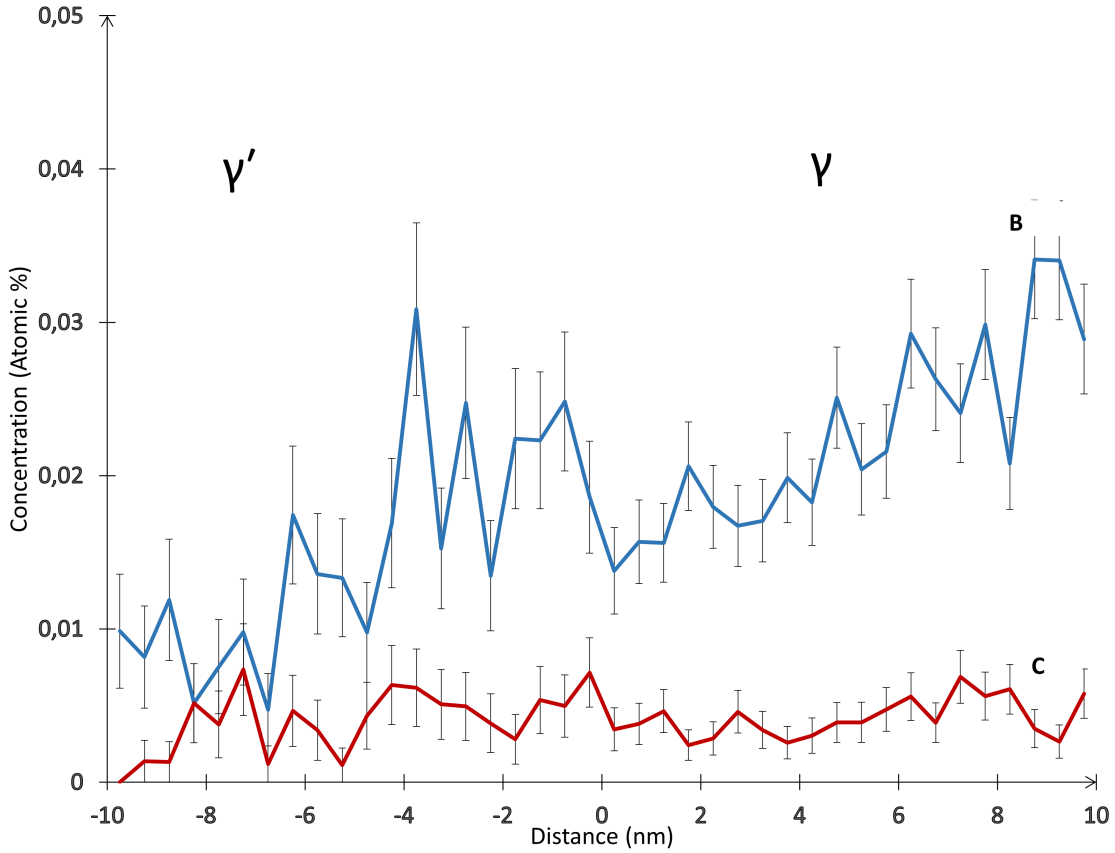

Figure 4.9: Proxigram from a γ/γ' iso-surface with the concentration of B and C in each phase. Each element is named at its respective curve. Error bars correspond to the 2σ counting error.

The lever rule method was used to calculate the volume fraction of γ' of the alloy. This was done by extracting the composition of each phase from the atom probe reconstruction by placing a squared region of interest (ROI) inside each phase without it touching the interfaces between the phases. The composition of each phase was then extracted by decomposing the peaks in the mass spectrum. These values are given in Table 4.2 with the atomic% of each element inside the phases and bulk material. The values for the bulk material are the same values given in Table 3.1 but with atomic%. This table also includes the atomic error percent for each phase and element. Only the elements that were found in both phases were used for the calculations.

Table 4.2: Table listing each alloying element and the atomic% of these inside each phase and the bulk material of CB. The composition of each phase is calculated from peak decomposition.

Ion	Atomic% - Bulk	Atomic% - γ	Atomic% - γ'
Nb	0,3	0,03 ±0,002	0,56 ±0,011
W	1	0,24 ±0,006	0,33 ±0,009
Mo	1,8	2,21 ±0,014	0,28 ±0,009
Al	4,9	0,57 ±0,013	13 ±0,040
Ti	3,7	0,16 ±0,006	13,50 ±0,037
Cr	18,1	30,9 ±0,045	0,94 ±0,015
Fe	4,2	6,91 ±0,026	0,59 ±0,019
Co	8,3	13,49 ±0,034	3,02 ±0,028
Ni	57,7	45,32 ±0,045	67,52 ±0,064

The values in Table 4.2 were then used to plot the curve given in Figure 4.10. The values on the x-axis are from calculating the composition of each element in γ' minus the composition in γ. The y-axis is the composition of the bulk material minus the composition in γ. When each element was plotted a linear regression line was plotted afterward. The slope of this regression line is equal to the volume fraction of γ' inside the CB alloy. In this case it was calculated to be around 44%. Each element is marked in the graph.

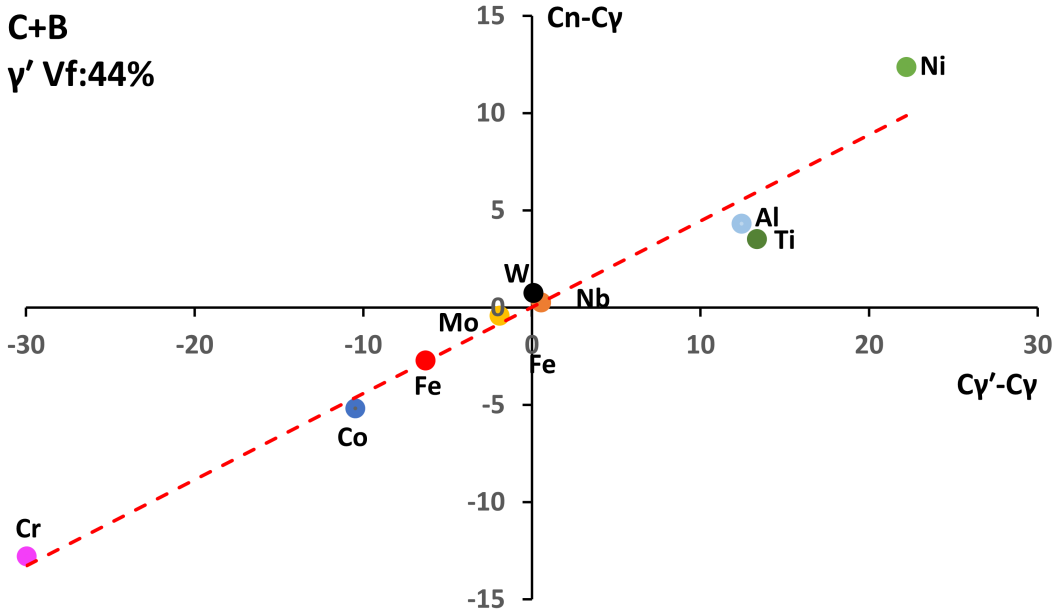

Figure 4.10: Curve used to calculate the volume fraction of γ' with the lever rule method. Each element is marked in the figure.

The main reason for studying the C alloy was to measure the composition of γ and γ' of the alloy in order to calculate the volume fraction of γ' and compare this with the results from the CB alloy. This could have an effect on the creep properties of the alloys as γ' is what often provides the strength to the alloys. If both alloys have a similar volume fraction of γ' the difference in creep resistance is most likely a result of the boron addition. Figure 4.11 presents an atom probe reconstruction from the C alloy. γ and γ' are marked in the reconstruction. The red symbols and line indicate the iso-surfaces where proxigrams were created. The chromium iso-surface and atoms are colored in pink and aluminium atoms are in blue. The chromium iso-surface has an iso-value of 5.05at.%. The lower part of the figure contains a large γ' with γ particles inside.

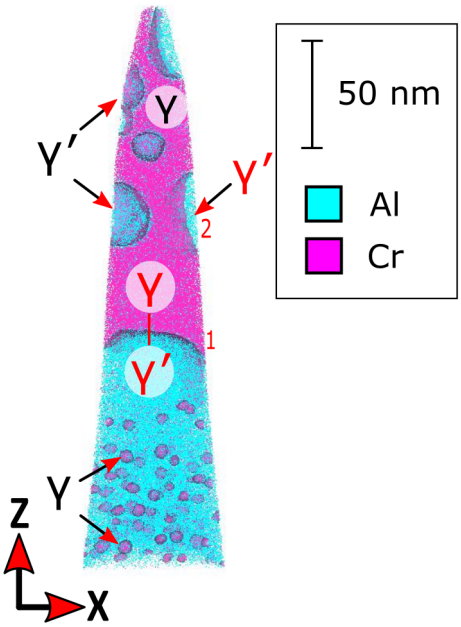

Figure 4.11: APT reconstruction of the C alloy with each phase indicated by its respective symbol. The red symbols, numbers and line indicate where the proxigrams in Figure 4.12 and 4.13 was measured.

Figure 4.12 is a proxigram from the large chromium iso-surface at the lower part of Figure 4.11 marked with a red line and (1. The area of γ is given on the right and for γ' on the left. Each element is marked in the figure in the area of the corresponding curve. γ seems to contain mostly Cr, Co and Fe while γ' seems to be mostly Al and Ti of the given elements. The nickel content in γ seems to be around 46-50 atomic% compared to around 70 atomic% in γ'. The maximum distance for this proxigram was at 10 nm with a bin size of 0.5. It was not observed any carbon in the C alloy with APT. This might be a result of the carbon being mostly around the grain boundaries in the sample.

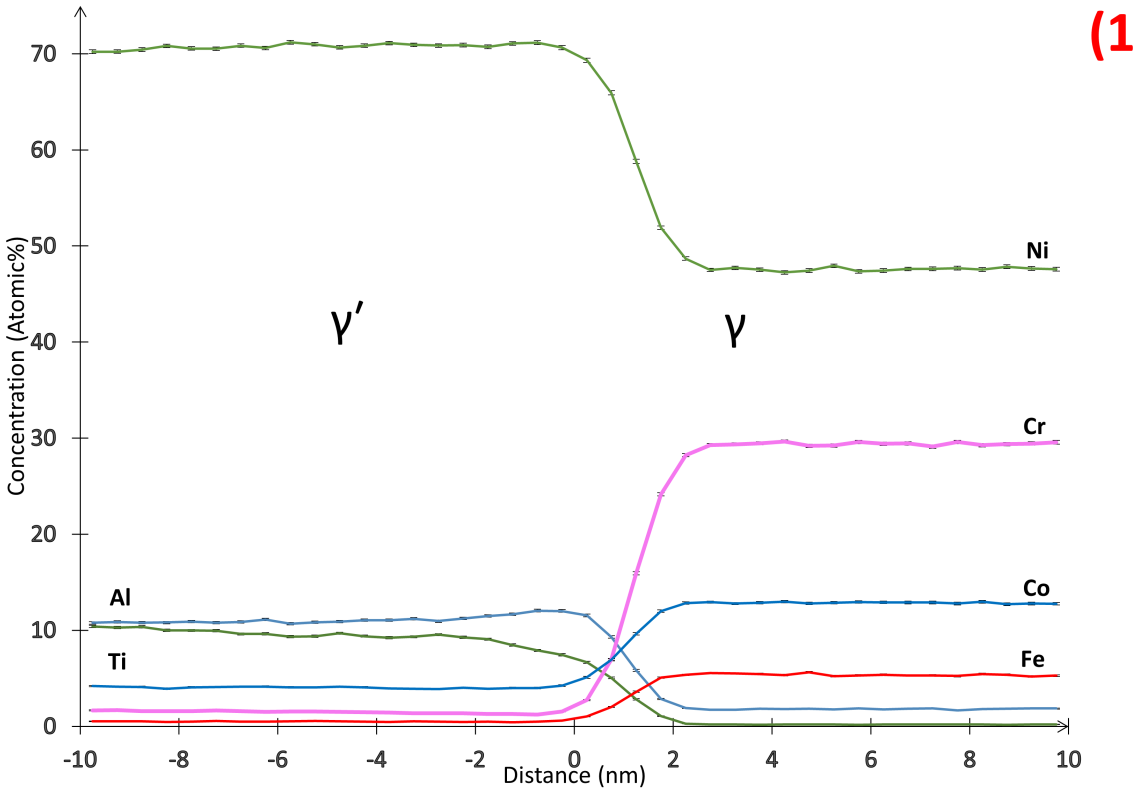

Figure 4.12: Proxigram of the γ/γ' transition in the C alloy with the concentration of five selected elements. Error bars correspond to the 2σ counting error.

Figure 4.13 presents a proxigram from the chromium iso-surface marked in the middle of the reconstruction in Figure 4.11 with (2. This proxigram showcases the concentration of Al, Ti, Co, Fe and Cr in γ' given on the left and γ on the right. The content of nickel seems to be almost identical to the values in Figure 4.12. The maximum distance for this proxigram was at 10 nm with a bin size of 0.5. Each element is named in proximity to its respective curve.

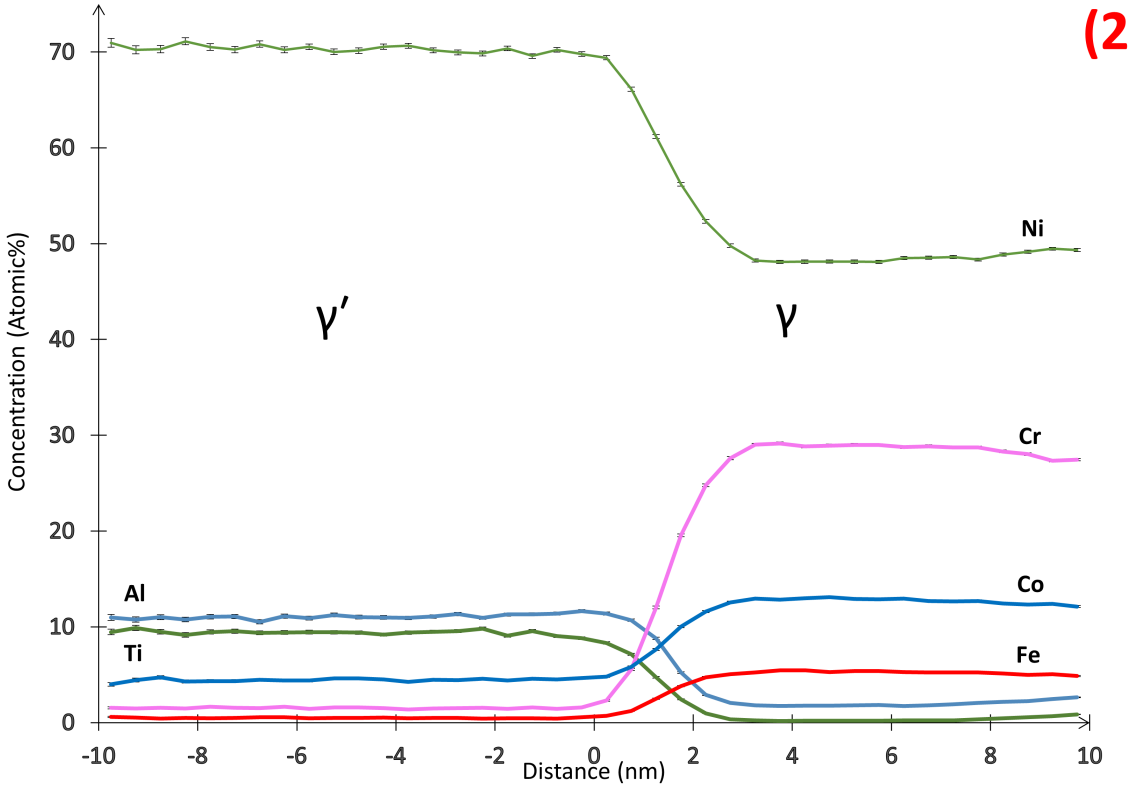

Figure 4.13: Proxigram of γ and γ' with the composition of given elements. Error bars correspond to the 2σ counting error.

Table 4.3 presents measured compositions in the bulk material and in γ and γ' from cubic ROIs. Each element is listed in atomic% including the atomic% error. These values were used to calculate the volume fraction of γ' in the C alloy. These are all elements that were identified in both phases.

Table 4.3: Table listing each alloying element and the atomic% of these inside each phase and the bulk material of C. The composition of each phase is calculated from peak decomposition.

Ion	Atomic% - Bulk	Atomic% - Gamma	Atomic% - Prime
Nb	0,6	0,05 ±0,003	0,97±0,009
W	1	0,3 ±0,007	0,19 ±0,005
Mo	1,8	1,44 ±0,013	0,30 ±0,005
Al	4,9	0,66 ±0,011	11,5 ±0,027
Ti	4,3	0,25 ±0,006	12,3 ±0,028
Cr	17,9	30,9 ±0,037	1,2 ±0,011
Fe	3,8	6,42 ±0,024	0,69 ±0,015
Co	7,9	12,3 ±0,031	2,46 ±0,018
Ni	57,8	47,5 ±0,051	70,3 ±0,044

The calculated values from Table 4.3 was used to construct the curve in Figure 4.14. Each element is plotted in the graph with a linear regression line constructed from all the points. The slope of this line gave a volume fraction of ca. 43% of γ' in the C alloy, which is around the same value as for the CB alloy. The values on the x-axis are from calculating the composition of each element in γ' minus the composition in γ. The y-axis is the composition in the bulk material minus the composition in γ. The composition of γ' was measured inside the large γ' precipitate seen in Figure 4.11. The volume fraction was also calculated using one of the smaller γ' precipitates. These gave a minimal difference in volume fraction.

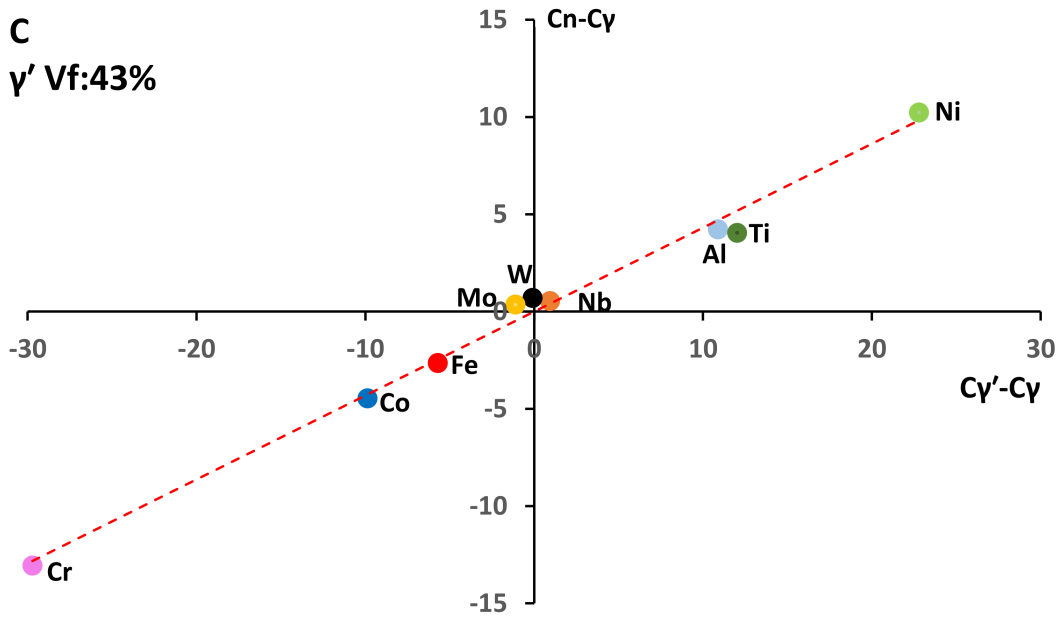

Figure 4.14: Curve used to calculate the volume fraction of γ' in the C alloy with the lever rule method. Each element is plotted by calculating the differential between the composition in γ and in γ' and the bulk material.

4.3 Grain boundary segregation

The volume fraction of γ' in the CB and C alloys was shown to be almost identical, meaning the great variation in creep resistance between the alloys is a result of the boron in the CB alloy. Boron is said to increase the creep resistance of alloys by segregating at grain boundaries which is why the main interest in the CB alloy was boron and its segregation in the microstructure. A possible grain boundary was only found in one of the reconstruction volumes. This reconstruction did however include a lot of interesting features as seen in Figure 4.15 which shows an iso-surface of boron marking the grain boundary in the CB alloy. This reconstruction also includes other interesting aspects as possible dislocations around the grain boundary and a particle surface. This particle is shown later in Figure 4.29 and 4.30 and is assumed to be a carbide. The boron iso-surface has an iso-value of 0.3at.%. Aluminium iso-surfaces and atoms are marked in blue while pink atoms are chromium atoms. The volume inside the red dashed boxes is presented in Figure 4.16. a) shows the reconstruction without any boron iso-surfaces. In b) only boron iso-surfaces are shown to better highlight the grain boundary in the reconstruction, as the aluminium iso-surfaces would obscure the boundary. The location of some γ and γ' phases is also marked in this figure.

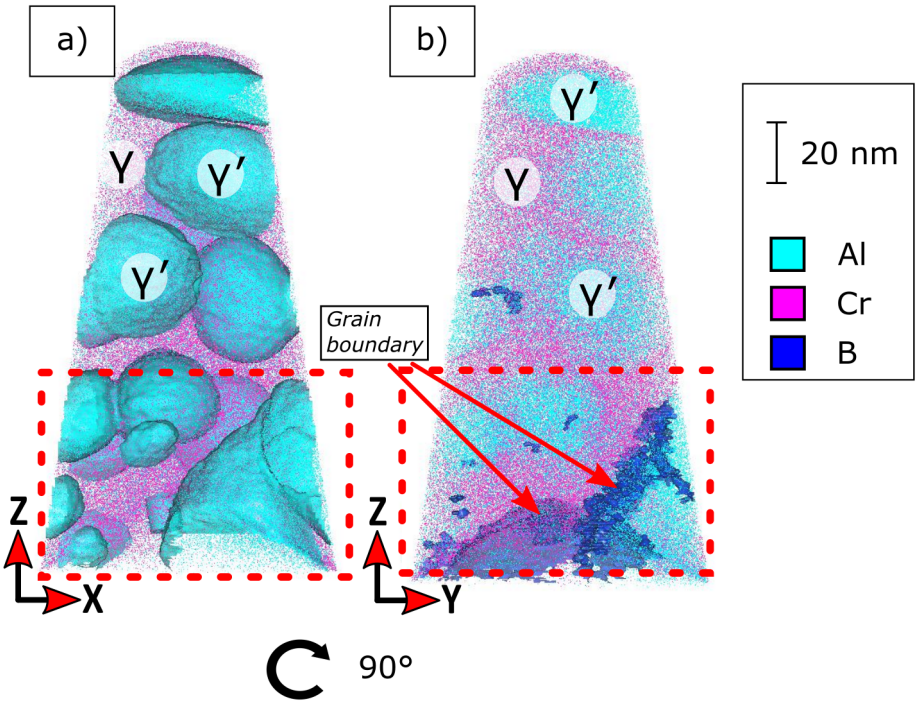

Figure 4.15: Reconstruction from the CB alloy showcasing a possible grain boundary. a) shows the microstructure without any boron and b) only has boron iso-surfaces to show the shape of the grain boundary.

A cut-out of the reconstructions with the grain boundary is presented in Figure 4.16. a) and b) shows the iso-surfaces without the aluminium iso-surfaces to highlight the shape of the possible grain boundary. The grain boundary is marked with green dashed lines in b). Multiple boron iso-surfaces are shown in a), which could be a mix of grain boundary and dislocations. In b) it is a red arrow marked with (1). This arrow indicates the direction and location of the cylindrical ROI used to plot the concentration profiles given in Figure 4.17 and 4.18. The other red arrow marked with (2) marks where Figure 4.19 was measured.

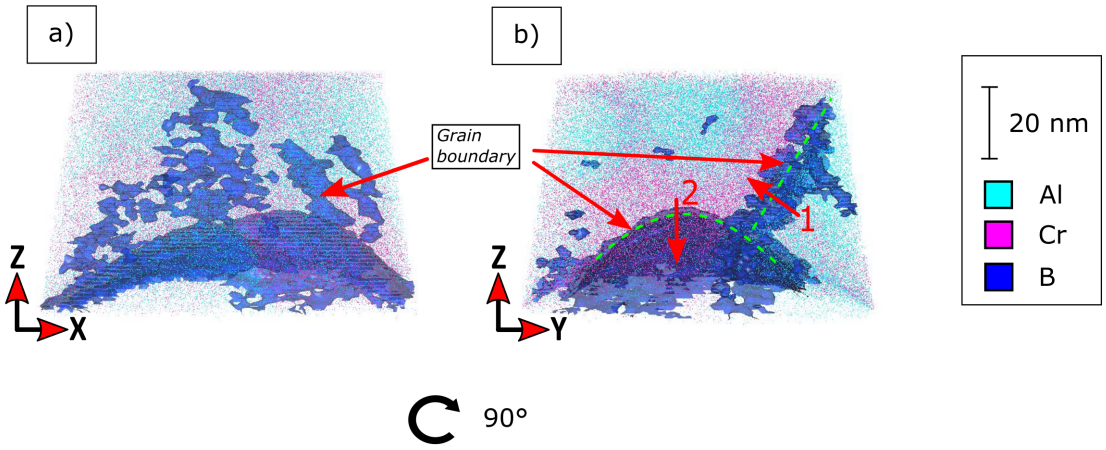

Figure 4.16: Atom probe reconstruction from the CB alloy showcasing a possible grain boundary in a) and b). The grain boundary is shown with a boron iso-surface. This figure shows the boron iso-surface without other iso-surfaces to better highlight the shape of the grain boundary.

Figure 4.17 is a composition profile showcasing the composition of the grain boundary given in Figure 4.15 and 4.16. A composition profile is a one-dimensional plot of the composition along a specified region of interest. This composition profile is made by using a cylindrical ROI perpendicular to the grain boundary. This composition profile showcases the concentration of boron and carbon at the grain boundary. It seems to be mostly boron with a peak value of around 0.4 at.%. Multiple measurements were done at the boron iso-surfaces above the carbide surface. Most peak values landed around the same maximum values with varying ROI size, angle and placements.

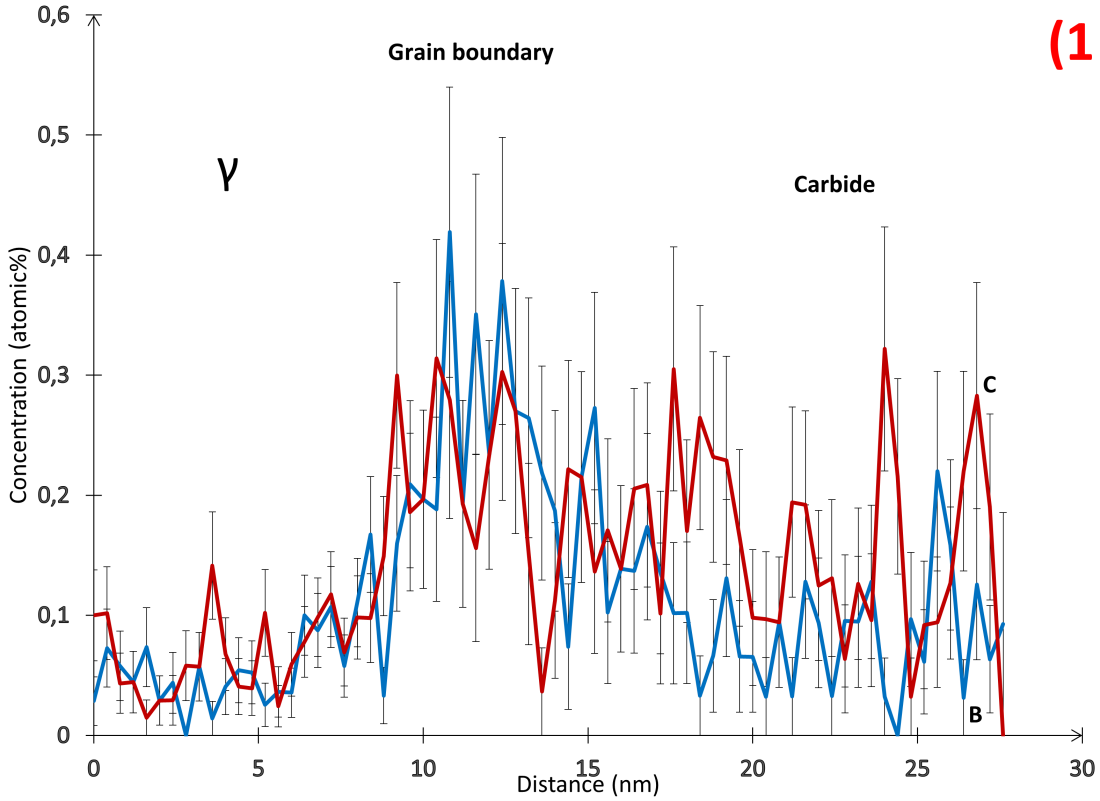

Figure 4.17: Composition profile showcasing the concentration of boron and carbon in a chosen area of the possible grain boundary. This area is marked as (1) in Figure 4.16. Error bars correspond to the 2σ counting error.

The composition profile in Figure 4.18 also shows the concentration of molybdenum in the grain boundary, as Mo also seems to have an increased value at the boundary. The concentration of Mo seem to peak at around 2.5 at.%.

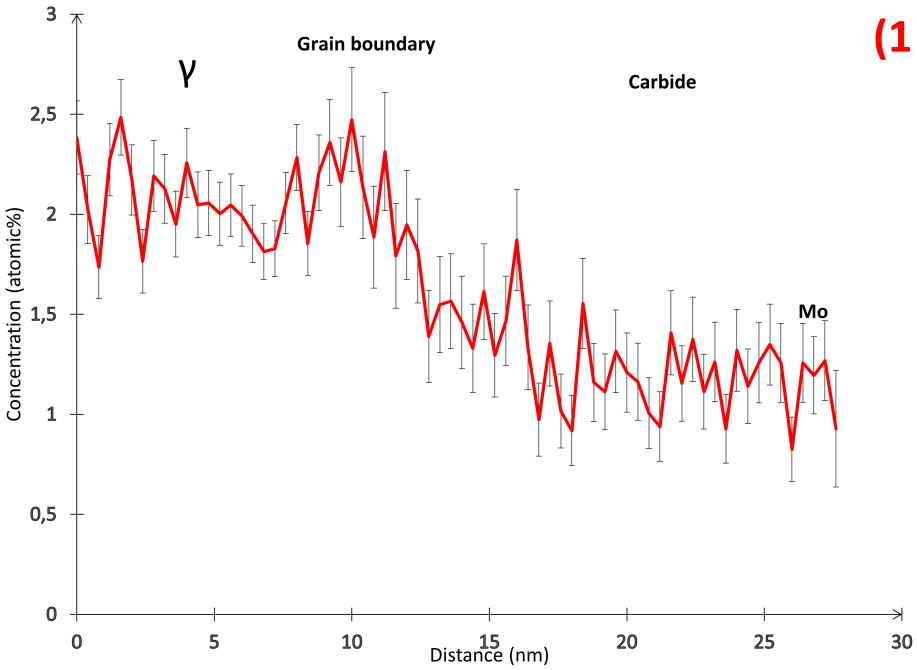

Figure 4.18: Composition profile including the concentration of molybdenum in the possible grain boundary Error bars correspond to the 2σ counting error..

Figure 4.19 shows a composition profile measured at the red arrow marked as (2) in Figure 4.16. This composition profile presents the concentration of boron at the carbide interface with a maximum value of ca. 8 at.%.

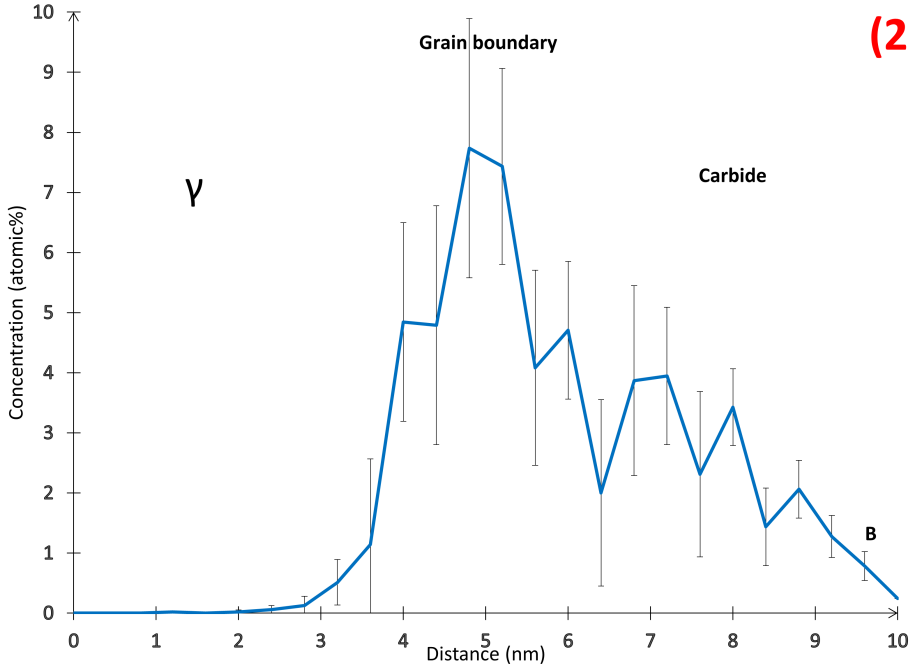

Figure 4.19: Composition profile with the boron concentration in the carbide surface. Error bars correspond to the 2σ counting error.

4.4 Segregation on dislocations

Multiple attempts of trying to include a grain boundary in the APT samples gave some very interesting observations despite of no grain boundaries observed in the reconstructions. These reconstructions had instead small boron enrichments as shown in Figure 4.20. This figure shows an atom probe reconstructions from the CB alloy with an enrichment of boron marked with a red arrow and an iso-surface in dark blue. This enrichment can potentially correspond to segregation of boron to a dislocation. The boron iso-surface has an iso-value of 0.22at.%. Aluminium is marked with a lighter blue color and chromium is marked with pink atoms. It is also an iso-surface of chromium present with a value of 17.05at.%. a) and b) is the same reconstruction with a 90°rotation. An enlarged area with the enrichment is shown in Figure 4.21 indicated by the red dashed box.

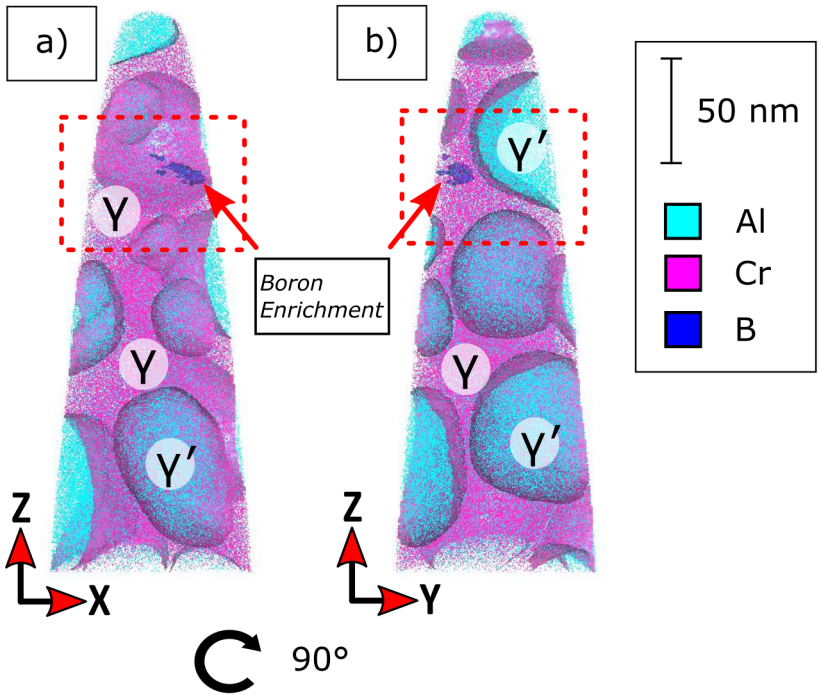

Figure 4.20: Atom probe reconstruction from the CB alloy with an iso-surface of boron showcasing a boron enrichment. The iso-surface of boron is in a dark blue and the iso-surface of chromium is in pink. The aluminium atoms are in light blue and chromium is in pink. a) and b) is from the same reconstruction with a 90°rotation to show the shape of the enrichment.

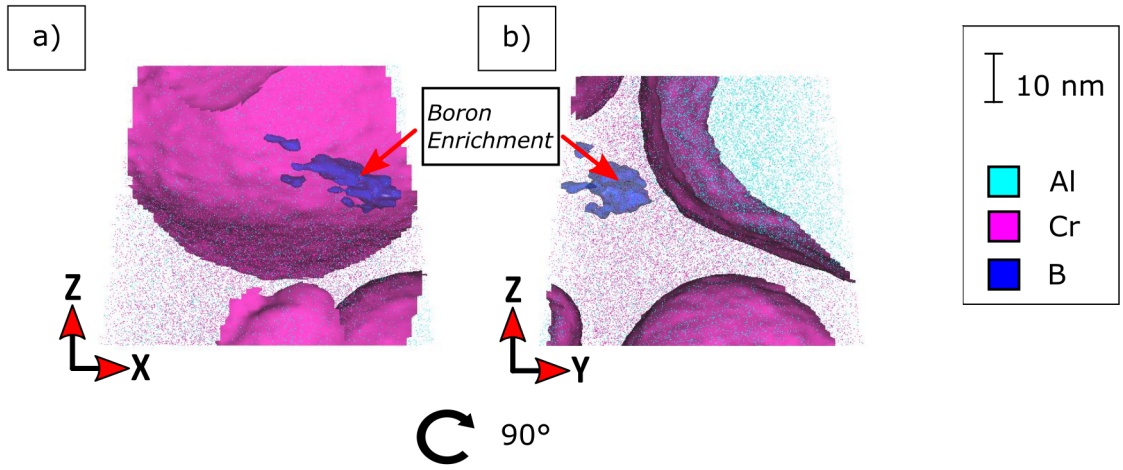

Figure 4.21: Iso-surface of a boron enrichment from the CB alloy. The iso-surface of boron is in a dark blue while aluminium atoms are in light blue and the chromium atoms and iso-surface is in pink. a) and b) is from the same reconstruction with a different angle.

A composition profile of the boron enrichment in Figure 4.21 is given in Figure 4.22. The highest amount of boron is in the middle of the profile with a value of around 0.7 atomic%. The concentration of carbon does not seem to peak anywhere in the profile. Mo seems to have an increased concentration in the same area as B. It also seems to be a depletion of Al in this area. The distance of the composition profile is of 10 nm with a bin size of 0.5 nm.

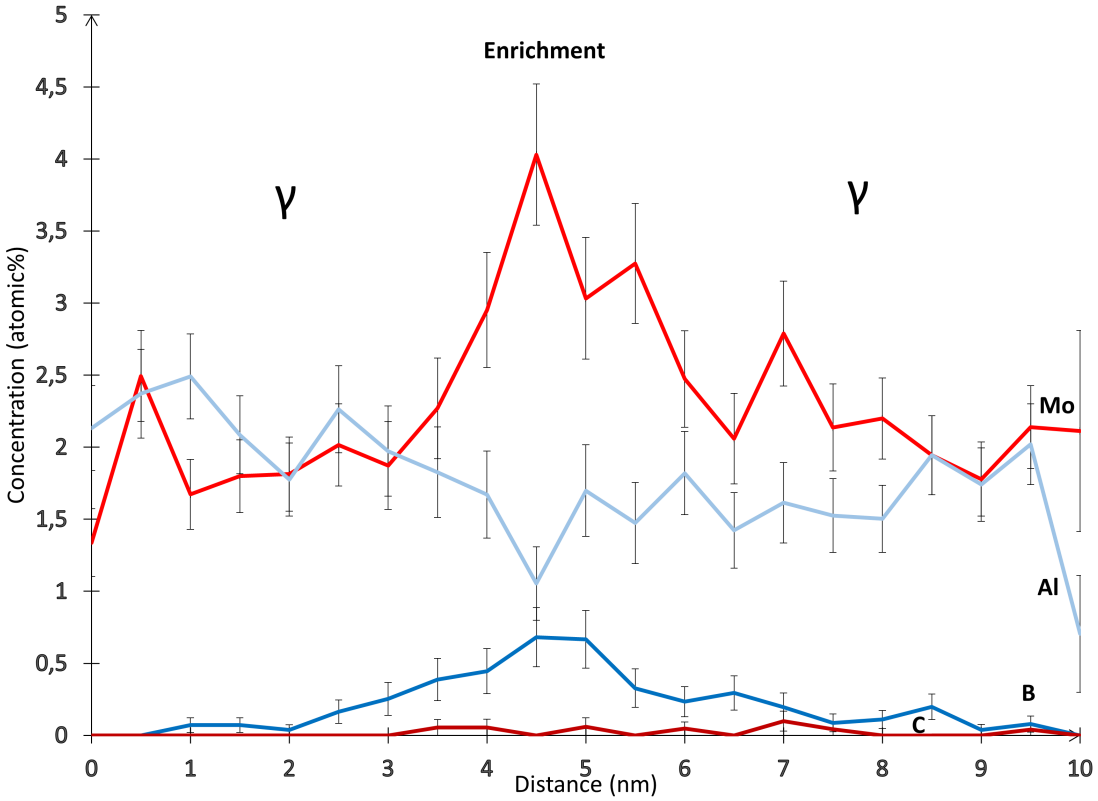

Figure 4.22: Composition profile from the CB alloy showcasing the concentration changes of B, C, Mo and Al around the B concentration found in the reconstruction. Error bars correspond to the 2σ counting error.

The boron enrichment found in the last reconstruction was not expected and it was not found anything similar in the literature. These enrichments were therefore studied further by studying more samples with the same observations to have statistically enough observations of these enrichments. Another example is therefore given in Figure 4.23 where the observed enrichment is marked with red arrows. This boron enrichment is marked with an iso-surface in a dark blue and has an iso-value of 0.22at.%. Aluminium is marked with a lighter blue color and chromium is marked with pink atoms and a pink iso-surface with an iso-value of 12.3at.%. This reconstruction consisted of large γ' precipitates. The red dashed boxes indicate the areas in Figure 4.24.

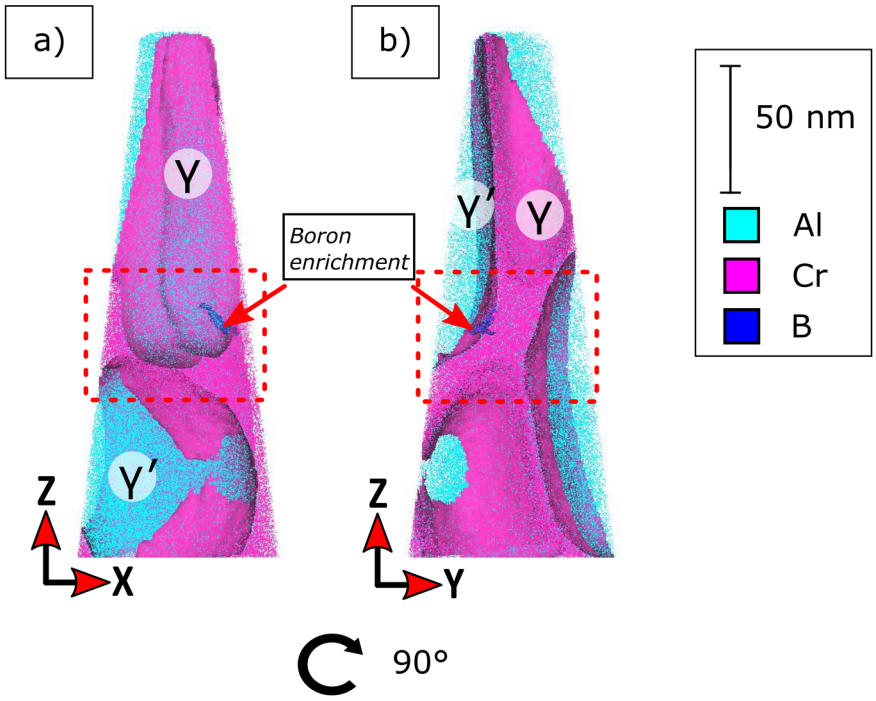

Figure 4.23: Boron enrichment spotted in an atom probe reconstruction in CB. The iso-surface of boron is in a dark blue. Aluminium atoms are colored in light blue and chromium atoms are in pink.

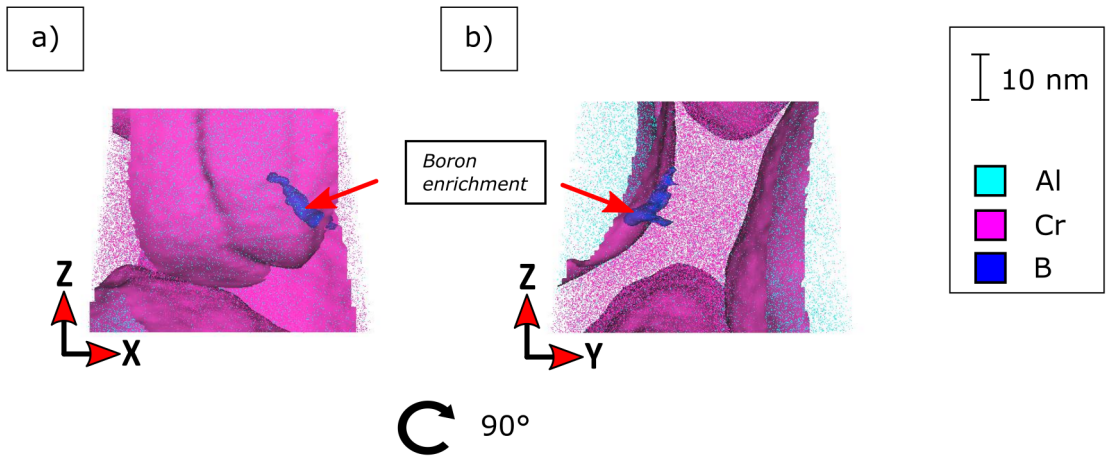

Figure 4.24: Zoom-in on the reconstruction given in Figure 4.23. Aluminium atoms are colored in blue and chromium atoms are colored pink. The iso-surface for chromium is in pink and the iso-surface for boron is in a darker blue.

Figure 4.25 shows a composition profile of the boron enrichment given in Figure 4.23 and 4.24. The composition is measured over a distance of 10 nm with a bin size of 0.5. The largest measured value of boron is ca. 1at.% for this boron enrichment. The Mo concentration seems to increase with increasing B concentrations with a maximum concentration of around 6at.%. The concentration of carbon does not seem to have any peaks present. The aluminium content was not included in this proxigram as it showed no clear depletion. This might be a result of few aluminium ions being in this area of the reconstruction.

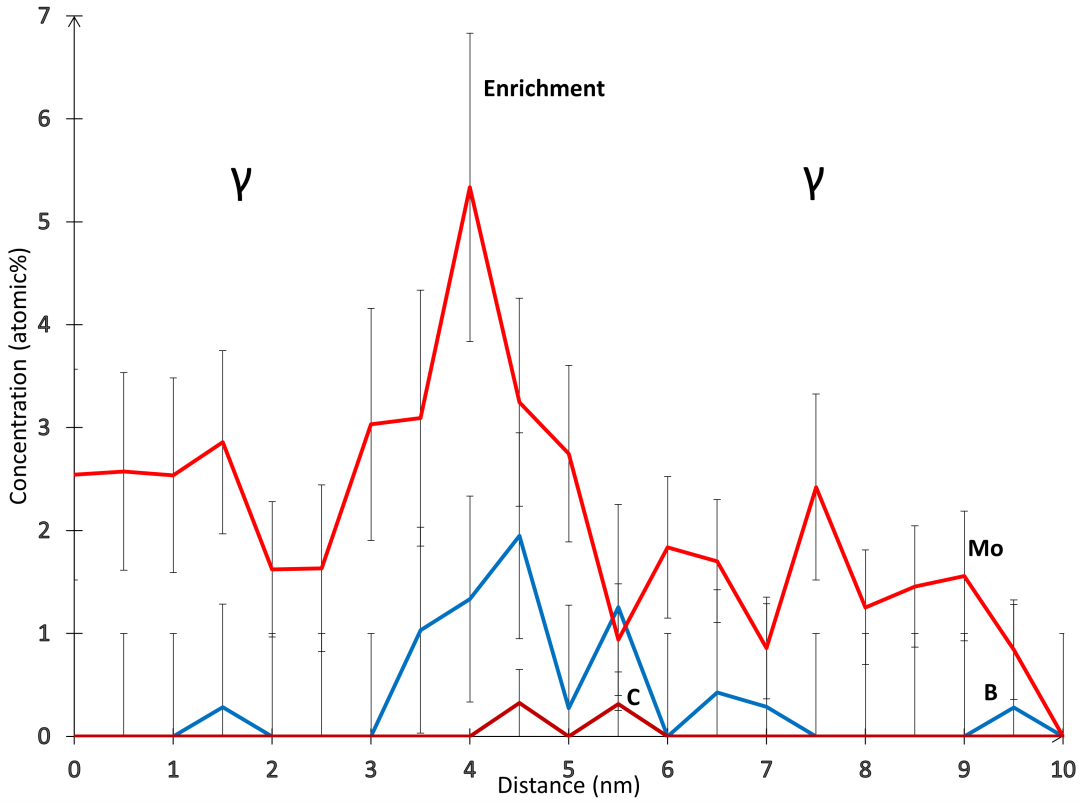

Figure 4.25: CB alloy composition profile of a boron enrichment showcasing the variation in concentration of B, C, and Mo. Error bars correspond to the 2σ counting error.

Figure 4.26 shows the final atom probe reconstruction from CB where an enrichment was spotted. The location of this enrichment is marked with red arrows. The iso-surface of boron is however obstructed from the chromium iso-surfaces. Later figures will therefore help in showcasing this boron enrichment. The boron iso-surface is in a darker blue with an iso-value of 0.002at.%. The chromium iso-surfaces are in pink and have a value of 15.74at.%. The red dashed boxes indicate the area showcased in later figures. Aluminium atoms are colored in blue while chromium atoms are in pink. a) and b) is from the same reconstruction with a 90°rotation.

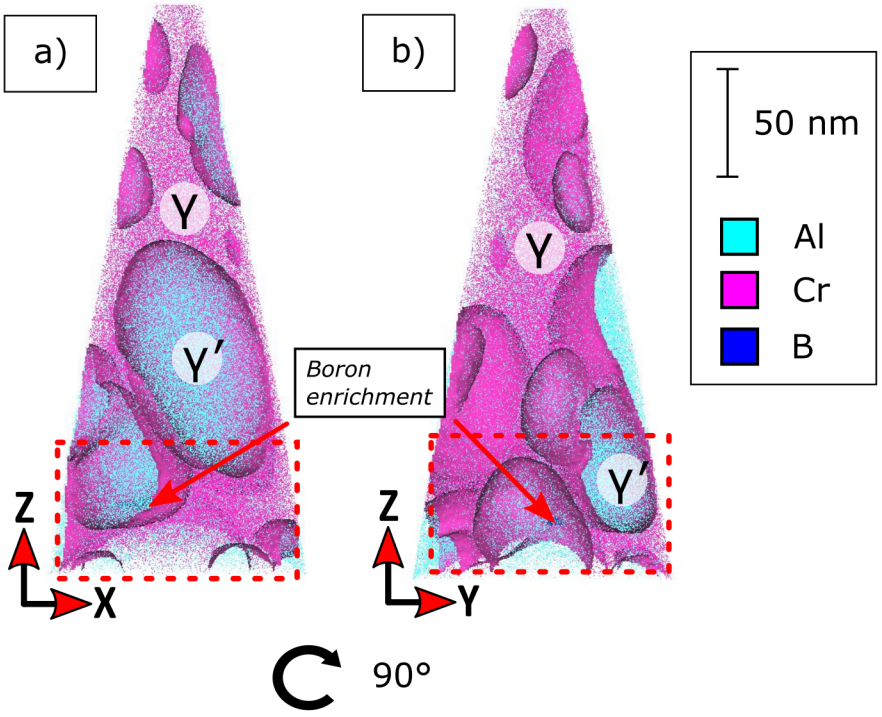

Figure 4.26: APT reconstruction from the CB alloy with a boron enrichment. This reconstruction includes pink chromium atoms and aluminium atoms with also pink chromium iso-surfaces. The boron enrichment is in a darker blue.

Cut-outs from the reconstruction given in Figure 4.26 is presented in Figure 4.27. a) and b) shows the reconstruction from the side from different angles while c) and d) show it from the top and underneath. The boron enrichment is marked with a blue iso-surface. This is the longest boron enrichment spotted in the CB alloy. The enrichment seems to reside on the γ/γ' surface with some parts inside each phase.

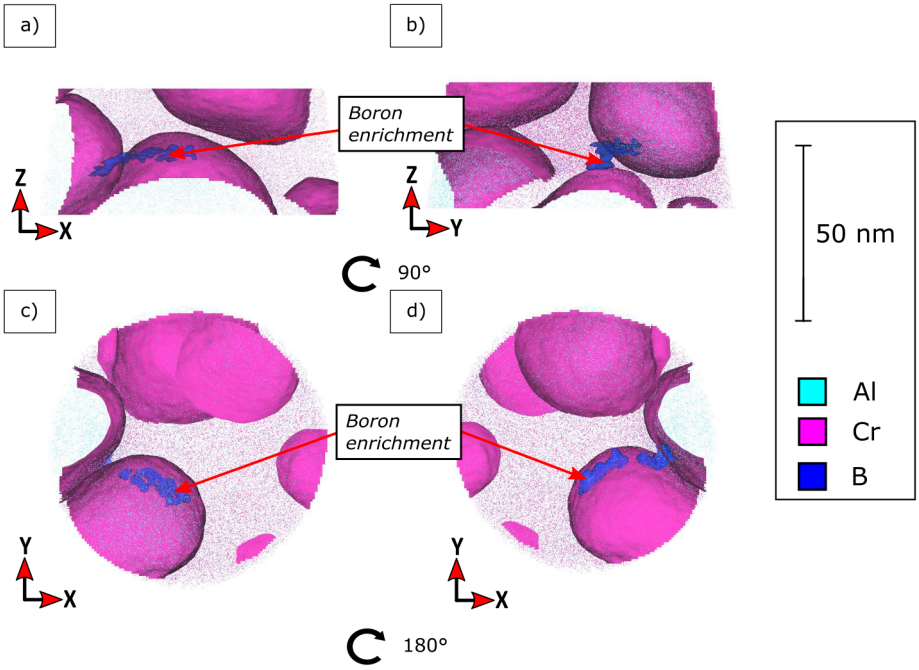

Figure 4.27: Cut outs of the reconstruction with the third boron enrichment found in the CB alloy. The dark blue iso-surface is of boron and the pink iso-surfaces are chromium. a)-d) shows the same boron enrichment in the reconstruction from four different angles.

Figure 4.28 shows a composition profile of the boron enrichment found in the reconstruction. This profile covers a distance of 10 nm with a bin size of 0.5. The highest concentration value for boron seems to be around 1.2 atomic%. Note that all composition profiles show different maximum values of boron for each enrichment. This could for example be a result of the enrichments being boron segregating at different types of dislocations.

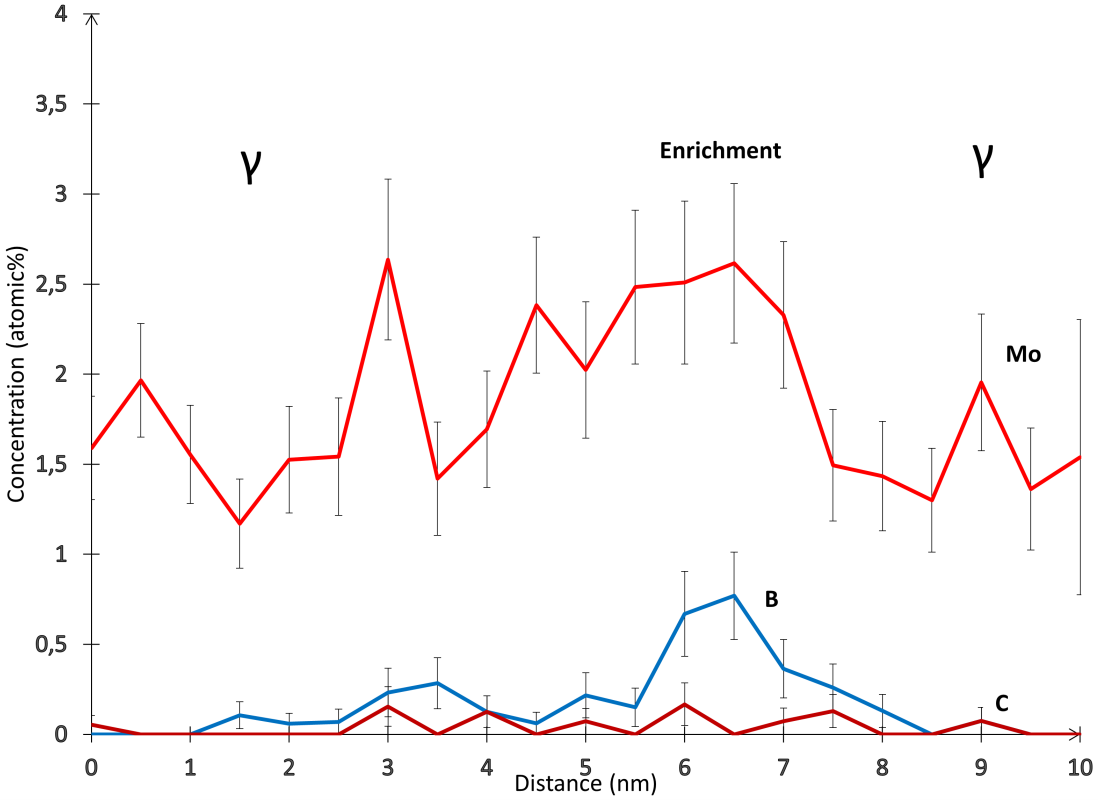

Figure 4.28: Concentration of B, C and Mo plotted in a concentration profile from the CB alloy. Both Mo and B have a peak between 4 and 6 nm in distance. Error bars correspond to the 2σ counting error.

4.5 Intergranular particle

The reconstruction in Figure 4.15 contained a lot of interesting features including a particle found at the bottom of the reconstruction. This particle is assumed to be a carbide, and could have big implications on the microstructure around it including the grain boundary that is above it and seems to go along the particle surface. This particle is presented in Figure 4.29 with a red iso-surface of carbon with an iso-value of 2.03at.%. Aluminium atoms and iso-surface is marked in blue and chromium atoms are in pink. The aluminium iso-surface has an iso-value of 5.35at.%. Both a) and b) given in Figure 4.29 shows the same reconstruction from different angles. The red dashed box indicates the volume of the reconstruction given in Figure 4.30, which shows images closer to the carbide.

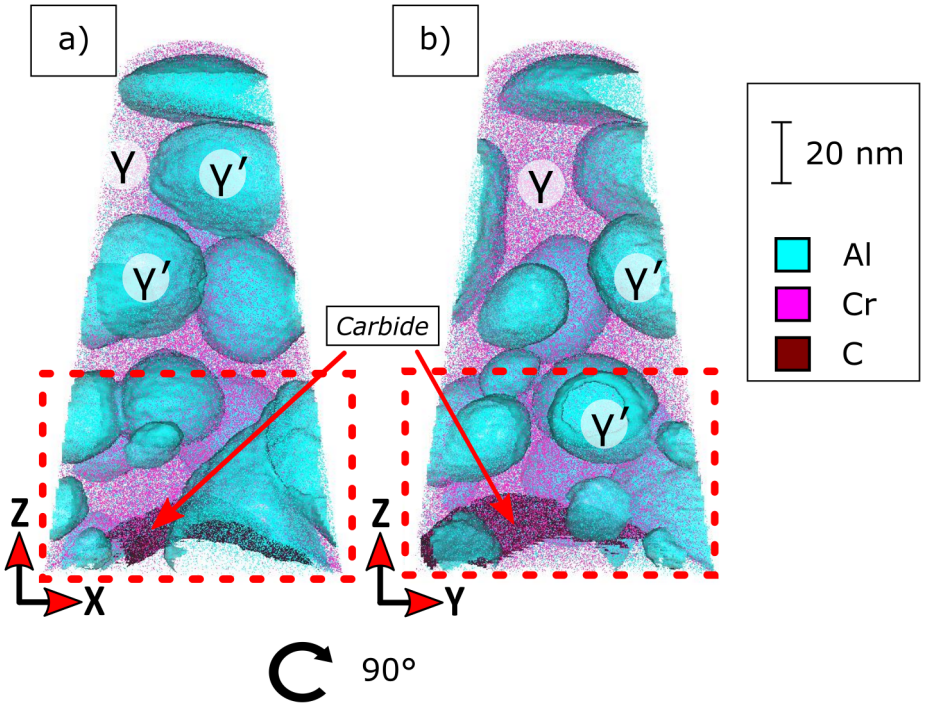

Figure 4.29: APT reconstruction from a sample milled out of the CB superalloy sample. Each phase and a carbide are marked in this figure. Aluminium atoms and iso-surfaces are colored blue and chromium in pink. Finally, the carbide is marked with a red iso-surface.

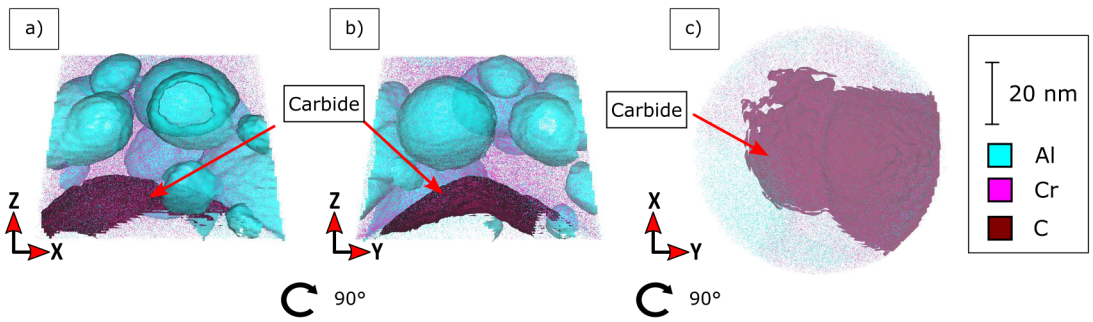

Figure 4.30: Cut out of the reconstruction in Figure 4.29 showcasing the carbide surface from two different angles in a) and b). c) showcases the carbide from above.

Multiple proxigrams were created from the particle iso-surface to find the chemical composition of the particle. The first proxigram given in Figure 4.31 include elements that have a drastic change in their value when analyzing outside and inside the particle volume. The volume of the particle is given on the right side of the proxigram. It is clear that it is a depletion of chromium and iron inside the particle volume. The values for carbon and titanium increase drastically inside the particle volume however, indicating that this particle might be a titanium carbide.

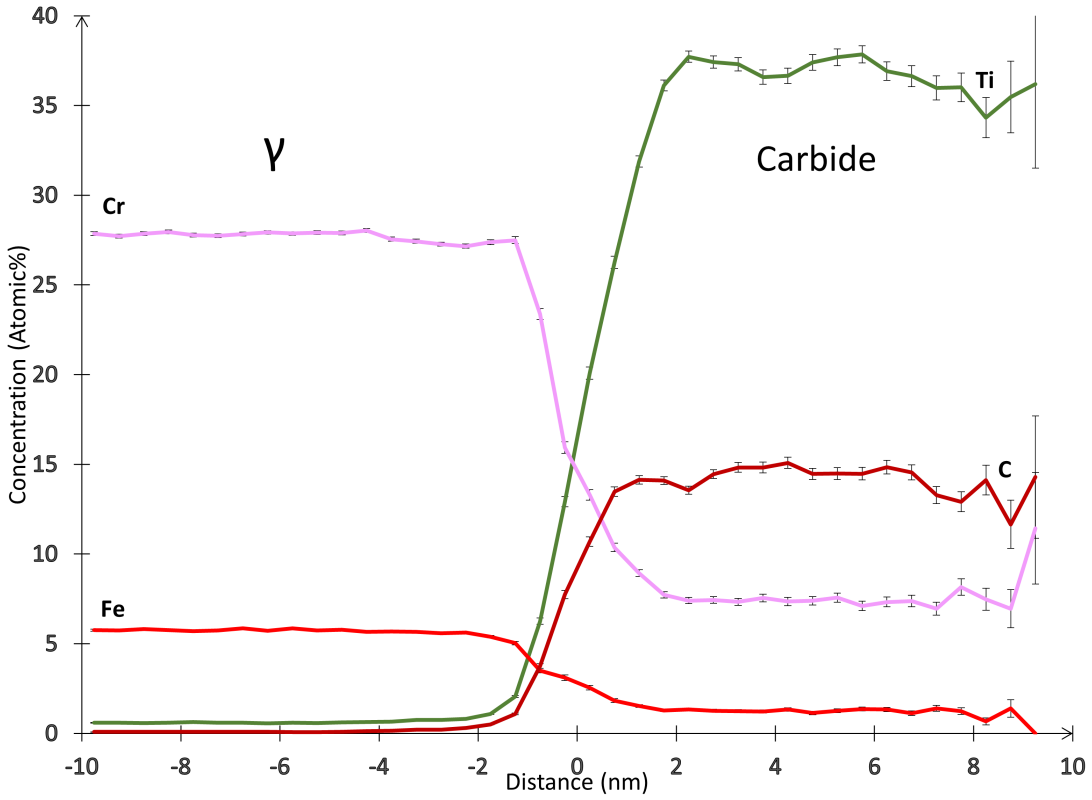

Figure 4.31: Proxigram with elements changing drastically in concentration when moving from outside to inside the carbide volume. Error bars correspond to the 2σ counting error.

The other proxigrams showcase the composition of the carbide surface as shown in Figure 4.32. The elements used in this proxigram are elements that seem to increase in value at the particle surface. Note that it also is a grain boundary present at the carbide surface. This proxigram has a maximum distance of 10 nm and a bin size of 0.5. Each element is named close to its respective curve.

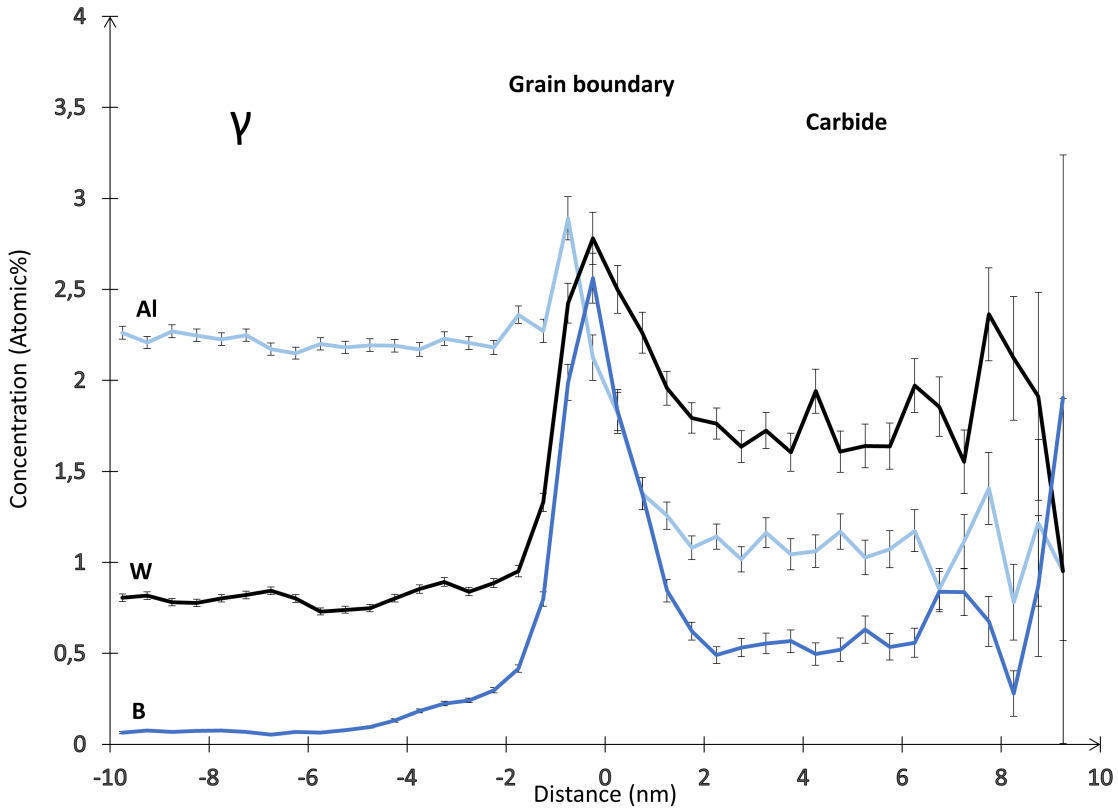

Figure 4.32: Proxigram with elements that show a higher concentration at the carbide surface. In this proxigram molybdenum is not included to better highlight the shape of the curves for the other elements. Error bars correspond to the 2σ counting error.

Figure 4.33 is the same proxigram as Figure 4.32 showcasing the Mo concentration of the carbide surface. The separate curve of Mo is to better highlight the shape of the curves for the other elements in Figure 4.32.

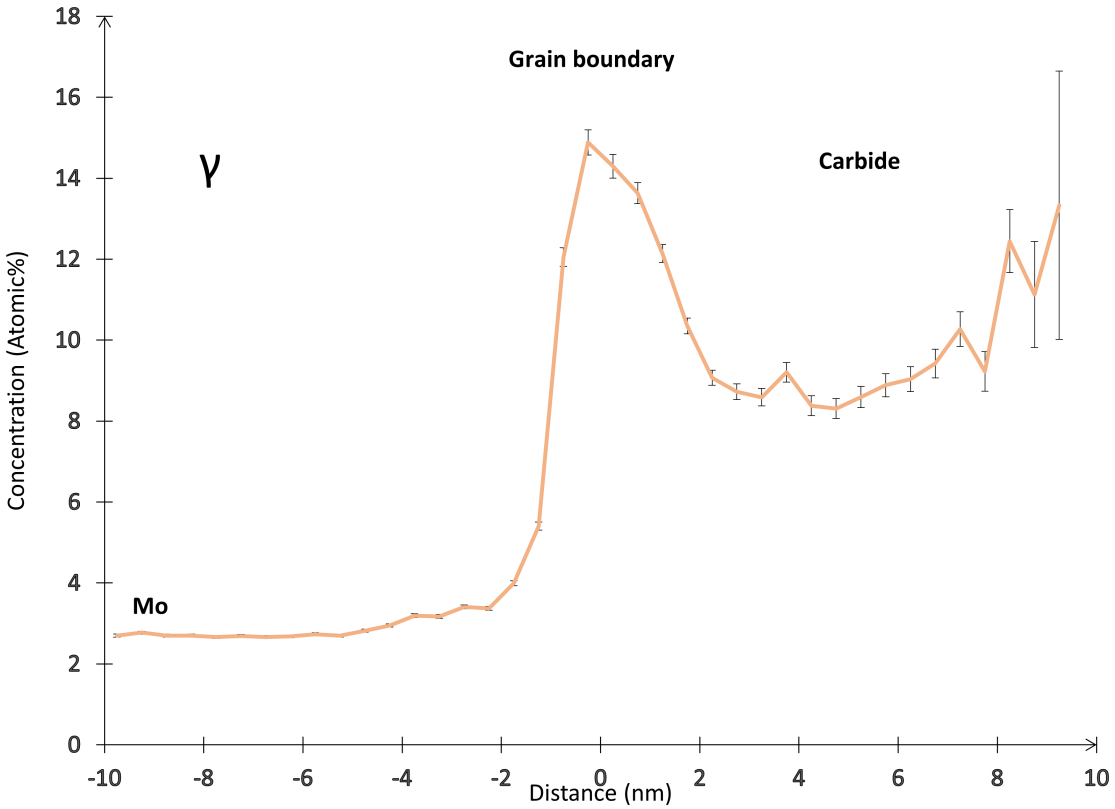

Figure 4.33: Proxigram from the carbide surface showcasing the change in composition of Mo. Error bars correspond to the 2σ counting error.

5. Discussion

Intergranular cracking and embrittlement of the C alloy

The C alloy showed significantly lower creep properties compared to the CB alloy according to Figure 3.1. It was found fewer cracks on the polished surface of the C alloy with the SEM compared to the CB alloy. The CB alloy had multiple cracks both close and some millimeters away from the fracture surface with varying sizes. All cracks found on the C alloy seem to have propagated to long cracks as both cracks in Figure 4.1 and 4.4 are longer than 30 μm. The absence of boron might have resulted in the lower creep properties of the sample as cracks easily propagated along grain boundaries, which might explain why all cracks were intergranular. Without the beneficial effects of boron the grain boundaries have shown little creep resistance with the lack of grain boundary strengthening. Other effects could also be related to grain boundary embrittlement. Figure 4.2 and 4.5 shows both cracks imaged with backscattered electrons. Oxides seem to be present in both cracks as these have a high contrast compared to the base material with BSE as seen in Figure 4.2 and 4.5. There are a lot more oxides present in the C alloy compared to the CB alloy indicating that the C alloy is more susceptible to grain boundary embrittlement. It is said that boron decreases diffusion along grain boundaries which might mean that boron decreases diffusion of oxygen along grain boundaries, which results in less grain boundary embrittlement. One of the reasons boron might increase creep properties could be that the boron decreases the grain boundary embrittlement in addition to the strengthening effects. The oxides present inside the cracks also hint to these cracks being a result of creep, as the cracks had access to oxygen which would be provided during fracture of the sample. These cracks do therefore not seem to be a result of the additive manufacturing process, as one would expect less oxides present inside these cracks. There were also not observed any cracks similar to what was named internal cracks in [105], which were small cracks consisting of cavities along grain boundaries. This could also indicate that this alloy suffered mainly from grain boundary embrittlement. The EBSD results show that both cracks have propagated intergranulary along high angle grain boundaries. The cracks seem to have propagated 45°with respect to the fracture surface. This was discussed in [105] to indicate that the cracks are related to creep deformation.

Comparison of composition for the CB and C alloy with APT

The atom probe reconstruction from CB given in Figure 4.7 shows a typical reconstruction of a nickel-based superalloy with γ' precipitates inside the γ matrix. This is also seen in Figure 4.11. The composition of both the CB alloy in Figure 4.8 and for the C alloy in Figure 4.12 and 4.13 seems to be quite similar with almost identical shape of the graphs. The atomic percent for the given alloying elements and nickel seems to be around the same range for both samples in both γ and γ'. It was not observed any carbon in the C alloy with APT. This might be a result of the carbon being mostly at the grain boundaries in the sample. When boron is not present the carbon is no longer in the losing battle of occupying sites around grain boundaries and might achieve a higher grain boundary segregation. In the literature as mentioned earlier segregation is observed of carbon around grain boundaries with APT, even in alloys with a low amount of carbon. Presence of carbon and boron was observed in the bulk of the CB alloy as shown in Figure 4.9. From this proxigram it seems as most of the boron reside on the γ/γ' interface in the bulk material or in γ when a grain boundary is not present. It seems as it is an overall higher amount of boron in γ compared to γ'. The reason carbon and boron are detected in CB might be because of the two elements competing, as the combination of these elements reduces the overall segregation. The grain boundaries might be already occupied with boron or carbon, resulting in a higher concentration of these elements in γ and γ'. The addition of carbon might reduce the grain boundary segregation of boron which results in a higher boron concentration in the bulk material.

The lever rule was used for both the CB and C alloys resulting in a similar volume fraction of γ' of 43-44%. γ' is what provides the strength and mechanical properties of this alloy, where one often wants to increase the volume fraction of γ' to increase the strength of the material. This means that the large deviation in creep resistance measured from these alloys does not originate from a difference in the volume fraction of γ'. The most likely explanation is therefore that boron is the reason for CB having a superior creep resistance compared to C as seen in Figure 3.1. This is further backed by the observation that the proxigrams from both samples seen in Figure 4.8 and 4.12 almost look identical with around the same concentration for each element. Both samples are very similar in composition, with boron being the main difference. This highlights the criticality of alloying with boron to increase the creep strength. The grain boundaries are still the weakest points of the alloys as both of them crack intergranulary, showing the importance of grain boundary strengthening.

Boron segregation at grain boundaries

The large boron enrichment that might possibly be a grain boundary is located along a large γ/γ' surface as seen in Figure 4.15 and 4.16. This is the part of the grain boundary above the carbide surface which is marked with (1. The boron iso-surfaces indicating the boron enrichments are inside both γ and γ' close to the interface. It was observed in Figure 4.9 that there was an increased concentration of boron on the γ/γ' interface. An interesting angle on this could be that the boron iso-surfaces in Figure 4.16 are very high boron enrichment on the interface. In other words, the boron has segregated at the interfaces and not a grain boundary. It is shown in Figure 4.17 that the boron concentration in the possible grain boundary is low. One might expect to find a higher concentration of boron at a grain boundary as for example the concentration in [12] was between 2-7% on a similar alloy. These grain boundaries did however not have any carbides present in the reconstruction.

In a previous study [106], it was found that borides formed progressively through building with additive manufacturing of the nickel-based superalloy. When the borides formed, solutes around the boride were depleted and consumed by the boride. This means that the presence of an intermetallic particle could decrease the overall concentration of boron at the grain boundaries as a result of boron diffusing to the particle present in the material. No borides or carbides were observed in this alloy with SEM, given the resolution of an SEM [105]. It was however found a carbide in the reconstruction in Figure 4.29 which is right underneath the possible grain boundary. This then seems to indicate that there are carbides present in the CB alloy. The results in Figure 4.31 shows that the carbon and titanium content increases drastically inside the particle volume, indicating that this might be a titanium carbide.

It is shown in Figure 4.32 that the boron concentration increases to around 2.5% at the surface of the carbide. Figure 4.19 show that the boron concentration is almost at 8% on the carbide surface. This amount of boron is what is expected at a grain boundary. The high boron concentration found in Figure 4.19 and Figure 4.32 therefore indicates that the grain boundary goes along the carbide surface, as there are only high amounts of boron at the surface and not inside the carbide volume. This is also clear in Figure 4.15 where the carbide surface is indicated with a boron iso-surface. The grain boundary might therefore go along the carbide surface and then follow the green line shown in Figure 4.16. The part of the grain boundary which is above the carbide might have a decreased concentration of boron since it is so close to the carbide which would consume a lot of boron. It was found in [106] that the portion of the grain boundary closest to an intermetallic particle had a lower concentration compared to a part further away. It might be that a part of the grain boundary further away from the carbide, which was not included in the reconstruction had a higher boron concentration.

The boron iso-surfaces in Figure 4.16 c) seem to consist of a grain boundary and boron enrichments. Some of these iso-surfaces look similar to the boron enrichments presented in other reconstructions which were discussed to perhaps be dislocations. It might be that some of these iso-surfaces are dislocations close to the grain boundary. For example from a dislocation pile-up where multiple dislocations would be present in the proximity of the grain boundary. The pile-up would be a result of the deformation that happened during the creep test of the sample, which could explain why the grain boundaries found in [12] look different from the grain boundary found here. In the article from Tytko [55] it was observed titanium carbides at the grain boundary in a polycrystalline superalloy. It was argued that these carbides also had negative effects as a result of the carbides being incoherent with the matrix which gave a high dislocation density. The dislocation density could then lead to increased creep rates in the material. It might be that that this high dislocation density is what is seen in Figure 4.16. It could also be that the grain boundary only goes along the carbide surface and that all the boron enrichments above the carbide surface are dislocations from the pile-up. This could for example explain the differences in boron concentration between the possible grain boundary part above the carbide and the grain boundary part along the carbide surface. To be certain when analyzing grain boundaries in the future, correlative TEM/APT (transmission electron microscope) should be used to make sure that a grain boundary is present in the sample before it is run in the APT. This would remove a lot of uncertainties and help to distinguish grain boundaries, dislocations and other phenomena. An example is presented in Figure 5.1 where one can observe the grain boundary in a) with TEM before the sample is run in the APT. The results are then shown in b) and c) where one is certain that there is a grain boundary present in the sample.

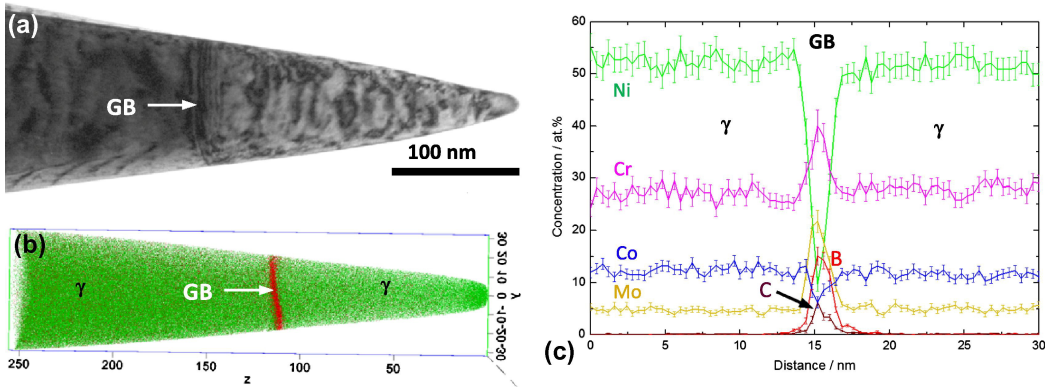

Figure 5.1: APT sample analyzed with TEM in a) and with the final reconstruction in b) where a grain boundary is analyzed [55].

It might be that the concentration profile in Figure 4.17 shows the boron concentration in a dislocation or an array of dislocations, and not a grain boundary above the carbide surface. If there are both dislocations and a grain boundary present above the carbide surface in this reconstruction, it might seem as both have around the same boron concentration. All attempts of measuring the concentration profile seemed to result in approximately the same values no matter the size and placement of the ROI. This value is lower than all composition profiles for the boron enrichments in Figure 4.22, 4.25 and 4.28. One reason for the low boron concentration on the grain boundary could be that there are a lot more points where boron could segregate as there is a grain boundary and multiple dislocations present. It could also be because of the carbide that is present, reducing the boron concentration in the area around itself. This further proves the value of correlative TEM/APT for dividing grain boundaries and dislocations.

Molybdenum segregates at both dislocations and grain boundaries as seen in the literature for other superalloys. The molybdenum peak in Figure 4.18 might indicate that the measured area is simply not just a boron enrichment on an interface, but a dislocation or grain boundary. Carbon showed little variation in concentration between the composition profiles for the boron enrichments, with no outstanding peak. The amount of carbon inside the enrichments seems to be generally low. This is visible in for example Figure 4.22 where carbon does not have any peak in concentration present. It was then assumed that carbon does not segregate to dislocations in this alloy, which could for example be a result of competing sites with boron and the slower diffusion of carbon. In Figure 4.17 it does however seem as carbon has a peak in concentration at the same location as boron which could indicate that this is a grain boundary. In this figure the carbon content is almost 0.1% lower at the highest concentration of boron while for the rest the carbon concentration is almost equal or even higher in some areas. This is a contrast to the composition profiles for the enrichments, where the carbon concentration was quite low compared to the boron.

Segregation of boron on dislocations

Some unexpected results from the CB alloy were the boron enrichments which were found in multiple reconstructions. The enrichment found in Figure 4.27 seems to extend over a larger area than the enrichments found in the other reconstructions. All boron enrichments seem to be located close to a γ/γ' surface and to have roughly the same boron concentrations as seen in Figure 4.22, 4.25 and 4.28, and vary between ca. 0.7 and 1.9 at.%. These enrichments might correspond to boron segregating at dislocations or at least parts of dislocations. The boron enrichments might be a result of Cottrell atmospheres that have formed around the dislocations giving the enrichments the linear shape. If boron segregates at dislocations inside this superalloy this might give a strengthening effect as the atmospheres slow down dislocation movement. This might also increase the creep strength of the alloy as moving dislocations during creep are slowed down by the formation of these atmospheres. An interesting angle could however be that these atmospheres indirectly weaken the grain boundaries of the superalloy by trapping the boron on the dislocations and thereby hindering the boron from segregating to the grain boundaries. In other words, this might result in an overall decreased amount of grain boundary segregation of boron. This could explain the lower boron concentration found on the possible grain boundary. If the grain boundary is surrounded by multiple dislocations from a pile-up this might mean that there are a lot of available sites for the boron to segregate at. If boron then segregates at the dislocations instead of the grain boundary, it might decrease the maximum possible grain boundary segregation. Most cracks found on the CB alloy were intergranular meaning the grain boundaries are the weakest link of the alloy. Weakening of the grain boundaries would therefore mean an overall weaker alloy. It was found in [105] that some intergranular cracks transitioned to transgranular cracks during propagation. This was discussed to be a result of boron segregating at the grain boundaries. Less boron segregated at the grain boundaries might therefore lower the chance for this transition during crack propagation. It is shown in Figure 3.1 that the CB alloy has similar creep strength to an alloy that is produced with traditional routes. If boron did not segregate at dislocations then perhaps this alloy produced with AM would be able to even transcend some mechanical properties of the alloys which were cast and wrought. This has been observed in other cases with other nickel-based superalloys. It is shown in Figure 4.22, 4.25 and 4.28 that the concentration of molybdenum increases in the areas of high boron concentrations. This seems to correlate well with other findings, where Mo have segregated at dislocations [92, 107]. This further backs the possibility of the boron enrichments being dislocations instead of random enrichments as Mo is known as a typical element

to segregate at dislocations.

Desegregation of grain boundaries

Multiple attempts to analyze a grain boundary with the APT were unsuccessful as it is challenging to prepare the samples to get a grain boundary inside the sample tip. Out of eight APT experiments it was only found a possible grain boundary in one of the samples. In previous studies, boron clearly decorates grain boundaries as observed by APT. It was expected to identify the grain boundary in a similar way here. However if this segregation is not present it would be difficult to observe the grain boundary. Desegregation of grain boundaries is a phenomenon where boron or other elements that have segregated at the boundaries diffuse away from the grain boundary. These solutes usually diffuse into grain boundary precipitates as carbides or borides and usually occur after heat treatment [53, 108, 109, 110]. Segregation of boron at grain boundaries usually occurs as nonequilibrium segregation. This type of segregation tends to happen during cooling from high temperatures. At high temperatures a high amount of vacancies are created inside the grains. During cooling the grains become supersaturated with vacancies causing the vacancies to diffuse towards the grain boundary. If these vacancies meet a boron atom on the way to the grain boundary it might drag the boron atom with it to the grain boundary. This then causes segregation of boron at the grain boundary. Desegregation of grain boundaries may only occur at grain boundaries enriched from nonequilibrium segregation. The degree of desegregation depends on the temperature and cooling rate as enough time is necessary to achieve desegregation [111].

In the atom probe experiments in [12] the CB alloy was analyzed after heat treatment where grain boundary segregation of boron was observed. However for the sample called C+B+Zr where zirconium also was added to the alloy, the Zr was no longer present at the grain boundary after heat treatment. It was instead found a high concentration of Zr inside the γ' phase. After heat treatment the CB alloy was creep tested at 650 °C for almost 2500 hours until the sample ruptured. An interesting possibility could be that desegregation of the sample occurred during creep testing. The sample was exposed to a high temperature for a significantly long amount of time. It might therefore be that the boron diffused into the grain interior during creep. The desegregation of boron from the grain boundaries may then have weakened the grain boundaries causing the sample to fracture intergranulary as described in [105]. This would then explain why almost all cracks in the CB alloy propagated intergranulary and why so few grain boundaries with boron segregation were observed during this thesis. The weakening of the grain boundaries would have a detrimental effect on the creep properties of the alloy as the lack of boron segregation would severely weaken the alloy. This is observed for the C alloy which showed significantly lower creep resistance compared to the CB alloy as seen in Figure 3.1. In this case the boron might have acted similar to what zirconium already has shown in a similar alloy. However if the CB alloy fractured as a result of boron desegregating one might expect to observe a larger amount of oxides present in the cracks as seen for the C alloy in Figure 4.2 and 4.5. Since no boron grain boundary segregation was found in most APT samples one would expect that most of the boron would have desegregated. This would also imply that grain boundary embrittlement could be possible as boron was discussed to be the reason for CB experiencing less embrittlement than the C alloy. This could therefore imply that boron should be present at the grain boundaries and that no grain boundaries were present in these samples. An idea could also be that desegregation happen gradually through the creep test. Then the intergranular crack propagation might have occurred when the grain boundaries had a low enough boron concentration from desegregation. It could however be that there was some boron still present

preventing grain boundary embrittlement, but not sufficient enough to prevent cracking. This would then lead to the cracks being a result of creep, while perhaps the cracks in the C alloy are more affected by grain boundary embrittlement. This would explain the difference in oxides in the cracks from each alloy.

While most observations of desegregation are of boron diffusing to grain boundary precipitates, the article from [111] defines desegregation as atoms diffusing away from the grain boundary and back to the grain interior. If boron has desegregated from the grain boundaries it should be present somewhere else in the microstructure. Four different scenarios will therefore be discussed. These scenarios are boron desegregating to:

- i) The grain bulk
- ii) Dislocations
- iii) The γ/γ' interfaces
- iv) Intergranular particles as borides and carbides

These scenarios will also be illustrated in simplified schematics for visualization purposes. Note that if desegregation occurs multiple events might occur and not necessarily only one of them. Figure 5.2 is a schematic of a grain boundary segregated with boron before desegregation occurs and therefore has a significant amount of boron segregation. This is also the case for the part of the grain boundary that goes along the carbide. A γ' precipitate is also present in this figure.

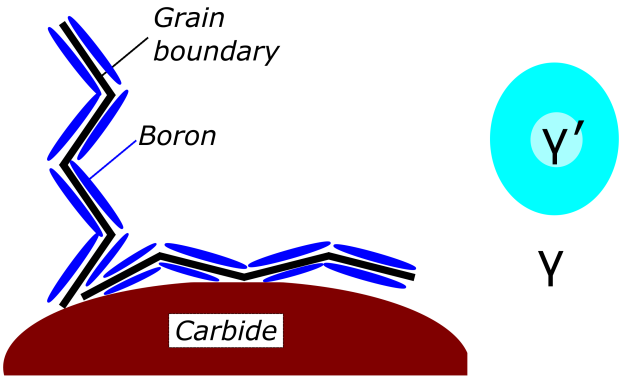

Figure 5.2: Schematic of a grain boundary, carbide and γ/γ' before desegregation. The grain boundary has a significant amount of boron segregation.

Segregation at dislocations

Boron enrichment was observed in multiple samples from the CB alloy. It is discussed that these enrichments might be dislocations where boron has segregated. These dislocations seem to be mostly present in the γ phase and close to the γ/γ' interface as seen in Figure 4.21, 4.24 and 4.27. One can observe in Figure 4.9 that these are the areas that generally have the highest concentration of boron present. A possibility might therefore be that boron desegregates from the grain boundaries and into the grain bulk as illustrated in Figure 5.3. Note that there is less boron on the part of the grain boundary above the carbide in the schematic after desegregation, compared to the part of the grain boundary that goes along the carbide surface. It might stay inside the bulk which explains the higher amount of boron in γ, or if a dislocation is present it could diffuse from the grain bulk to the dislocation as illustrated in Figure 5.4. This scenario would therefore mean that the segregation of boron on dislocations occurs during the creep test and is not present before this. This agrees with the presented theory which said that carbon and other elements could segregate to moving dislocations. One would expect this to be the case during creep while the material is deforming. If most of the boron in the sample was segregated at grain boundaries before the creep test and then desegregated from the grain boundaries, it would mean a significant boron concentration would be present in the bulk material. If the boron atoms then segregate at dislocations it could explain why the boron enrichments were found so frequently in the CB alloys. It would also explain the high amount of boron concentration found in each enrichment with peak values around 1-2 at.%.

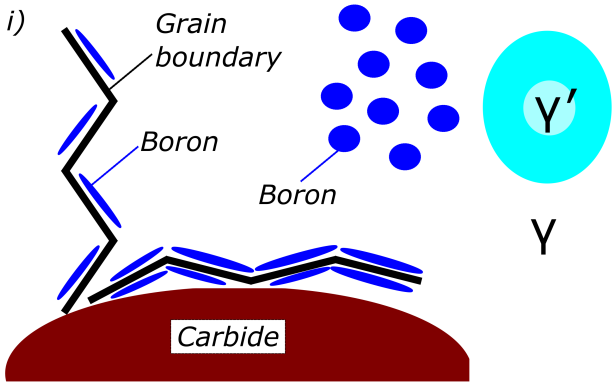

Figure 5.3: Schematic of desegregation of boron to the bulk material. The grain boundary has a reduced amount of boron segregation at the part above the carbide.

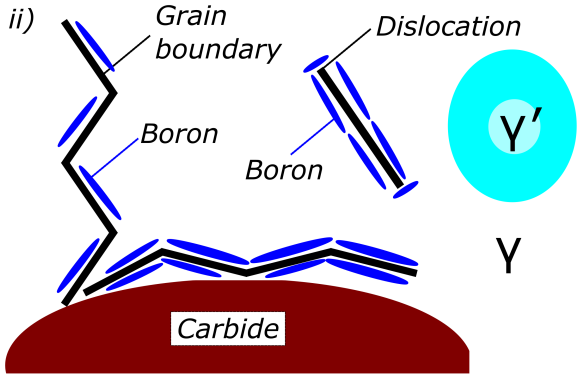

Figure 5.4: Schematic of boron segregated at a dislocation in the alloy after desegregation.

Segregation at γ/γ' interfaces

If no dislocations are present in the vicinity of the desegregated boron another possibility might be that the boron diffuses to the γ/γ' interfaces as shown in Figure 5.5. It is seen in Figure 4.9 that there is a high amount of boron on these interfaces. Note that all boron enrichments that were observed were in close proximity of γ/γ' interfaces. If these enrichments are not dislocations it might be the interfaces that are the reason for the boron enrichments. These interfaces might then have attracted the boron in the bulk material if these interfaces are more preferential for the boron compared to the bulk material.

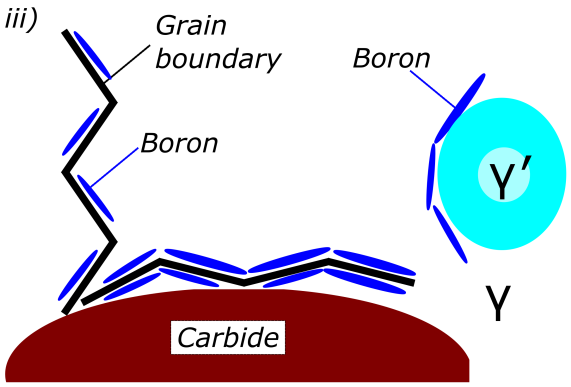

Figure 5.5: Schematic of boron segregated at a γ/γ' interface as a result of desegregation of a grain boundary.

Formation of intermetallic particles

The final event that might occur is that the boron has led to the formation of intermetallic particles or been consumed during coarsening of existing particles leading to grain boundary desegregation. A carbide that has consumed boron is illustrated in Figure 5.6. Most reviewed literature writing about boron desegregation observed boron partitioning to particles. In an article from Kurban [112] the segregation of boron was studied in an austenitic stainless steel. It was found that boron had a tendency to desegregate from grain boundaries during annealing at 800 °C with increasing annealing time. The boron then desegregated into carbides which precipitated at the grain boundaries. It was then discussed that boron has a higher affinity to carbides compared to grain boundaries. This could be connected with the earlier discussion of the grain boundary carbide consuming boron.

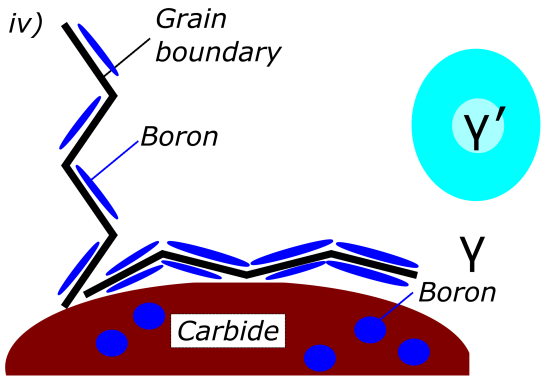

Figure 5.6: Schematic of a carbide having increased amounts of boron from formation, causing a reduced amount of boron segregation at the grain boundary.

If the boron enrichments above the carbide in Figure 4.15 and 4.16 is a grain boundary and there is desegregation of boron during creep the next question then might be how a grain boundary this close to a carbide still has segregation of boron? If there are grain boundaries present in the other reconstructions with boron fully desegregated then one would expect a grain boundary this close to a carbide to be fully desegregated too. This could therefore be an indication of desegregation not being the case in this alloy. Another reason might perhaps be that desegregation does not occur for all grain boundaries. This would mean that the grain boundary found here did not have any desegregation, while other reconstructions had fully desegregated grain boundaries. For example as a result of the carbide present in the same reconstruction as the grain boundary. If desegregation did occur during creep then perhaps boron desegregating from other grain boundaries collided with the grain boundary in Figure 4.30 on its way to the carbide and therefore segregated to this grain boundary instead. If desegregation occurred one would expect that all boron segregated at this grain boundary before creep would have been consumed by the carbide during desegregation. This would therefore mean that this grain boundary would be fully desegregated of boron before the diffusing boron from another grain boundary hit this boundary close to the carbide. This would again mean that there would be a lot of empty sites for boron to occupy at the grain boundary. Desegregation to particles is mainly observed after heat treatment in the literature, meaning higher temperatures and shorter time. More specifically during cooling where the temperature is decreasing and not constant as during this creep test. This could perhaps change up the desegregation behavior meaning for example desegregation to dislocations occur more frequently, or that desegregation to carbides occurs less as a result of the lower temperature. This discussion around desegregation shows why the use of correlative

TEM/APT could be important. This would give a definite answer to the question regarding if grain boundaries are present, regardless of boron being segregated at the grain boundaries or not.

It is also worth noting that all analyzed samples were attempts of studying grain boundaries, meaning all analyzed volumes at least are in the vicinity of a grain boundary. As all lift-outs were from grain boundaries as mentioned earlier. This means that for example all dislocations, bulk material and γ/γ' interfaces were close to the grain boundaries where desegregation might have occurred. This could for example mean that dislocations inside the grain bulk a long distance away from grain boundaries will not have any boron segregated. If the boron atoms actually are able to reach dislocations and other points of interest most likely depend on the diffusion process during creep. Boron diffuses fast [106], and with the creep test lasting over 2000 hours it might therefore be able to diffuse the necessary distance if the temperature is sufficient. Further research of multiple grain boundaries is required for this sample to determine the chemistry of the grain boundaries and to study if desegregation of boron does occur during creep. This would also highlight differences between different grain boundaries which would explain if desegregation and segregation of boron happens to only some or most of the grain boundaries in the sample. Analyzes of dislocations inside the grain bulk would help to determine if the boron enrichments are a result of desegregation from grain boundaries.

6. Conclusion

Two versions of the AD730 alloy named CB and C were studied to investigate grain boundary segregation and cracking after additive manufacturing and creep testing. The alloys were produced with laser powder bed fusion and were creep tested with the loading direction perpendicular to the building direction with a load of 690 MPa at 650 °C. Both alloys were investigated with atom probe tomography, as this characterization technique allows us to study boron segregation on crystal defects.

- All cracks found at the C alloy had propagated intergranulary. This indicates that the alloy fractured during creep as a result of lacking grain boundary strengthening. It was also observed significant amounts of oxides in the cracks which could mean the grain boundaries experienced embrittlement during creep. This was not observed for the CB alloy which could mean that boron segregating at the grain boundaries hinders embrittlement by for example hindering diffusion of oxygen along the boundaries.

- The calculated volume fraction of γ' was almost identical for both alloys. This indicates that the great deviation in creep strength is a result of the lack of boron in the C alloy. This is also backed by the fact that the composition of both alloys is almost identical.

- A grain boundary was found in a reconstruction from the CB alloy. This grain boundary had one part that seemed to go along a carbide surface and one part above the carbide. This grain boundary seemed to be surrounded by dislocations in a dislocation pile-up. The part along the carbide was assumed to be a grain boundary since it had a very high boron concentration.

- The boron concentration of the grain boundary part above the carbide was lower than expected. One reason for this could be that boron segregating at dislocations decreases the overall segregation at the grain boundaries. Which then indirectly weakens the grain boundary. Another possibility is that boron was consumed during formation or coarsening of the nearby carbide. It is also possible that the part above the carbide are dislocations from the pile-up and not part of the grain boundary.

- Multiple boron enrichments were found in the CB alloy which could correspond to boron segregation at dislocations. Increased amounts of of molybdenum was also found in the same regions. This segregation could strengthen the alloy by decreasing dislocation movement.

- Desegregation was also discussed as few grain boundaries were found in the reconstruction volumes. It is documented that desegregation of grain boundaries can happen for boron during heat treatment and it was also observed for zirconium in a similar alloy. Desegregation could be connected to the intergranular cracking as the grain boundary segregation would decrease during desegregation. The boron could then segregate at for example dislocations, γ/γ' interfaces or particles in the vicinity of the grain boundary. This would explain why the boron enrichments were found so frequently in the CB alloy. Desegregation might however not happen for all grain boundaries as it was found a grain boundary with boron segregation. It is also possible that desegregation did not occur at all.

7. Further studies

A lot is still unknown regarding the segregation behavior of boron after additive manufacturing and creep. More grain boundaries from the CB alloy should be analyzed to have more examples to compare with. This would make it easier to find the relationship between intermetallic particles, segregation, creep and manufacturing. This thesis relies on one reconstruction with multiple elements including dislocations, a grain boundary and a carbide which could have multiple interactions with each other. Having for example a grain boundary without any carbide present would help to divide effects from different sources when comparing with the results from this thesis. APT analyzes from the grain bulk would help to identify if segregation on dislocations occurs further away from grain boundaries and would also make it possible to compare the boron concentration in the grain bulk with what is found here. Correlative TEM and APT seems to be a powerful combination of characterization tools. This would be of great value to distinguish grain boundaries and dislocations and also to see if there are grain boundaries that are fully desegregated present. It could also be interesting to study grain boundaries in the C alloy to see how the composition of the grain boundaries changes when boron is absent. It could also be valuable to heat treat similar alloys at the same parameters as the creep test without applying stress. This would make it possible to identify what effect stress has on the segregations in the alloys. More studies on what effect creep and additive manufacturing has on grain boundary segregations could be interesting and valuable in future alloy design for high-temperature applications.

Bibliography

[1] ASTM, ISO, Astm52900-15 standard terminology for additive manufacturing—general principles—terminology, ASTM International, West Conshohocken, PA 3 (2015) 5.

[2] B. Graybill, M. Li, D. Malawey, C. Ma, J.-M. Alvarado-Orozco, E. Martinez-Franco, Additive Manufacturing of Nickel-Based Superalloys Volume 1: Additive Manufacturing; Bio and Sustainable Manufacturing (2018). V001T01A015.

[3] P. Nandwana, A. M. Elliott, D. Siddel, A. Merriman, W. H. Peter, S. S. Babu, Powder bed binder jet 3D printing of Inconel 718: Densification, microstructural evolution and challenges, Current Opinion in Solid State and Materials Science 21 (2017) 207–218.

[4] A. Yadollahi, N. Shamsaei, Additive manufacturing of fatigue resistant materials: Challenges and opportunities, International Journal of Fatigue 98 (2017) 14–31.

[5] A. Basak, S. Das, Effect of heat treatment on the microstructures of CMSX-4 processed through scanning laser epitaxy (SLE), in: 2017 International Solid Freeform Fabrication Symposium, University of Texas at Austin, 2017.

[6] Y. Lee, M. Nordin, S. S. Babu, D. F. Farson, Effect of fluid convection on dendrite arm spacing in laser deposition, Metallurgical and Materials Transactions B 45 (2014) 1520–1529.

[7] I. Lopez-Galilea, B. Ruttert, J. He, T. Hammerschmidt, R. Drautz, B. Gault, W. Theisen, Additive manufacturing of CMSX-4 Ni-base superalloy by selective laser melting: Influence of processing parameters and heat treatment, Additive Manufacturing 30 (2019) 100874.

[8] D. Raabe, M. Herbig, S. Sandlöbes, Y. Li, D. Tytko, M. Kuzmina, D. Ponge, P.-P. Choi, Grain boundary segregation engineering in metallic alloys: A pathway to the design of interfaces, Current Opinion in Solid State and Materials Science 18 (2014) 253–261. Slip Localization and Transfer in Deformation and Fatigue of Polycrystals.

[9] B. Gault, Atom Probe Microscopy, volume 160 of *Springer Series in Materials Science*, 1st ed. 2012. ed., Springer New York : Imprint: Springer, New York, NY, 2012.

[10] R. Reed, The Superalloys: Fundamentals and Applications, Cambridge University Press, 2008.

[11] D. K. Ganji, G. Rajyalakshmi, Influence of alloying compositions on the properties of nickel-based superalloys: a review, Recent Advances in Mechanical Engineering (2020) 537–555.

[12] A. Després, S. Antonov, C. Mayer, C. Tassin, M. Veron, J.-J. Blandin, P. Kontis, G. Martin, On the role of boron, carbon and zirconium on hot cracking and creep resistance of an additively manufactured polycrystalline superalloy, Materialia 19 (2021) 101193.

[13] Q. Chen, N. Jones, D. Knowles, The microstructures of base/modified RR2072 SX superalloys and their effects on creep properties at elevated temperatures, Acta Materialia 50 (2002) 1095–1112.

[14] M. Miller, Contributions of atom probe tomography to the understanding of nickel-based superalloys, Micron 32 (2001) 757–764.

[15] P. Kontis, A study on the effect of grain boundary elements on polycrystalline superalloys, Ph.D. thesis, University of Oxford, 2016.

[16] B. Fedelich, A. Epishin, T. Link, H. Klingelhöffer, G. Künecke, P. D. Portella, Rafting during high temperature deformation in a single crystal superalloy: experiments and modeling, Superalloys 6 (2012) 2012.

[17] A. Epishin, T. Link, M. Nazmy, M. Staubli, H. Klingelhoffer, G. Nolze, Microstructural degradation of CMSX-4: kinetics and effect on mechanical properties, Superalloys 2008 (2008) 725–731.

[18] M. Ott, H. Mughrabi, Dependence of the high-temperature low-cycle fatigue behaviour of the monocrystalline nickel-base superalloys CMSX-4 and CMSX-6 on the γ/γ'-morphology, Materials Science and Engineering: A 272 (1999) 24–30.

[19] Y.-t. Wu, C. Li, Y.-f. Li, J. Wu, X.-c. Xia, Y.-c. Liu, Effects of heat treatment on the microstructure and mechanical properties of Ni_3Al-based superalloys: A review, International Journal of Minerals, Metallurgy and Materials 28 (2021) 553–566.

[20] L. Lilensten, S. Antonov, B. Gault, S. Tin, P. Kontis, Enhanced creep performance in a polycrystalline superalloy driven by atomic-scale phase transformation along planar faults, Acta Materialia 202 (2021) 232–242.

[21] J. Jackson, M. Donachie, M. Gell, R. Henricks, The effect of volume percent of fine γ'on creep in Ds Mar-M200+ Hf, Metallurgical Transactions A 8 (1977) 1615–1620.

[22] M. Perrut, P. Caron, M. Thomas, A. Couret, High temperature materials for aerospace applications: Ni-based superalloys and -TiAl alloys, Comptes Rendus Physique 19 (2018) 657–671. New trends in metallic alloys / Alliages métalliques : nouvelles tendances.

[23] H. Qin, L. Lin, X.-b. Zhao, S.-f. Gao, J. Zhang, H.-z. Fu, Effect of carbon and boron additions on segregation behavior of directionally solidified nickel-base superalloys with rhenium, Transactions of Nonferrous Metals Society of China 23 (2013) 3257–3264.

[24] E. Chauvet, P. Kontis, E. A. Jägle, B. Gault, D. Raabe, C. Tassin, J.-J. Blandin, R. Dendievel, B. Vayre, S. Abed, G. Martin, Hot cracking mechanism affecting a non-weldable Ni-based superalloy produced by selective electron Beam Melting, Acta Materialia 142 (2018) 82–94.

[25] D. Bürger, A. Parsa, M. Ramsperger, C. Körner, G. Eggeler, Creep properties of single crystal Ni-base superalloys (SX): A comparison between conventionally cast and additive manufactured CMSX-4 materials, Materials Science and Engineering: A 762 (2019) 138098.

[26] L. Rickenbacher, T. Etter, S. Hövel, K. Wegener, High temperature material properties of IN738LC processed by selective laser melting (SLM) technology, Rapid Prototyping Journal (2013).

[27] R. Engeli, T. Etter, S. Hövel, K. Wegener, Processability of different IN738LC powder batches by selective laser melting, Journal of Materials Processing Technology 229 (2016) 484–491.

[28] L. N. Carter, C. Martin, P. J. Withers, M. M. Attallah, The influence of the laser scan strategy on grain structure and cracking behaviour in SLM powder-bed fabricated nickel superalloy, Journal of Alloys and Compounds 615 (2014) 338–347.

[29] M. M. Attallah, R. Jennings, X. Wang, L. N. Carter, Additive manufacturing of Ni-based superalloys: The outstanding issues, MRS Bulletin 41 (2016) 758–764.

[30] A. Hariharan, L. Lu, J. Risse, A. Kostka, B. Gault, E. A. Jägle, D. Raabe, Misorientation-dependent solute enrichment at interfaces and its contribution to defect formation mechanisms during laser additive manufacturing of superalloys, Physical Review Materials 3 (2019) 123602.

[31] A. Jiménez, P. Bidare, H. Hassanin, F. Tarlochan, S. Dimov, K. Essa, Powder-based laser hybrid additive manufacturing of metals: a review, The International Journal of Advanced Manufacturing Technology 114 (2021) 1–34.

[32] M. Cloots, K. Kunze, P. J. Uggowitzer, K. Wegener, Microstructural characteristics of the nickel-based alloy IN738LC and the cobalt-based alloy Mar-M509 produced by selective laser melting, Materials Science and Engineering: A 658 (2016) 68–76.

[33] Y. Chen, K. Zhang, J. Huang, S. R. E. Hosseini, Z. Li, Characterization of heat affected zone liquation cracking in laser additive manufacturing of Inconel 718, Materials Design 90 (2016) 586–594.

[34] M. Brennan, J. Keist, T. Palmer, Defects in metal additive manufacturing processes, Journal of Materials Engineering and Performance 30 (2021) 4808–4818.

[35] P. Ganesh, R. Kaul, C. Paul, P. Tiwari, S. Rai, R. Prasad, L. Kukreja, Fatigue and fracture toughness characteristics of laser rapid manufactured Inconel 625 structures, Materials Science and Engineering: A 527 (2010) 7490–7497.

[36] A. Theriault, L. Xue, J. Dryden, Fatigue behavior of laser consolidated IN-625 at room and elevated temperatures, Materials Science and Engineering: A 516 (2009) 217–225.

[37] L. Thivillon, P. Bertrand, B. Laget, I. Smurov, Potential of direct metal deposition technology for manufacturing thick functionally graded coatings and parts for reactors components, Journal of Nuclear Materials 385 (2009) 236–241. Nuclear Materials III.

[38] Y. Tian, N. Chekir, X. Wang, A. Nommeots-Nomm, R. Gauvin, M. Brochu, Microstructure characterization and grain morphology of alloy 625 with 0.4 wt% boron modification manufactured by laser wire deposition, Additive Manufacturing 24 (2018) 137–144.

[39] A. Ascari, A. Fortunato, A. H. Lutey, G. Guerrini, N. Pagano, Long pulse laser wire deposition of hard steels, Physics Procedia 83 (2016) 723–732. Laser Assisted Net Shape Engineering 9 International Conference on Photonic Technologies Proceedings of the LANE 2016 September 19-22, 2016 Fürth, Germany.

[40] C. Liu, C. White, Dynamic embrittlement of boron-doped Ni_3Al alloys at 600 °C, Acta Metallurgica 35 (1987) 643–649.

[41] J. C. Lippold, S. D. Kiser, J. N. DuPont, Welding metallurgy and weldability of nickel-base alloys, John Wiley & Sons, 2011.

[42] G. E. Dieter, Mechanical metallurgy, McGraw-Hill series in materials science and engineering, si metric ed. ed., McGraw-Hill, London, 1988.

[43] Y. Xu, Q. Jin, X. Xiao, X. Cao, G. Jia, Y. Zhu, H. Yin, Strengthening mechanisms of carbon in modified nickel-based superalloy Nimonic 80A, Materials Science and Engineering: A 528 (2011) 4600–4607.

[44] R. Fernandez, J. Lecomte, T. Kattamis, Effect of solidification parameters on the growth geometry of MC carbide in IN-100 dendritic monocrystals, Metallurgical transactions A 9 (1978) 1381–1386.

[45] A. Bhambri, T. Kattamis, J. Morral, Cast microstructure of Inconel 713C and its dependence on solidification variables, Metallurgical Transactions B 6 (1975) 523–537.

[46] J. Bae, J. Lee, S. Kim, C. Jo, Formation of MC-γ/γ' eutectic fibers and their effect on stress rupture behavior in D/S Mar-M247LC superalloy, Scripta Materialia 45 (2001) 503–508.

[47] T. Alam, P. J. Felfer, M. Chaturvedi, L. T. Stephenson, M. R. Kilburn, J. M. Cairney, Segregation of B, P, and C in the Ni-based superalloy, Inconel 718, Metallurgical and Materials Transactions A 43 (2012) 2183–2191.

[48] D. Shah, D. Duhl, Effect of minor elements on the deformation behavior of nickel-base superalloys, Superalloys 1988 (1988) 693–702.

[49] S. Tin, T. Pollock, W. King, Carbon additions and grain defect formation in high refractory nickel-base single crystal superalloys, Superalloys 2000 (2000) 201–210.

[50] K. Al-Jarba, G. Fuchs, Carbon-containing single-crystal nickel-based superalloys: Segregation behavior and carbide formation, JOM 56 (2004) 50–55.

[51] J. Stinville, K. Gallup, T. Pollock, Transverse creep of nickel-base superalloy bicrystals, Metallurgical and Materials Transactions A 46 (2015) 2516–2529.

[52] L. Xiao, D. Chen, M. Chaturvedi, Effect of boron on fatigue crack growth behavior in superalloy IN 718 at RT and 650°C, Materials Science and Engineering: A 428 (2006) 1–11.

[53] W. Chen, M. Chaturvedi, N. Richards, G. McMahon, Grain boundary segregation of boron in INCONEL 718, Metallurgical and Materials Transactions A 29 (1998) 1947–1954.

[54] S. Sanyal, U. V. Waghmare, T. Hanlon, E. L. Hall, P. Subramanian, M. Gigliotti, Interfaces in Ni-based superalloys and implications for mechanical behavior and environmental embrittlement: a first-principles study, Superalloys (2012) 531e536.

[55] D. Tytko, P.-P. Choi, J. Klöwer, A. Kostka, G. Inden, D. Raabe, Microstructural evolution of a Ni-based superalloy (617B) at 700°C studied by electron microscopy and atom probe tomography, Acta Materialia 60 (2012) 1731–1740.

[56] D. Blavette, P. Duval, L. Letellier, M. Guttmann, Atomic-scale APFIM and TEM investigation of grain boundary microchemistry in Astroloy nickel base superalloys, Acta Materialia 44 (1996) 4995–5005.

[57] S. Sijbrandij, M. Miller, J. Horton, W. Cao, Atom probe analysis of nickel-based superalloy IN-718 with boron and phosphorus additions, Materials Science and Engineering: A 250 (1998) 115–119.

[58] R. T. Holt, W. Wallace, Impurities and trace elements in nickel-base superalloys, International Metals Reviews 21 (1976) 1–24.

[59] S. Sanyal, U. V. Waghmare, P. Subramanian, M. F. Gigliotti, Effect of dopants on grain boundary decohesion of Ni: A first-principles study, Applied Physics Letters 93 (2008) 223113.

[60] T. Garosshen, T. Tillman, G. McCarthy, Effects of B, C, and Zr on the structure and properties of a P/M nickel base superalloy, Metallurgical Transactions A 18 (1987) 69–77.

[61] L. Xiao, M. C. Chaturvedi, D. Chen, Effect of boron and carbon on the fracture toughness of IN 718 superalloy at room temperature and 650°C, Journal of materials engineering and performance 14 (2005) 528–538.

[62] P. Zhou, J. Yu, X. Sun, H. Guan, Z. Hu, The role of boron on a conventional nickel-based superalloy, Materials Science and Engineering: A 491 (2008) 159–163.

[63] R. Messmer, C. Briant, The role of chemical bonding in grain boundary embrittlement, Acta Metallurgica 30 (1982) 457–467.

[64] C. Briant, R. Messmer, An electronic model for the effect of alloying elements on the phosphorus induced grain boundary embrittlement of steel, Acta Metallurgica 30 (1982) 1811–1818.

[65] Y. Liu, K. Chen, G. Lu, J. Zhang, Z. Hu, Impurity effects on the Ni/Ni_3Al interface cohesion, Acta Materialia 45 (1997) 1837–1849.

[66] J. Yang, Q. Zheng, X. Sun, H. Guan, Z. Hu, Relative stability of carbides and their effects on the properties of K465 superalloy, Materials Science and Engineering: A 429 (2006) 341–347.

[67] X. Li, M. Ou, M. Wang, L. Zhang, Y. Ma, K. Liu, Effect of boron addition on the microstructure and mechanical properties of K4750 nickel-based superalloy, Journal of Materials Science & Technology 60 (2021) 177–185.

[68] K. Laha, J. Kyono, T. Sasaki, S. Kishimoto, N. Shinya, Improved creep strength and creep ductility of type 347 austenitic stainless steel through the self-healing effect of boron for creep cavitation, Metallurgical and Materials Transactions A 36 (2005) 399–409.

[69] I. Baker, B. Huang, E. Schulson, The effect of boron on the lattice properties of Ni_3Al, Acta Metallurgica 36 (1988) 493–499.

[70] C. Lee, G. Han, R. Smallman, D. Feng, J. Lai, The influence of boron-doping on the effectiveness of grain boundary hardening in Ni_3Al, Acta Materialia 47 (1999) 1823–1830.

[71] S. Huang, A. Taub, K. Chang, Boron extended solubility and strengthening potency in rapidly solidified Ni_3Al, Acta Metallurgica 32 (1984) 1703–1707.

[72] B. Ladna, H. Birnbaum, Surface and grain boundary segregation of sulfur and boron in nickel, Acta Metallurgica 36 (1988) 745–755.

[73] X. Cheng, X. Wan, J. Guo, C. Liu, Effect of Zr and B on Environmental Embrittlement in Ni_3Al Alloys, Scripta Materialia 38 (1998) 959–964.

[74] P. Kontis, H. M. Yusof, S. Pedrazzini, M. Danaie, K. Moore, P. Bagot, M. Moody, C. Grovenor, R. Reed, On the effect of boron on grain boundary character in a new polycrystalline superalloy, Acta Materialia 103 (2016) 688–699.

[75] P. Bagot, O. Silk, J. Douglas, S. Pedrazzini, D. Crudden, T. Martin, M. Hardy, M. Moody, R. Reed, An atom probe tomography study of site preference and partitioning in a nickel-based superalloy, Acta Materialia 125 (2017) 156–165.

[76] E. A. Jägle, Z. Sheng, L. Wu, L. Lu, J. Risse, A. Weisheit, D. Raabe, Precipitation reactions in age-hardenable alloys during laser additive manufacturing, JOM 68 (2016) 943–949.

[77] F. I. Versnyder, M. Shank, The development of columnar grain and single crystal high temperature materials through directional solidification, Materials Science and Engineering 6 (1970) 213–247.

[78] J. Cao, J. Zhang, R. Chen, Y. Ye, Y. Hua, High temperature oxidation behavior of Ni-based superalloy GH202, Materials Characterization 118 (2016) 122–128.

[79] A. Németh, D. Crudden, D. Armstrong, D. Collins, K. Li, A. Wilkinson, C. Grovenor, R. Reed, Environmentally-assisted grain boundary attack as a mechanism of embrittlement in a nickel-based superalloy, Acta Materialia 126 (2017) 361–371.

[80] International Conference on Corrosion of Nickel-Base Alloys, Corrosion of nickel-base alloys : conference proceedings of the International Conference on Corrosion of Nickel-Base Alloys, 23-25 October 1984, Cincinnati, Ohio, American Society for Metals, Metals Park, Ohio, 1985.

[81] H. Kitaguchi, H. Li, H. Evans, R. Ding, I. Jones, G. Baxter, P. Bowen, Oxidation ahead of a crack tip in an advanced Ni-based superalloy, Acta Materialia 61 (2013) 1968–1981.

[82] U. Krupp, W. Kane, C. Laird, C. McMahon, Brittle intergranular fracture of a Ni-base superalloy at high temperatures by dynamic embrittlement, Materials Science and Engineering: A 387 (2004) 409–413.

[83] W. M. Kane, C. McMahon Jr, Part ii. effects of grain-boundary structure on the path of cracking in polycrystals, Materials Science and Engineering: A 507 (2009) 61–65.

[84] J. Pfaendtner, C. McMahon Jr, Oxygen-induced intergranular cracking of a Ni-base alloy at elevated temperatures—an example of dynamic embrittlement, Acta Materialia 49 (2001) 3369–3377.

[85] L. Viskari, M. Hörnqvist, K. Moore, Y. Cao, K. Stiller, Intergranular crack tip oxidation in a Ni-base superalloy, Acta Materialia 61 (2013) 3630–3639.

[86] H. Evans, H. Li, P. Bowen, A mechanism for stress-aided grain boundary oxidation ahead of cracks, Scripta Materialia 69 (2013) 179–182.

[87] H.-J. Christ, K. Wackermann, U. Krupp, Effect of dynamic embrittlement on high temperature fatigue crack propagation in IN718–experimental characterisation and mechanism-based modelling, Materials at High Temperatures 33 (2016) 528–535.

[88] R. Darolia, Development of strong, oxidation and corrosion resistant nickel-based superalloys: critical review of challenges, progress and prospects, International materials reviews 64 (2019) 355–380.

[89] P. Kontis, Interactions of solutes with crystal defects: A new dynamic design parameter for advanced alloys, Scripta Materialia 194 (2021) 113626.

[90] G. Viswanathan, R. Shi, A. Genc, V. Vorontsov, L. Kovarik, C. Rae, M. Mills, Segregation at stacking faults within the γ phase of two Ni-base superalloys following intermediate temperature creep, Scripta Materialia 94 (2015) 5–8.

[91] T. Smith, B. Esser, N. Antolin, G. Viswanathan, T. Hanlon, A. Wessman, D. Mourer, W. Windl, D. McComb, M. Mills, Segregation and η phase formation along stacking faults during creep at intermediate temperatures in a Ni-based superalloy, Acta Materialia 100 (2015) 19–31.

[92] X. Wu, S. K. Makineni, P. Kontis, G. Dehm, D. Raabe, B. Gault, G. Eggeler, On the segregation of Re at dislocations in the γ'phase of Ni-based single crystal superalloys, Materialia 4 (2018) 109–114.

[93] O. Waseda, R. G. Veiga, J. Morthomas, P. Chantrenne, C. S. Becquart, F. Ribeiro, A. Jelea, H. Goldenstein, M. Perez, Formation of carbon cottrell atmospheres and their effect on the stress field around an edge dislocation, Scripta Materialia 129 (2017) 16–19.

[94] D. Blavette, E. Cadel, A. Fraczkiewicz, A. Menand, Three-dimensional atomic-scale imaging of impurity segregation to line defects, Science 286 (1999) 2317–2319.

[95] R. Mulford, U. Kocks, New observations on the mechanisms of dynamic strain aging and of jerky flow, Acta Metallurgica 27 (1979) 1125–1134.

[96] J. Liu, C. Ye, Y. Dong, Recent development of thermally assisted surface hardening techniques: A review, Advances in Industrial and Manufacturing Engineering 2 (2021) 100006.

[97] R. Hayes, W. Hayes, On the mechanism of delayed discontinuous plastic flow in an age-hardened nickel alloy, Acta Metallurgica 30 (1982) 1295–1301.

[98] C. Scheu, E. Stergar, M. Schober, L. Cha, H. Clemens, A. Bartels, F.-P. Schimansky, A. Cerezo, High carbon solubility in a γ-TiAl-based Ti–45Al–5Nb–0.5 C alloy and its effect on hardening, Acta Materialia 57 (2009) 1504–1511.

[99] H. Suzuki, et al., Chemical interaction of solute atoms with dislocations, Sci. Rep. Res. Inst. Tohoku Univ. A 4 (1952) 455–463.

[100] G. Han, I. Jones, R. Smallman, Direct evidence for Suzuki segregation and Cottrell pinning in MP159 superalloy obtained by FEG(S)TEM/EDX, Acta Materialia 51 (2003) 2731–2742.

[101] L. Feng, Y. Rao, M. Ghazisaeidi, M. J. Mills, Y. Wang, Quantitative prediction of Suzuki segregation at stacking faults of the γ' phase in Ni-base superalloys, Acta Materialia 200 (2020) 223–235.

[102] B. Gault, M. P. Moody, J. M. Cairney, S. P. Ringer, Atom probe crystallography, Materials Today 15 (2012) 378–386.

[103] M. Miller, R. Forbes, Atom probe tomography, Materials Characterization 60 (2009) 461–469.

[104] A. Vella, J. Houard, Atom Probe Tomography, Chapter Eight - Laser-Assisted Field Evaporation, Academic Press, 2016.

[105] O. Vad, Creep deformation of an additively manufactured nickel-based superalloy, 2021.

[106] P. Kontis, E. Chauvet, Z. Peng, J. He, A. K. da Silva, D. Raabe, C. Tassin, J.-J. Blandin, S. Abed, R. Dendievel, B. Gault, G. Martin, Atomic-scale grain boundary engineering to overcome hot-cracking in additively-manufactured superalloys, Acta Materialia 177 (2019) 209–221.

[107] Q. Ding, S. Li, L.-Q. Chen, X. Han, Z. Zhang, Q. Yu, J. Li, Re segregation at interfacial dislocation network in a nickel-based superalloy, Acta Materialia 154 (2018) 137–146.

[108] A. Egbewande, H. Zhang, R. Sidhu, O. Ojo, Improvement in laser weldability of INCONEL 738 superalloy through microstructural modification, Metallurgical and Materials Transactions A 40 (2009) 2694–2704.

[109] X. Huang, M. Chaturvedi, N. Richards, J. Jackman, The effect of grain boundary segregation of boron in cast alloy 718 on HAZ microfissuring—A SIMS analysis, Acta Materialia 45 (1997) 3095–3107.

[110] R. Sidhu, O. Ojo, M. Chaturvedi, Microstructural response of directionally solidified René 80 superalloy to gas-tungsten arc welding, Metallurgical and Materials Transactions A 40 (2009) 150–162.

[111] O. Idowu, O. Ojo, M. Chaturvedi, Crack-free electron beam welding of Allvac 718Plus® superalloy, Welding journal 88 (2009) 179–187.

[112] M. Kurban, U. Erb, K. Aust, A grain boundary characterization study of boron segregation and carbide precipitation in alloy 304 austenitic stainless steel, Scripta Materialia 54 (2006) 1053–1058. Viewpoint set no. 40: Grain boundary engineering.

A. Results from project thesis

Some results from the project thesis [105] are attached to help the reader. These results are already examined and should not be evaluated for this thesis. These results are from the alloy named CB, including images taken with SE, BSE and EBSD. Figure 7.1 shows an intergranular crack close to the fracture surface of the CB alloy.

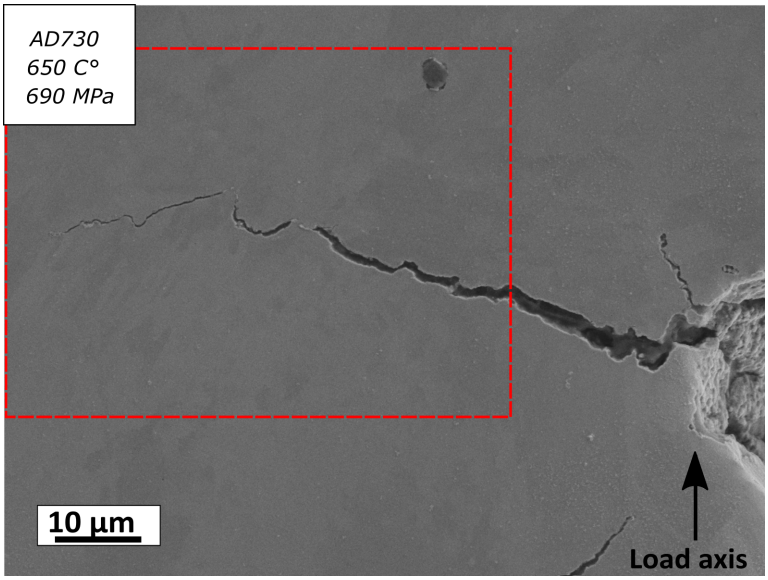

Figure 7.1: Example of a crack found close to the fracture surface of the sample. This image is taken with secondary electrons. The red dashed box marks where the EBSD analysis was applied in Figure 7.2.

Figure 7.2 shows the crack in Figure 7.1 from the area in the red dashed box with EBSD.

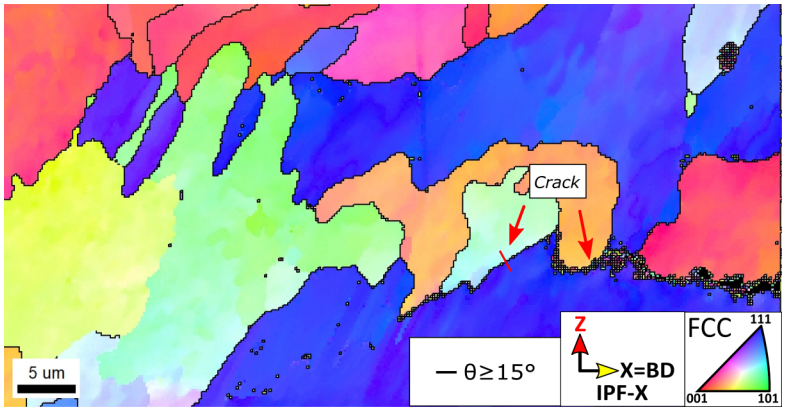

Figure 7.2: IPF-X map corresponding to the area denoted by the red dashed box in Figure 7.1. The crack is marked with red arrows.

A transition from intergranular to transgranular propagation is shown in Figure 7.3 with secondary electrons.

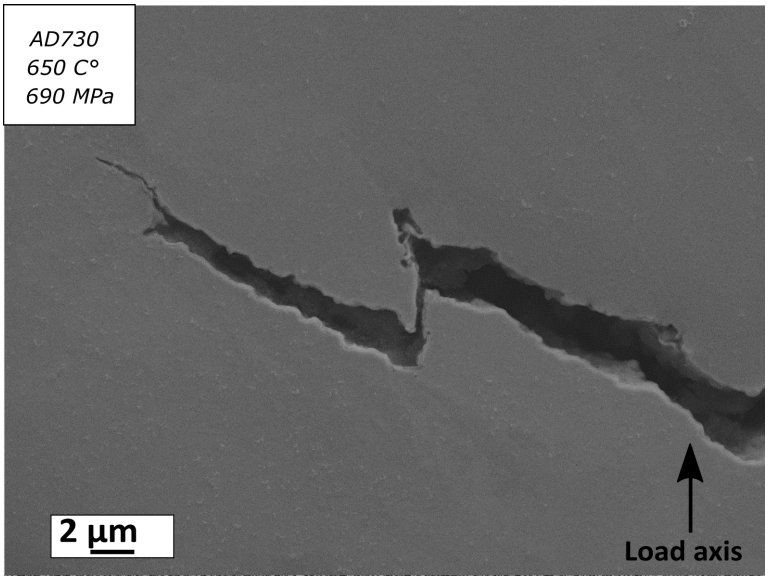

Figure 7.3: Image of a crack close to the fracture surface taken with secondary electrons. This is the same crack as in Figure 7.4.

Figure 7.4 shows an IPF-X map of the propagation transition in the crack from Figure 7.3.

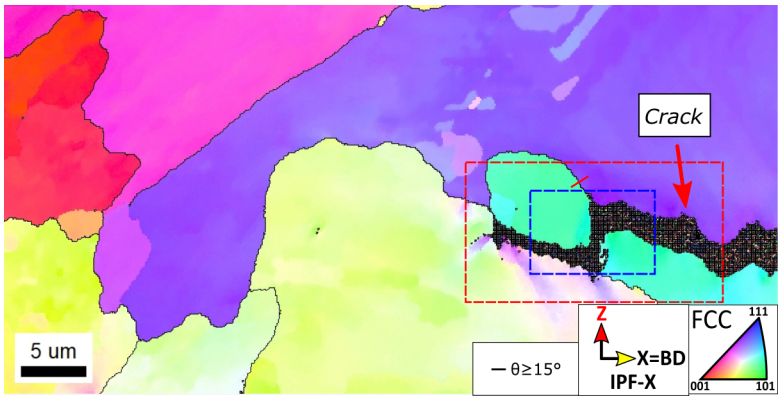

Figure 7.4: IPF-X map of the crack in Figure 7.3. This crack is marked with a red arrow. The red dashed box marks the area for Figure 7.3. The blue dashed box marks the area of Figure 7.5.

Figure 7.5 shows oxides present in the crack from Figure 7.3 with backscattered electrons.

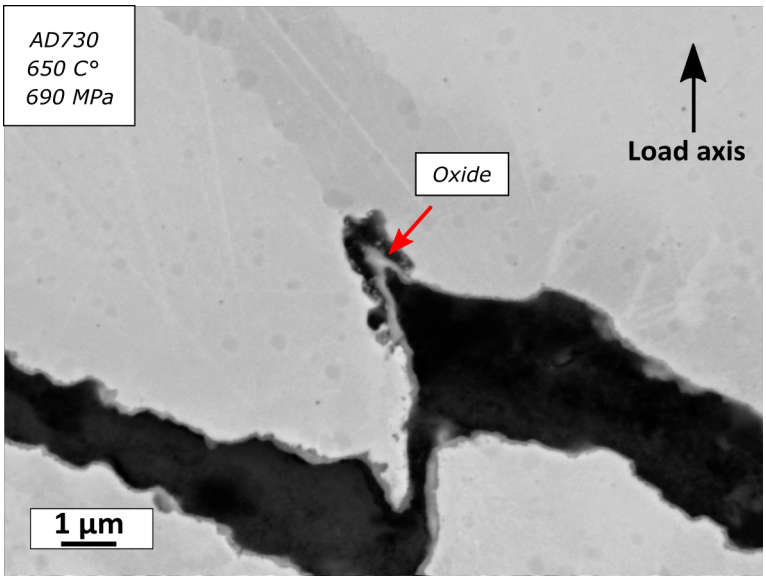

Figure 7.5: Image of a crack close to the fracture surface taken with backscattered electrons. This is the same crack as in Figure 7.4.

Multiple cracks are presented with secondary electrons in Figure 7.6.

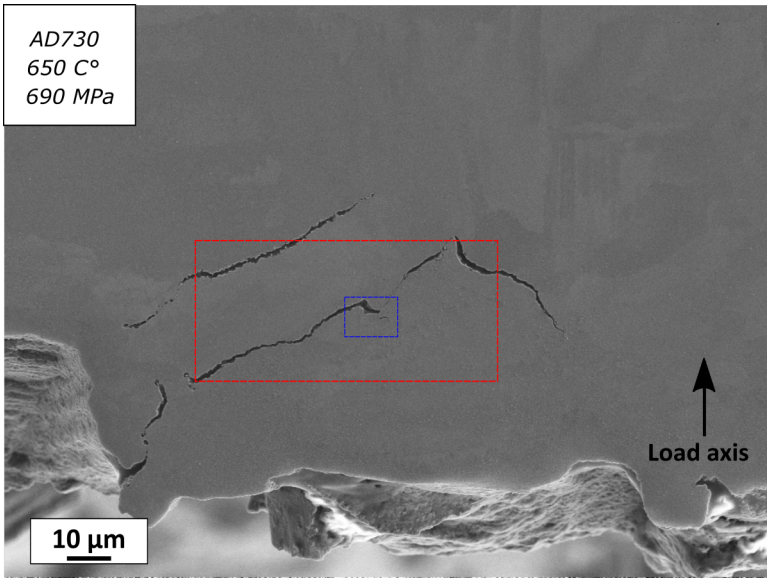

Figure 7.6: Image of cracks close to the fracture surface taken with secondary electrons. The red dashed box marks where the EBSD analysis in Figure 7.7 was performed. The blue dashed box indicates the area in Figure 7.8.

Figure 7.7 is an IPF-X map of the cracks given in Figure 7.6.

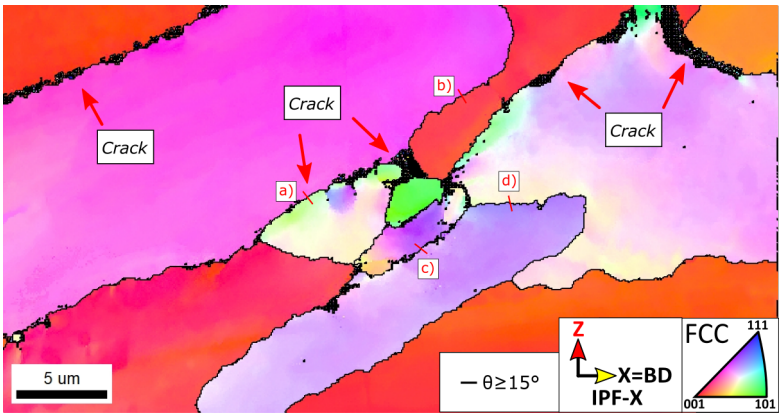

Figure 7.7: IPF-X map of cracks found close to the fracture surface given in Figure 7.6. Some of the cracks are indicated with red arrows. The points a)-d) are areas where misorientation was measured.

Figure 7.8 is an image taken with backscattered electrons of the cracks in Figure 7.6.

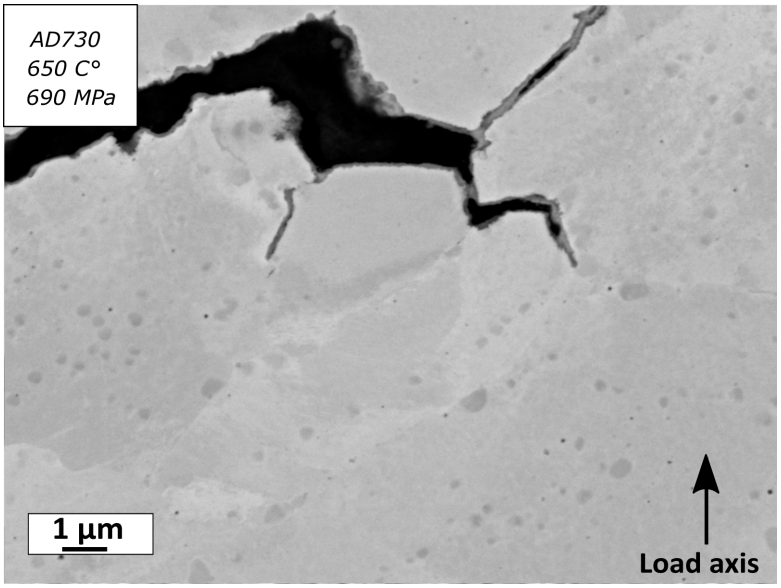

Figure 7.8: Image of cracks close to the fracture surface taken with backscattered electrons in the area marked with a blue dashed box in Figure 7.6.

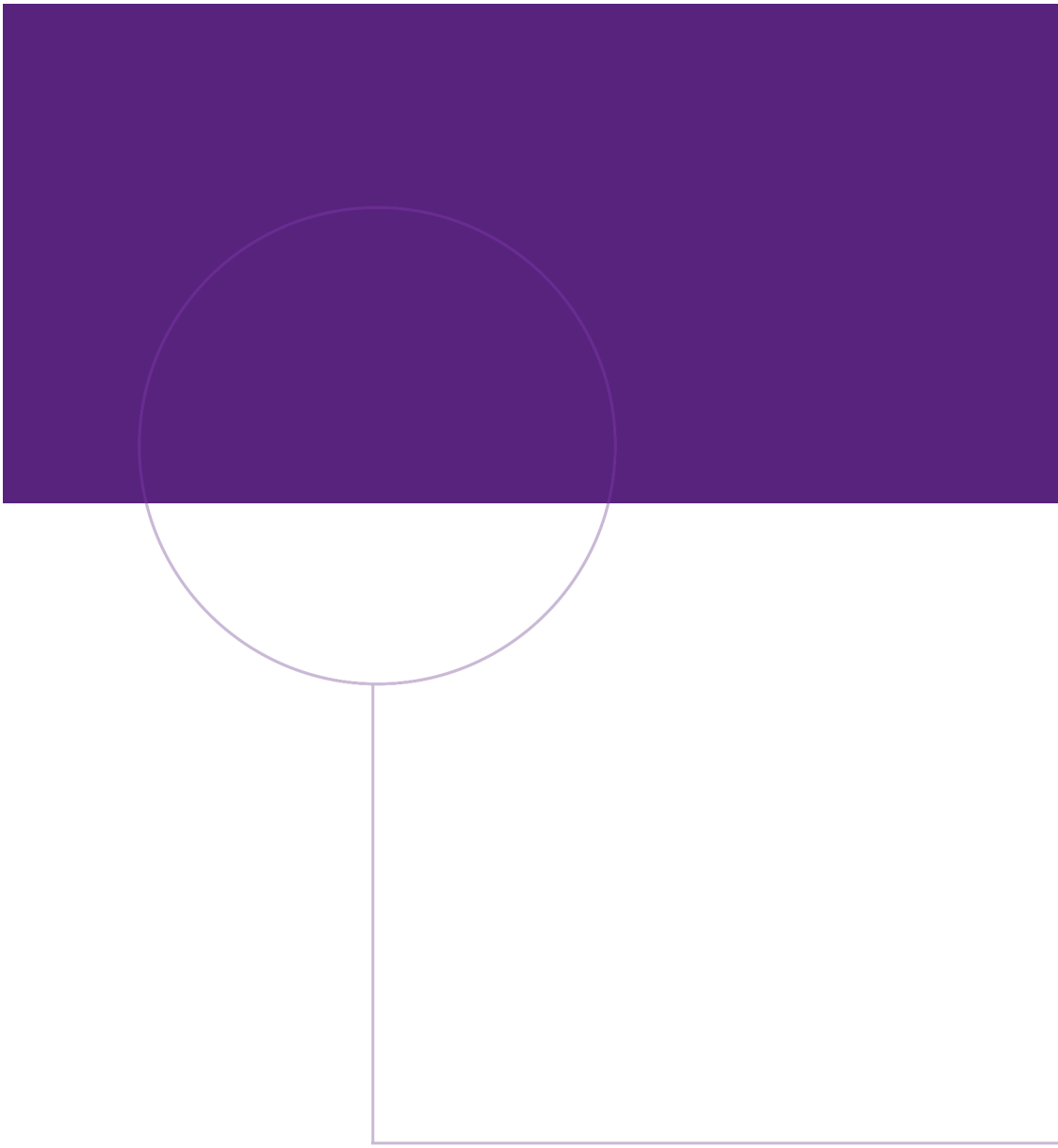

NTNU

Norwegian University of
Science and Technology